Hybridization of Andreev bound states in closely spaced Josephson junctions

Vincent Benzoni

PSL
UNIVERSITÉ PARIS

THÈSE DE DOCTORAT
DE L'UNIVERSITÉ PSL

Préparée au Collège de France

Hybridization of Andreev bound states in closely spaced Josephson junctions

Hybridation d'états liés d'Andreev dans des jonctions Josephson contiguës

Soutenue par
Vincent BENZONI
Le 4 Mars 2021

Ecole doctorale n° 564
École doctorale Physique en Île-de-France

Spécialité
Physique

Composition du jury :

Marcelo, GOFFMAN Chargé de recherche, CEA-Saclay	*Président*
François, LEFLOCH Chargé de recherche, CEA-Grenoble	*Rapporteur*
Régis, MÉLIN Directeur de recherche, Institut Néel	*Rapporteur*
Julia, MEYER Professeur, Université Grenoble Alpes	*Examinateur*
Çağlar, GIRIT Chargé de recherche, Collège de France	*Directeur de thèse*

COLLÈGE DE FRANCE
1530

"À vaincre sans péril, on triomphe sans gloire !"
Pierrre Corneille

"Be water, my friend!"
Bruce Lee

This thesis discusses the hybridization of Andreev bound states in a system of two closely spaced Josephson junctions, an "Andreev molecule". Devices incorporating Andreev molecules are predicted to have an energy spectrum with avoided crossings and a non-conventional current-phase relation.

The first part is a theoretical analysis of Andreev Molecule. Two microscopic mechanisms at the origin of the hybridization of Andreev bound states are explained. Furthermore, electrical characteristics of a molecule in multiple circuit configurations are calculated using different theoretical frameworks.

In the second part measurements of a circuit made up of two Josephson junctions in close proximity to each other are presented. Although possible signs of hybridization are detected, due to the presence of noise and insufficiently small junction separation, the results are inconclusive.

In the third part technical details of device fabrication and the measurement setup, including a millikelvin DC cryogenic amplifier, are described.

Cette thèse traite de l'hybridation des états liés d'Andreev dans un système formé de deux jonctions Josephson contiguës, une "molécule d'Andreev". Il est prédit que les dispositifs incorporant des molécules d'Andreev ont un spectre d'énergie avec des anti-croisements et une relation courant-phase non conventionnelle.

La première partie est une analyse théorique de la molécule d'Andreev. Les deux mécanismes microscopiques à l'origine de l'hybridation des états liés d'Andreev y sont décrits. De plus, les caractéristiques électriques d'une molécule dans des configurations de circuits multiples y sont calculées à l'aide de différents cadres théoriques.

Dans la deuxième partie sont présentées des mesures d'un circuit constitué de deux jonctions Josephson très proches l'une de l'autre. Bien que des signes possibles d'hybridation soient détectés, en raison de la présence de bruit et d'une séparation des jonctions trop faible, les résultats ne sont pas concluants.

Dans la troisième partie sont décrits les détails techniques de la fabrication de l'appareil et du dispositif de mesure, y compris l'utilisation à des millikelvins d'un amplificateur DC cryogénique.

Vincent BENZONI Hybridization of Andreev Bound States in closely spaced Josephson Junctions 2021

Hybridization of Andreev Bound States in closely spaced Josephson Junctions

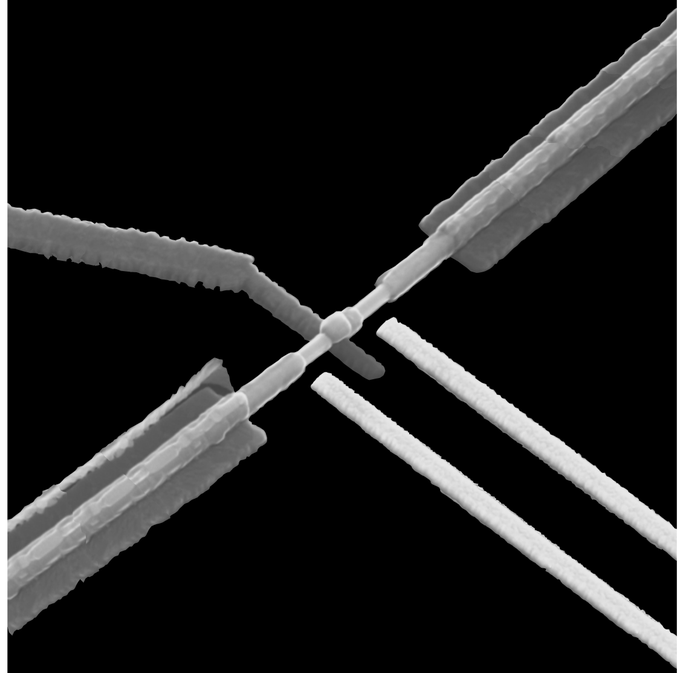

Vincent BENZONI
Φ_0 Lab
Collège de France, Paris

"Que la force me soit donnée de supporter ce qui ne peut être changé et le courage de changer ce qui peut l'être mais aussi la sagesse de distinguer l'un de l'autre."
Marc Aurèle

"If you're going through hell, keep going."
Winston Churchill

Remerciements

"En recevant la distinction que le jury a bien voulu m'accorder, ma gratitude est d'autant plus profonde que je mesurais à quel point cette récompense dépasse mes mérites personnels" Camus. Très vite en commençant mon travail d'expérimentateur, je me suis retrouvé à me sentir comme un artisan au sens noble du terme. C'est-à-dire comme un homme qui se met au service de sa passion en améliorant sa technique inlassablement pour participer à une œuvre qui le dépasse. Ce travail long, parfois difficile, le plus souvent acharné n'a été possible que grâce à la présence de ceux dont j'aime à croire qu'ils sont mes compagnons : ces hommes et ces femmes riches de leurs seuls doutes, animés par la même passion pour la belle physique. Si j'essaie de rendre modestement hommage à cette dernière dans les chapitres suivants, c'est à ces rêveurs rigoureux que je souhaite dédier ces quelques lignes.

Cette aventure n'a pu commencer que grâce à la folie de Caglar de bien vouloir accepter d'être mon directeur de thèse. Depuis notre première rencontre pour un stage de master et encore aujourd'hui, tu as toujours été très inspirant pour moi. Ta rigueur scientifique, ta curiosité, ton dévouement à la physique ont toujours été pour moi une source d'inspiration. Je ne te serai jamais suffisamment reconnaissant pour tout ce que tu m'as permis d'apprendre et de découvrir. Je me souhaite un jour d'avoir ta sagesse, celle de l'artisan fidèle à son art, malgré les tumultes que celui-ci lui impose.

Jean-Loup, à l'instar de Caglar, tu m'as accompagné tout au long de mon parcours de jeune chercheur. Tu es un grand physicien au grand cœur, je te remercie d'avoir été toujours disponible pour m'écouter, me conseiller et me soutenir dans les moments les plus indispensables. Je te remercie également de m'avoir écouté quand je te bassinais avec tous mes projets de geekerie. Tes connaissances pointues sur des sujets précis et hétéroclites me manqueront.

JD, j'ai eu la chance de travailler avec toi au début de ma thèse. Tu as une place toute particulière dans toute cette aventure, car tu as grandement contribué à ce travail, qui n'aurait jamais pu voir le jour sous cette forme aussi aboutie sans toi. Je te remercie d'avoir passé de nombreuses heures à m'expliquer les rudiments de la physique des états d'Andreev et d'avoir toujours eu la volonté de se comprendre entre nous, mais aussi avec nos confrères. Ton amour pour la physique rayonnait à chacune de nos discussions et peu importe ton interlocuteur du plus farouche ou plus conquis, tu as toujours su exposer nos travaux avec une grande force de persuasion.

Fabien, tu as été compagnon du devoir que je souhaiterais à tout le monde de rencontrer. Tu as, en plus d'être un physicien aux mille facettes, un don pour mettre du baume au cœur et du cœur à l'ouvrage. Entre tes techniques de Sioux de fabrication, tes playlists, tes accents, ton écoute et ton humour, tu as été d'un grand support pour moi. Je te remercie d'avoir croisé mon chemin et d'avoir pris le temps de partager avec moi ton amour de la physique, du café, des bonnes affaires sur aliexpress et de la vie.

Joël, tu as été le premier thésard du groupe quand celui-ci était encore très jeune. Tu as été le premier cordé et tu m'as facilité le passage en ouvrant la voie avec ton calme et la force

tranquille qui te caractérisent. Je te remercie d'avoir eu la patience de me transmettre ce savoir gris du labo dont tu fus le premier producteur et gardien.

Léo, en tant que troisième thésard de Phi0, tu es mon successeur. Ce statut particulier à mes yeux fait que nous avons partagé beaucoup de choses pendant ces années. La pluralité des sujets que tu maîtrises et ta curiosité m'ont toujours impressionné, le tout couplé à ta constante bonne humeur. Je suis très heureux de t'avoir rencontré, impatient de découvrir tes qualités de myciculteur, mais surtout de te voir devenir docteur !

Ramiro, j'ai eu la chance d'écrire ma thèse à côté de toi dans notre bureau partagé. Je ne sais pas si la chance était partagée, mais ta sérénité, ta douceur et nos conversations tous les deux, quand j'avais besoin de respirer, ont été essentielles pour moi. Tu as une discipline, une éthique et une sagesse dans le travail qui te permettent d'aller là où tu le souhaites et de le partager avec les autres. Je te remercie pour tout cela.

Arthur, tu es arrivé vers la fin de ma thèse et même si nous n'avons pas passé beaucoup de temps ensemble, cela a rapidement été plaisir de travailler avec toi. La démonstration de ta volonté, ta force de travail pour mener à bien ton projet de recherche, passer le concours du CNRS et le réussir m'ont motivé pour finir d'écrire ma thèse. Je te remercie également pour cette chorégraphie avec l'enceinte Bluetooth le soir après ma soutenance, cela reste un des moments mémorables de cette journée.

Phi0 aura été l'un des plus beaux souvenirs de ma thèse. Je garde évidement de beaux souvenirs de science de cette aventure de mes premiers refroidissements de lignes supraconductrices en plomb, jusqu'aux mesures du dernier échantillon. Je garde aussi en mémoire des moments d'amitié. Il est commun d'entendre que ce qui compte n'est pas la destination, mais le voyage et bien pour ma thèse les membres de Phi0 auront été le paysage.

Je désire aussi particulièrement remercier le groupe Quantronique, le SPEC dans sa globalité et spécialement Marcelo. J'ai grâce à vous pu continuer ma thèse en me donnant la possibilité de fabriquer mes jonctions Josephson sur des nanofils d'InAs-Al.

Marcelo, j'ai eu la chance que tu puisses croire dans mon projet de double jonction. Étant le physicien généreux que tu es, tu m'as pris sous ton aile comme un étudiant pour me montrer tout le processus de fabrication que tu avais développé jusque-là et qui a été la base de mon travail. Je te suis très reconnaissant de m'avoir toujours soutenu aussi bien par tes conseils, ta bonne humeur, et tes fredonnements.

Je souhaite également remercier Pief et Sébastien pour leur disponibilité et leur patience infinie quand je venais les embêter pour des problèmes dans la salle blanche. Vous étiez toujours prêt à m'aider malgré mes demandes peu orthodoxes et ma capacité à rendre certaines machines hors service.

J'ai envie également remercier M. Goffman, M. Lefloch, M. Mélin et Mme Meyer d'avoir eu la gratitude de constituer mon jury.

Je souhaiterais remercier tous mes collègues du Collège de France, je pense notamment à Carmen, aux trois Françoise, à Pascal, à Nicolas et bien d'autres d'avoir apporté un support aussi bien technique qu'administratif sans faille, tout au long de ma thèse. Vous êtes les faiseurs de l'ombre sans qui rien de tout cela ne serait possible.

J'aimerais finir par remercier mes proches, mes parents qui ont su cultiver ma curiosité qui m'a permis d'en arriver là et qui m'ont soutenu tout long de l'écriture de cette thèse chacun dans leur style ; mes amis, qui ont tous survécu à des conversations bien trop longues où j'expliquais

ce que je faisais au labo, et qui sont restés mes amis même après cela.

J'aimerais finir en remerciant le plus tendrement possible ma nouvelle famille, Cécile (et ptitpti), qui ont été en première ligne dans les bons comme dans les mauvais moments et me donnent la chance d'être heureux de vivre et de me dépasser.

Contents

Résumé en français

Lorsque deux systèmes physiques sont juxtaposés, il n'est pas rare d'observer l'émergence de nouveaux phénomènes. Par exemple, la formation d'une molécule de dihydrogène est issue du rapprochement de deux atomes d'hydrogène en-dessous du rayon de Bohr. Cette proximité modifie les orbitales de chacun des atomes, leur spectre en énergie ainsi que leur propriété chimique. De même, dans un circuit électrique où la séparation entre des composants est inférieure à la longueur d'onde électromagnétique traversant ce dernier, les effets des interférences modifient sa réponse. Pour les composants électroniques, ces interactions peuvent devenir encore plus riches en ajoutant les ingrédients de la physique quantique. Les composants peuvent alors aussi être définis avec une longueur de cohérence électronique qui révèle une nouvelle dimension pour les interactions.

L'un des composants électroniques quantiques les plus représentatifs est la jonction Josephson. Les effets Josephson ont été théorisés en 1962 par Brian Josephson [1] puis observés dans la première jonction Josephson par Anderson et Rowell [2] en 1963. Une jonction Josephson est un composant constitué de deux îlots supraconducteurs séparés par un lien faible. Ce lien faible, au centre de la jonction, transporte un supercourant sans être un supraconducteur. Cet effet surprenant est rendu possible par l'existence des Etats Liés d'Andreev (Andreev Bound States ou ABS). Ces états microscopiques de quasi-particules liées, situés au niveau du lien faible, représentent des chemins fermés pour le transfert des paires de Cooper d'un côté à l'autre de la jonction sans dissipation. La dispersion énergétique des ABS dépend de la nature de la diffusion dans le lien faible ainsi que de la différence de phase à travers celui-ci. Les propriétés assez généralistes d'une jonction Josephson composée de deux supraconducteurs et d'un lien faible permettent l'existence d'un bestiaire très fournie. Il est possible de fabriquer des jonctions avec des liens faibles à base de métaux normaux, de semi-conducteur, de nanofil, de nanotube, de graphène, de vide, de contact atomique, etc. Ainsi, grâce à une conception flexible et au développement de techniques de fabrication sophistiquées, les jonctions Josephson sont devenues le couteau-suisse des circuits quantiques.

Lorsqu'elles sont isolées, les jonctions obéissent aux relations de Josephson. Leurs propriétés sont bien comprises et exploitées dans divers domaines tels que la magnétométrie [3] et la métrologie [4]. De plus, en raison de leur cohérence quantique et de leur potentiel d'intégration dans des circuits à grande échelle, les jonctions Josephson servent de base pour certaines architectures de qubits pour l'information et le calcul quantique [5, 6, 7, 8, 9, 10, 11, 12, 13].

En rapprochant deux jonctions Josephson l'une de l'autre, elles se couplent elles et ne sont plus isolées. Cette promiscuité permet alors de faire émerger de nouveaux phénomènes physiques. Dans des circuits avec des fréquences de fonctionnement et des vitesses de propagation typiques, les jonctions peuvent interagir via le champ électromagnétique sur des distances allant du micromètre au centimètre. Cette interaction est bien comprise et très utilisée dans plusieurs applicationsé[14]. Cependant, elle n'est pas intrinsèque dans la mesure où elle dépend entièrement de l'environnement électromagnétique qui couple les jonctions entre elles. En outre,

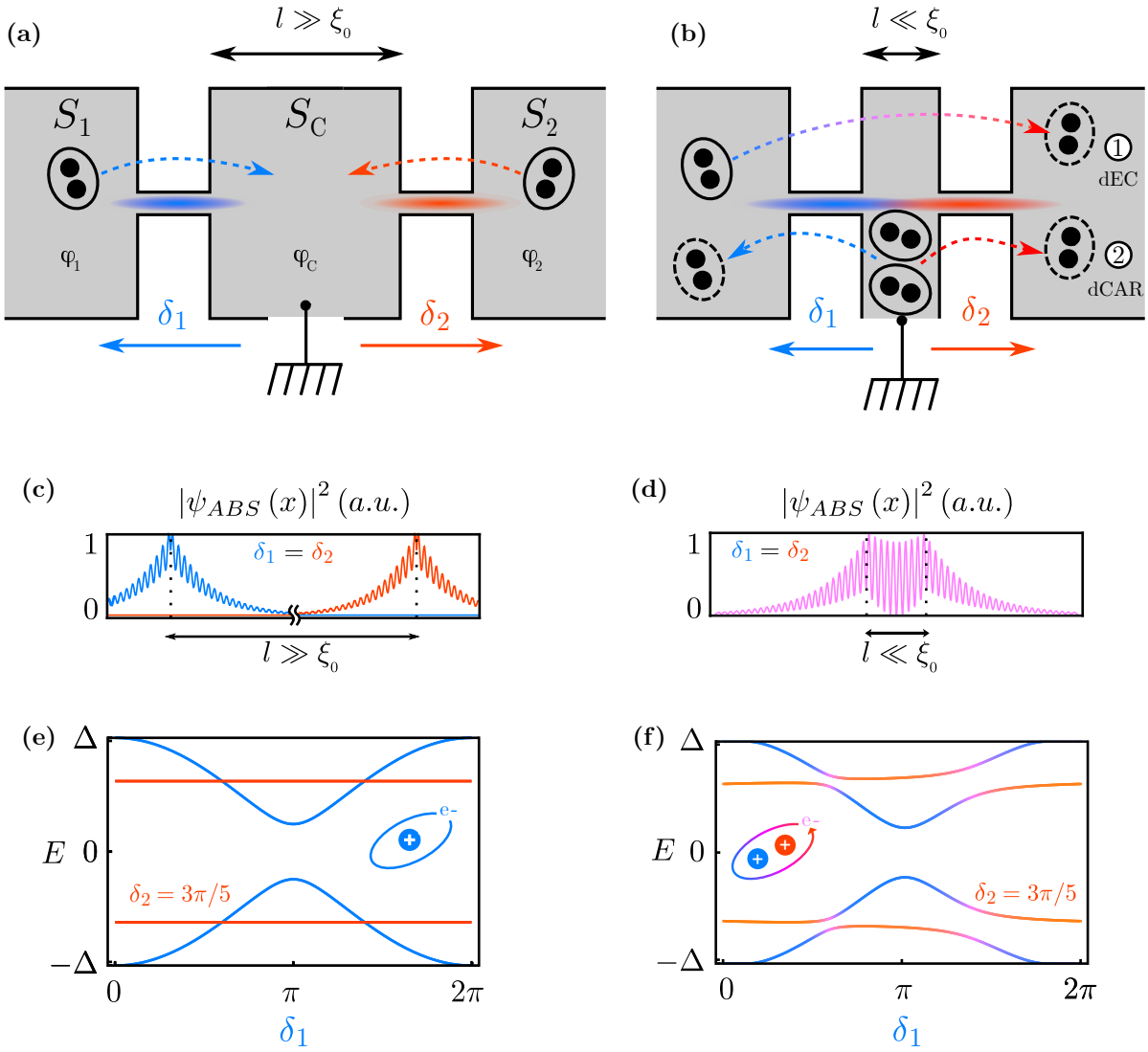

Figure 1: Hybridation de jonctions Josephson contigües. (a) Schéma de deux jonctions Josephson séparées par une distance de $l \gg \xi_0$. (b) Schéma d'une molécule d'Andreev, au sein de laquelle les états liés d'Andreev séparés par une distance $l \ll \xi_0$ s'hybridisent. Deux mécanismes non-locaux additionnels peuvent transporter les pairs de Cooper : le double co-tunneling élastique (dEC) et la double réflexion croisée d'Andreev (dCAR). (c)-(d) Fonctions d'onde des ABS. Lorsque la distance de séparation est grande ($l \gg \xi_0$), les fonctions d'onde ont un recouvrement négligeable. Pour des petites distances de séparation ($l \ll \xi_0$), les fonctions d'onde se recouvrent et s'hybridisent. (e)-(f) Spectre en énergie des ABS en fonction de δ_1 avec $\delta_2 = 3\pi/5$. Contrairement au cas des jonctions séparées, la molécule d'Andreev fait apparaître des croisements évités qui indiquent le mélange des états des deux jonctions.

les jonctions s'influencent également sur une distance de l'ordre du micron par la diffusion de quasi-particules. Cependant, cet effet n'est important qu'à proximité de T_c, la température de transition supraconductrice, ou pour des tensions de polarisation importantes [15]. Ce processus d'interaction modifie la valeur de l'énergie du gap supraconducteur ainsi que le courant critique.

A mesure que la distance entre les jonctions devient comparable à ξ_0 (la longueur de cohérence de l'état supraconducteur), des nouveaux processus apparaissent. Ces derniers trouvent leur origine dans le chevauchement des fonctions d'onde définissant l'ABS de chaque jonction. L'ABS est un système à deux niveaux, analogue à un atome artificiel. Ainsi, à l'image de la formation d'une molécule, le rapprochement de deux jonctions Josephson contrôlables indépendamment (c.-à-d. ABS) forme une molécule d'Andreev. Ce système intrigant a déjà été étudié dans des travaux précédents dans des régimes particuliers. Près de T_c, des travaux, utilisant les équations de Ginzburg-Landau, ont permit de calculer les effets résultant de cette interaction [15, 16]. Plus récemment, des théoriciens ont étudié ce problème à une température aléatoire en utilisant les fonctions de Green. Ces travaux ont permis de calculer des supercourants non-locaux hors équilibre et de démontrer l'existence d'un déphasage de π dans la relation courant-phase [17, 18, 19, 20, 21, 22]. Pour finir, un verrouillage de phase remarquable, similaire aux pas de Shapiro, a été prédit puis mesuré expérimentalement dans des bi-jonctions supraconductrices polarisées avec des tensions commensurables [23, 24]

Cette thèse a pour but de poursuivre ces travaux intéressants et d'explorer la molécule d'Andreev sur un plan à la fois théorique et expérimental.

La partie théorique présente une description microscopique du mécanisme responsable de l'hybridation des jonctions et comprend une étude de la fragilité de l'hybridation dans des systèmes comportant de nombreux canaux et un degré de désordre. La description de la construction théorique d'une molécule d'Andreev est exposée en partant d'une seule jonction Josephson (Fig. 1(e) et (b)).

Une fois construite, l'étape suivante est la description de la molécule d'Andreev la plus simple possible à une dimension et un canal à l'aide des équations de Bogoliubov-de Gennes. Par la suite, il est présenté l'analyse d'un système plus compliqué mais plus proche d'une réalisation expérimentale. Cette étude utilise le formalisme de Landauer-Büttiker pour décrire une molécule d'Andreev unidimensionnelle avec plusieurs canaux de conduction. Pour finir, le modèle d'une molécule d'Andreev à deux dimensions est développé à l'aide d'une méthode de liaisons fortes. Cette dernière approche permet l'ajout du désordre dans le modèle et d'en observer les effets. La fonction d'onde (Fig. 1(c) et (d)), le spectre d'énergie (Fig. 1(e) et (f)) et la relation courant-phase calculée à partir de ce modèle donnent les signatures attendues d'une molécule d'Andreev lors de mesures DC. De plus, la dépendance explicite des dimensions physiques dans ces relations facilite la conception et la fabrication d'une molécule d'Andreev.

La partie expérimentale décrit la fabrication d'un dispositif composé de deux jonctions Josephson juxtaposées, à partir de nanofils hybrides semiconducteur-supraconducteur épitaxiés en InAs-Al [25]. Cette plateforme technologique a été choisie pour ses caractéristiques satisfaisant les contraintes identifiées dans la partie théorique (Fig. 2(a)). Les mesures DC de ce dispositif sont présentées dans la Fig. 2(b). De ces mesures, il ressort que la distance de séparation entre les jonctions n'est pas assez petite pour observer un effet clair et renforce le caractère crucial de cette dimension. Ces premiers résultats encourageants ont permis de définir les bases

qui permettront d'optimiser les mesures et d'améliorer le dispositif.

Dans le but de réduire le bruit et d'obtenir une mesure plus fine d'une molécule d'Andreev, un protocole a été développé afin d'utiliser des transistors à haute mobilité électronique (HEMT) à des températures proches du millikelvin. La description précise de ce protocole figure dans un chapitre à part, et montre l'utilisation d'un HEMT dans un régime de faible dissipation fonctionnant toujours comme un amplificateur et un isolateur de circuit.

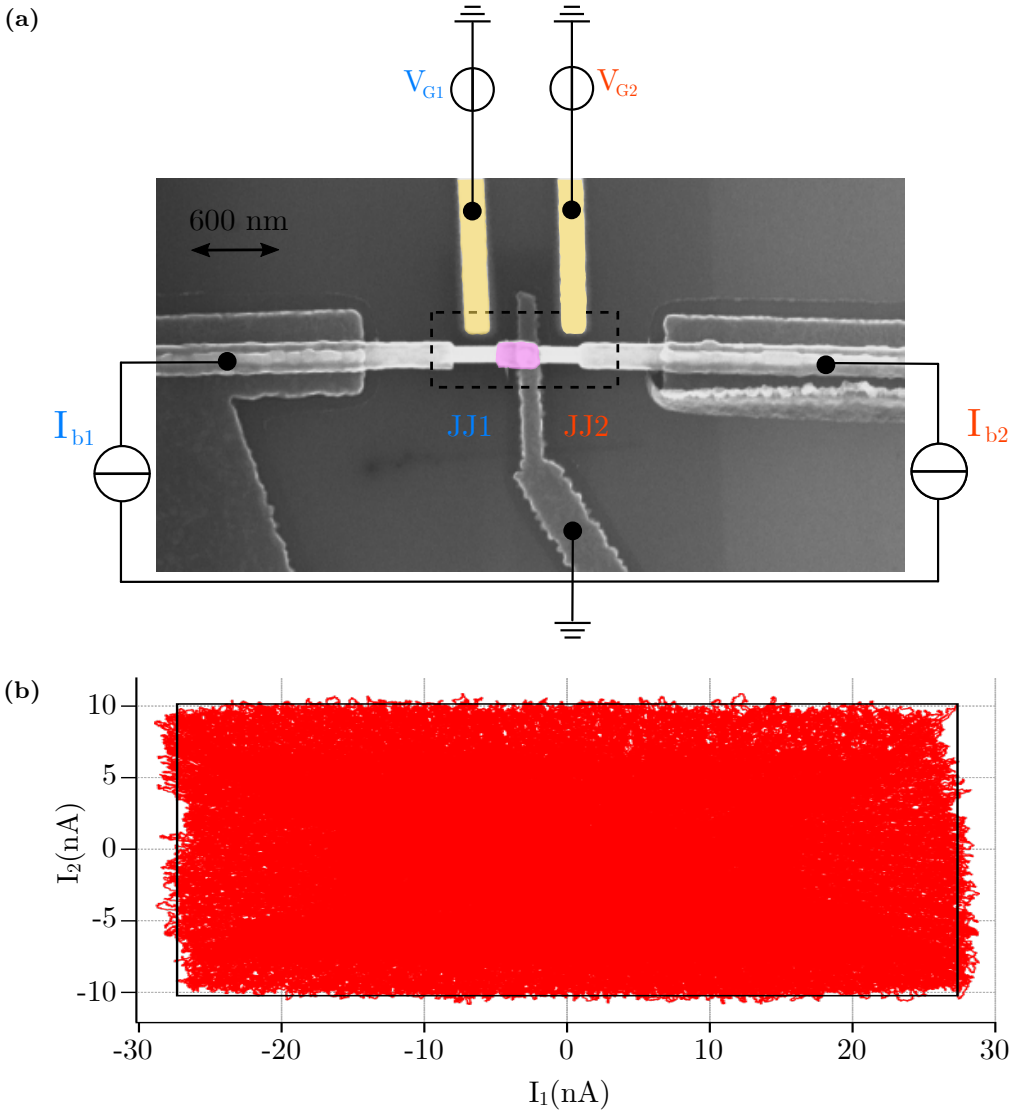

Figure 2: (a) Photo prise au MEB du dispositif AM14 composé de deux jonctions Josephson, JJ1 et JJ2, faites à partir d'un nanofils épitaxié en InAs-Al et séparé par une distance d'approximativement 300 nm. (b) Courant de switching du dispositif AM14 montrant une possible hybridation des états d'Andreev (déformation de la région rouge par rapport au rectangle noir).

Introduction

New physical phenomena often emerge when two interacting objects are juxtaposed. For example, the molecule that forms when two hydrogen atoms are brought within a Bohr radius of each other has modified orbitals, a distinct energy spectrum, and completely different chemical properties. Similarly, when the separation between electrical components is smaller than the electromagnetic wavelength, interference effects modify the circuit response. For electrical components these interactions can become even richer if we add the ingredients of quantum physics. Components can then also be defined with an electronic coherence length which reveals a new dimension for interactions.

One of the most representative quantum electrical components is the Josephson junction. The Josephson effects were theorized in 1962 by Brian Josephson and [1] then observed in the first Josephson junction by Anderson and Rowell [2] in 1963. A Josephson junction is a component made of two superconducting islands separated by a weak link. The weak link is the core of a junction, and carries a supercurrent without being a superconductor. This surprising effect is made possible by Andreev Bound States (ABS). These microscopic bound quasiparticle states, located at the weak link, represent closed paths for the transfer of Cooper pairs from one side of the junction to the other without dissipation. The energy dispersion of ABS depends on the nature of scattering in the weak link as well as the phase difference across it. The myriad possibilities for weak link materials include normal metals, semiconductors, nanowires, nanotubes, graphene, atomic contacts, etc. With a flexible design and the development of sophisticated fabrication techniques, Josephson junctions have become the Swiss Army knife of quantum circuits.

When isolated, junctions obey the Josephson relations and their properties are well understood and exploited in various fields such as magnetometry [3] and metrology [4]. Moreover, due to their quantum coherence and potential for integration in large-scale circuits, Josephson junctions serve as qubits for quantum information and computation [5, 6, 7, 8, 9, 10, 11, 12, 13].

Devices in which two Josephson junctions are brought close to each other can exhibit rich new phenomena. In circuits with typical operating frequencies and propagation velocities, junctions can interact via the electromagnetic field over distances spanning micrometers to centimeters. This interaction is well understood and most often utilized in applications [14]. It is not intrinsic in that it depends entirely on the electromagnetic environment which couples the junctions together. Junctions also affect each other over a length scale of microns via the diffusion of quasiparticles but this is only important close to T_c, the superconducting transition temperature, or at large bias voltages [15]. This process induces modifications of the superconducting energy gap and critical currents.

As the distance between Josephson junctions become comparable to ξ_0, the superconducting coherence length, additional processes emerge. They are due to the overlapping of the wave functions defining the ABS of each junction. An Andreev bound states is a two-level system

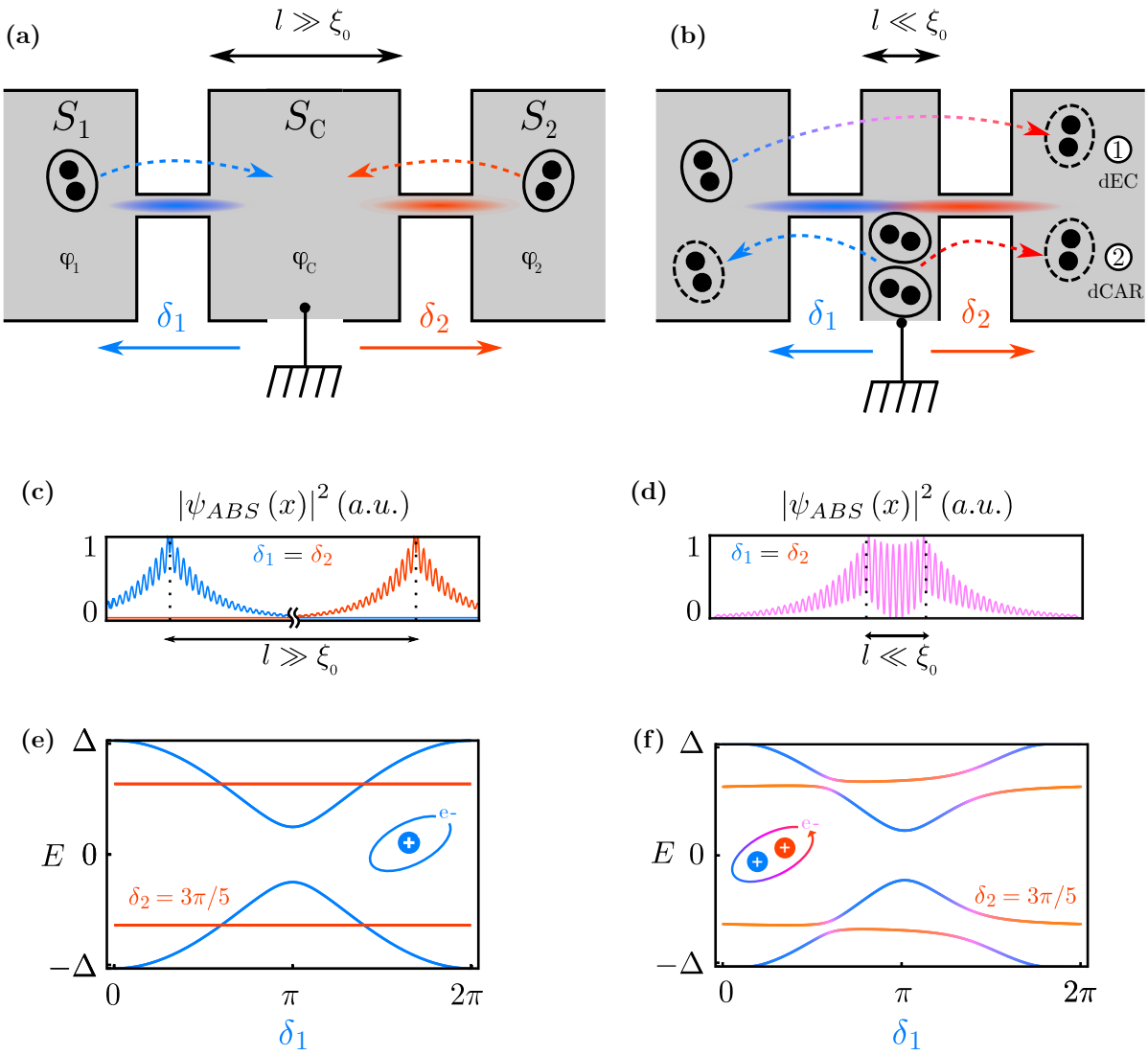

Figure 0.1: Hybridization of closely spaced Josephson junctions. (a) Sketch of two junctions separated by a distance $l \gg \xi_0$. (b) Sketch of an Andreev molecule, in which the Andreev bound states of two junctions separated by a distance $l \ll \xi_0$ hybridize. Two additional non-local mechanisms can transport Cooper pairs: double elastic co-tunneling (dEC) and double-crossed Andreev reflection (dCAR). (c)-(d) ABS wave functions. At large separation, the other wave functions have a negligible overlap. For small separation ($l \ll \xi_0$), the wavefunctions overlap and hybridize (e)-(f) Spectrum of ABS as a function of δ_1 and fixed phase $\delta_2 = 3\pi/5$. Unlike for large separation, in an Andreev molecule, the spectrum displays avoiding crossings which indicate the mixing of states of the two junctions.

analogous to an artificial atom. And similarly to the formation of a molecule, bringing closer two independently controllable Josephson junctions (i.e. ABS) forms an Andreev molecule. This intriguing system has been studied in preceding work in different scenarios. Near T_c, using the Ginzburg-Landau equations, effects resulting from this interaction were calculated [15, 16]. More recently, theorists have investigated this problem at arbitrary temperature using Green's function techniques. Non-local out-of-equilibrium supercurrents were calculated and the existence of π shifts in the current-phase relation was demonstrated [17, 18, 19, 20, 21, 22]. A remarkable phase-locking similar to Shapiro steps was predicted and subsequently measured experimentally in superconducting bi-junctions biased with commensurate voltages [23, 24].

This thesis aims to pursue these interesting works and to explore the Andreev molecule both theoretically and experimentally.

On the theoretical aspects, we proposed a microscopic description of the mechanism responsible for the hybridization of the junctions and studied the fragility of the hybridization in systems with many channels and some disorder. We built an Andreev molecule step by step starting from a single junction (Fig. 0.1(e) and (b)). The next step is the description of the simplest possible Andreev molecule which corresponds to a one-dimensional one-channel molecule using the Bogoliubov-de Gennes equations. The following step is the study of systems closer to potential devices. We used the Landauer-Büttiker formalism to describe a one-dimensional multi-channel Andreev molecule. Finally, using a tight-binding approach we construct a two-dimensional Andreev molecule. This last approach allows adding disorder in the system and studying its effect. The wave functions (Fig. 0.1(c) and (d)), the energy spectrum (Fig. 0.1(e) and (f)) and the current-phase relation calculated from this model gives the expected signatures of an Andreev molecuLe in DC measurements. Furthermore, the explicit dependence of the physical dimensions in these relations aid in the design and fabrication of an Andreev molecule.

Experimentally, we chose to fabricate Josephson junctions based on hybrid semiconductor-superconductor epitaxial InAs-Al nanowires [25] for their suitability in satisfying the constraints identified theoretically (Fig. 0.2(a)). We present the DC measurements performed on this device in Fig. 0.2(b). From the measurements, it appears that the junction separation was not small enough to witness a clear effect and reinforce the crucial importance of the separation size. These initial encouraging results laid the groundwork to optimize the measurement setup and to improve the device.

In the quest to reduce noise and have a more sensitive measurement of an Andreev molecule, we have developed the use of high-electron-mobility transistors (HEMT) at millikelvin temperatures. In a separate chapter, we present the protocol we developed to use a HEMT in a low dissipation regime while continuing to function as an amplifier and circuit isolator.

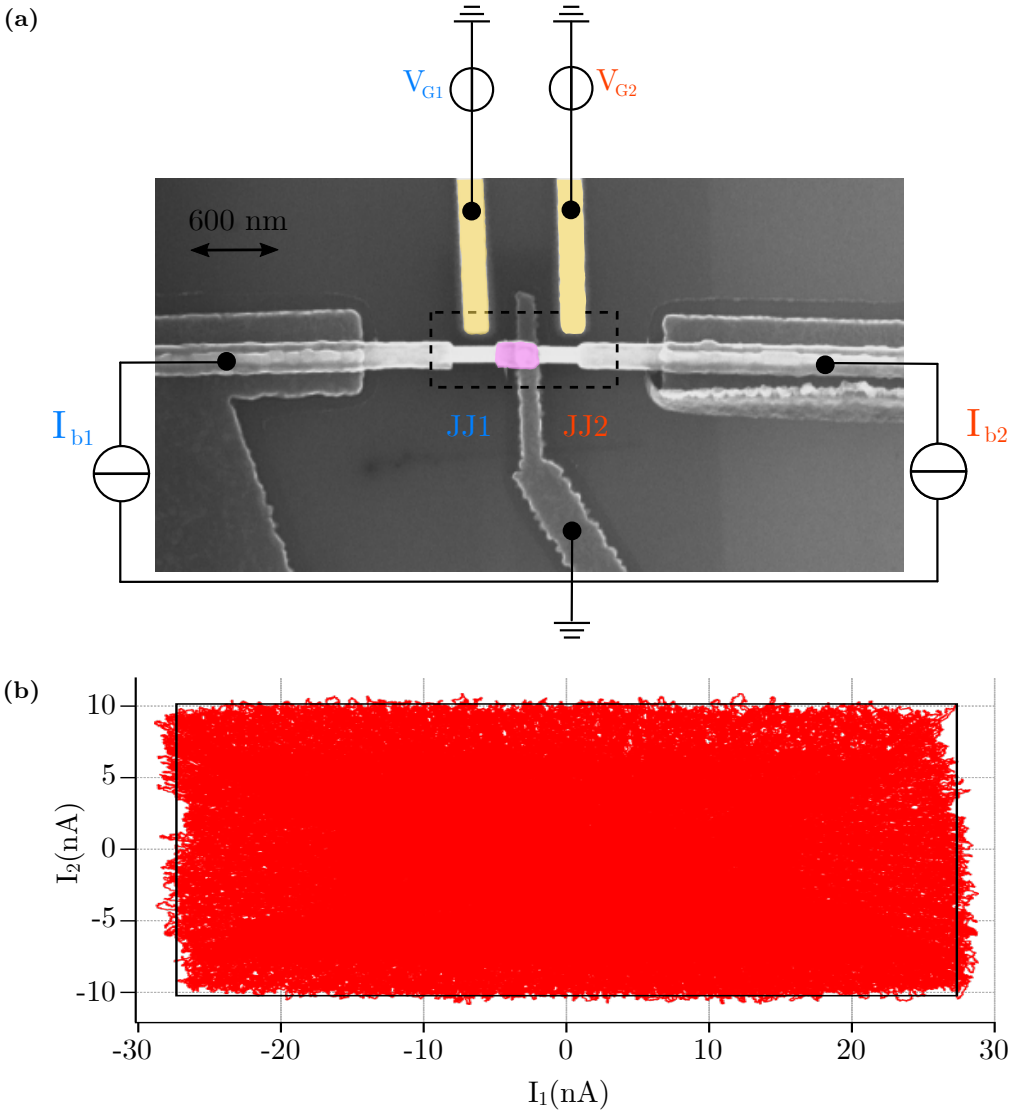

Figure 0.2: (a) SEM image of device AM14 with two Josephson junctions, JJ1 and JJ2, made from an InAs-Al epitaxial nanowire and separated by a distance of approximately 300 nm. (b) Switching current measurement of AM14 hinting at the possibility of hybridization of Andreev states (deformation of red region as compared to black rectangular contour).

1 Theory of hybridized Andreev Bound States: Andreev molecules

The simplest Andreev molecule consists of two closely spaced Josephson junctions which share a common terminal. In this configuration, each Josephson junction is composed of two superconducting electrodes separated by a weak link and one electrode is common to both junctions. The Josephson junctions and the coherent mixing of their localized electronic state, the Andreev Bound States (ABS), are at the core of the Andreev molecule. In this chapter we will theoretically describe the Andreev molecule starting from its building blocks a single Josephson junction carrying Andreev Bound States. We will adopt three different models, each model giving a better understanding of different aspects of the Andreev molecule. The results presented in this chapter come from two articles published by the group [26, 27] and enriched by new findings.

We will first present a macroscopic approach to derive the Josephson effect in a single Josephson junction in one dimension and one channel. We will then carefully add another junction to this system to build the simplest Andreev molecule and then calculate its energy and current of this new system.

In a second step, to depict an Andreev molecule closer to the devices we fabricated, we will be using the Landauer-Büttiker formalism to derive the Josephson effect in a one-dimensional multi-channel single Josephson junction. Then following the same procedure, we will add a second junction to create a multi-channel Andreev molecule and calculate its energy and current. This work will give a microscopic description of the phenomena at the origin of the hybridization.

For the last model using, the tight-binding formalism, we will consider a multi-channel Andreev molecule in two dimensions. This approach will let us understand the robustness of the phenomena against disorder for such hybridized systems. Eventually, we will gather all this theoretical work into practical advice for experimentalists.

1.1 Single-channel Andreev molecule in 1D

In this section, we will describe the Andreev molecule using the most common description for the Josephson junctions, the Bogoliubov-de Gennes formalism.

1.1.1 Andreev Bounds States in a Josephson junction

Consider a Josephson junction in the form of two superconductors S_2 and S_1 coupled through a weak link. Experimentally, this has been realized with superconducting atomic contacts [28, 29] or could be envisioned in semiconducting nanowires epitaxially covered with superconducting

aluminum [30, 31, 32]. The superconducting state of each slab is associated with a phase, respectively ϕ_2 and ϕ_1. A phase difference $\delta = \phi_1 - \phi_2$ is defined across the weak link, as illustrated in Fig. 1.1. Quasiparticles in such a circuit can be described by a 2×2 Hamiltonian H_{SJJ} in a Nambu space:

$$H_{SJJ} = \begin{pmatrix} H_0 + H_{WL} & \Delta(x) \\ \Delta^*(x) & -H_0 - H_{WL} \end{pmatrix} \tag{1.1}$$

where $H_0 = \frac{-\hbar^2}{2m}\partial_x^2 - \mu$ is the single-particle energy (m is the electron mass, μ the chemical potential) and $H_{WL} = U_0\delta(x)$ models scattering at the weak link with amplitude U_0. By using δ-Dirac functions for the scatterer, we limit the analysis to weak links that are shorter than the superconducting coherence length. The off-diagonal terms of the Hamiltonian describe electron pairing in each superconductor,

$$\Delta(x) = \begin{cases} \Delta e^{i\varphi_1} & \text{if } x < 0 \\ \Delta e^{i\varphi_2} & \text{if } x > 0 \end{cases}$$

where the amplitude Δ is constant along the whole device. To find the eigenenergies of this Hamiltonian, we need to use wave functions that are continuous along the x-axis and obey the Bogoliubov-de Gennes (BdG) equation $H_{SJJ}\psi = E\psi$. The spectrum is composed of discrete ABS with energies smaller than the superconducting gap $|E| < \Delta$ and a continuum of states for $|E| > \Delta$.

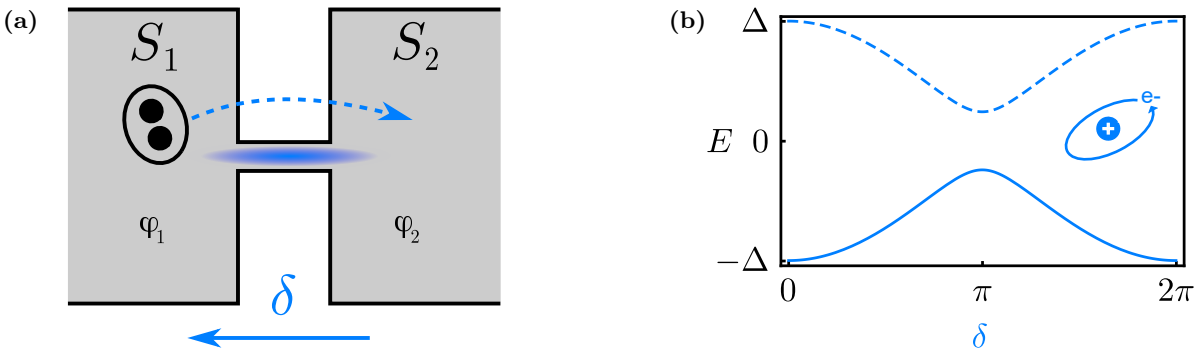

Figure 1.1: (a) A single Josephson tunnel junction defined by two superconductors S_1 and S_2, a weak link and a phase difference δ defined across the weak link following the convention $\delta = \phi_1 - \phi_2$. (b) The weak link hosts localized electronic states called Andreev Bound States (ABS) whose energies periodically depend on the superconducting phase difference. This two-level system can be interpreted as an artificial atom with two levels as represented in blue.

If we consider the cases of the ABS, the sub-gap states respecting the BdG equations for an infinite superconductor are evanescent waves. These solutions are spinors of electron or hole type ($\eta = e$ or h),

$$\psi^{\delta}_{\eta\pm}(x) = \frac{1}{\sqrt{L}}\left(u^{\delta}_{\eta}, v^{\delta}_{\eta}\right)^T e^{\pm i k_\eta x}, \tag{1.2}$$

where L is the total size of the system and we have defined coherence factors,

$$\begin{aligned} u^{\delta}_{e(h)} &= \frac{e^{-i\delta/2}}{\sqrt{2}}\left(1 \pm \sqrt{1-\epsilon^{-2}}\right)^{1/2}, \\ v^{\delta}_{e(h)} &= \mathrm{sign}(\epsilon) \times \frac{e^{i\delta/2}}{\sqrt{2}}\left(1 \mp \sqrt{1-\epsilon^{-2}}\right)^{1/2}, \end{aligned} \tag{1.3}$$

where $k_{e(h)}$ are complex momenta which results in an exponential envelope to the wave function. The coherence factors come from the Bogoliubov transformation which allow to pass from a many-body BCS hamiltonian to a single particle BdG Hamiltonian. If the superconducting gap is much smaller than the Fermi energy $\Delta \ll E_F$, we can use the Andreev approximation which leads to $k_{e(h)} \approx k_F \pm i/\xi$ where k_F is the Fermi momentum in the normal state and the coherence length is a function of energy $\xi^{-1} = \xi_0^{-1}\sqrt{1-\epsilon^2} \ll k_F$. Here $\xi_0 = \hbar v_F/\Delta$ is the bare superconducting coherence length, v_F is the Fermi velocity and $\epsilon = E/\Delta$ is the normalized energy. The wave functions of Andreev molecules are defined piecewise in the following way

$$\psi(x) = \begin{cases} \gamma_{1e}\psi_e^-(x) + \gamma_{1h}\psi_h^+(x) & \text{if } x < 0 \\ \gamma_{2e}\psi_e^+(x) + \gamma_{2h}\psi_h^-(x) & \text{if } x > 0 \end{cases}$$

where we exclude diverging spinors on sides 1 and 2 and we introduce two sets of two coefficients $\Psi_e = (\gamma_{1e}, \gamma_{2e})^T$ and $\Psi_h = (\gamma_{1h}, \gamma_{2h})^T$ give the respective weight of each component (1 for superconductor 1 and 2 for superconductor 2). If we want the solutions of the BdG equations to be physically meaningful, the wave functions have to respect two conditions. Firstly, they must be continuous at the boundary $x = 0$,

$$\psi\left(0^-\right) = \psi\left(0^+\right)$$

with superscript $\pm$ referring to the two sides of the boundary. Secondly, their derivative at the boundary has to be continuous

$$\partial_x\psi\left(0^+\right) - \partial_x\psi\left(0^-\right) = \frac{2m}{\hbar}U_0\psi(0)$$

due to the δ Dirac function that we use to model scattering on the weak link. Continuity and the BdG Hamiltonian impose conditions which give four equations for four unknown coefficients

$$\Psi_e = a(\epsilon)\, A\Psi_h \quad \text{and} \quad \Psi_h = a(\epsilon)\, A^*\Psi_e \tag{1.4}$$

with $a(\epsilon) = e^{-i\arccos\epsilon}$ the probability amplitude for an electron to be Andreev reflected into a hole at the interface between a normal metal and superconductor. The matrix $A(\Phi) = e^{-i\Phi}M^{-1}M^*e^{i\Phi}$ depends on superconducting phase differences contained in the diagonal matrix $\Phi = \mathrm{diag}(\delta_1/2, \delta_2/2)$ and scattering amplitude at the weak links through the matrix M

$$M = \begin{pmatrix} 1 & -1 \\ -u_0^* & -u_0^* \end{pmatrix}$$

with reduced scattering potential

$$u_0 = 1 + iU_0/\hbar v_F,$$

which are directly related to the transmissions of each junction $\tau_0 = 1/|u_0|^2$. Combining the two parts of Eq. 1.4, we have non-trivial solutions only if

$$\mathrm{Det}\left(1 - a(\epsilon)^2 A(\Phi) A^{-1}(-\Phi)\right) = 0. \tag{1.5}$$

The solutions to this last equation are energies E_A where

$$E_A = \pm\Delta\sqrt{1 - \tau_0 \sin^2\left(\frac{\delta}{2}\right)} \tag{1.6}$$

is the Andreev energy for different τ_0 displayed in Fig. 1.2(b). These energy states contribute to the supercurrent passing through the junction from the following equation

$$I^{ABS} = -\frac{1}{\varphi_0}\frac{\partial E_{ABS}}{\partial \delta} = \frac{\Delta}{4\varphi_0}\frac{\tau_0 \sin(\delta)}{\sqrt{1 - \tau_0 \sin^2\left(\frac{\delta}{2}\right)}} \tag{1.7}$$

with $\varphi_0 = \frac{\hbar}{2e}$ the reduced flux quantum, see Fig. 1.2(a). This current exists in the absence of voltage drop across the junction and can be tuned by changing the phase difference δ. In the low transmission limit $\tau_0 \ll 1$, or tunnel limit, this expression simplifies to the DC Josephson relation $I(\delta) = I_0 \sin\delta$, with $I_0 = \Delta\tau_0/4\varphi_0$. The wave function of a quasiparticle occupying an ABS decays exponentially away from it over a distance $\xi = \xi_0/\sqrt{\tau_0}|\sin\frac{\delta}{2}|$, where $\xi_0 = \hbar v_F/\Delta$ is the bare superconducting coherence length and v_F is the Fermi velocity (Fig. 1.5(a)). As with real atoms, ABS form a coherent quantum system with spatially localized wave functions. As a consequence, if ABS are separated by a distance $l \sim \xi$, the overlap of their wave functions leads to their hybridization and the formation of the Andreev artificial molecule.

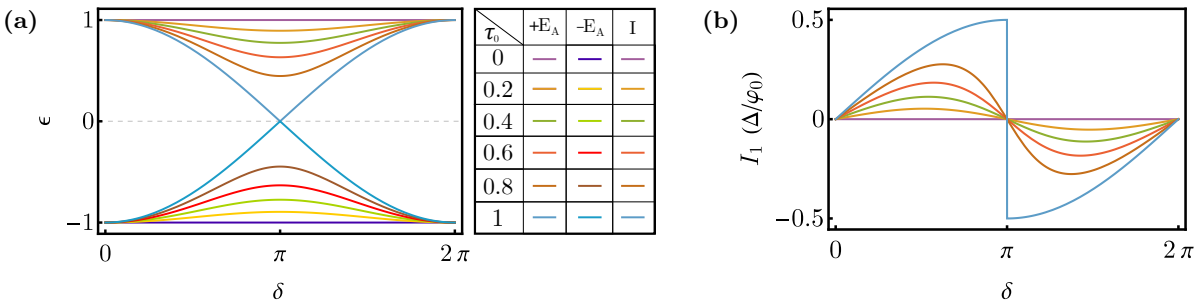

Figure 1.2: (a) The energy spectrum of a single Josephson junction for different values of τ_0.The minimum gap between the ABS is obtained at $\delta = \pi$. (b) The current-phase relation of a single Josephson junction for different values of τ_0. The higher transmissions give larger supercurrents.

1.1.2 BdG description of the Andreev molecule

1.1.2.1 Hamiltonian of the circuit

The simplest Andreev molecule is made of the straightforward Josephson junction, which is composed of two superconductors connected by a one-dimensional quantum conductor with a

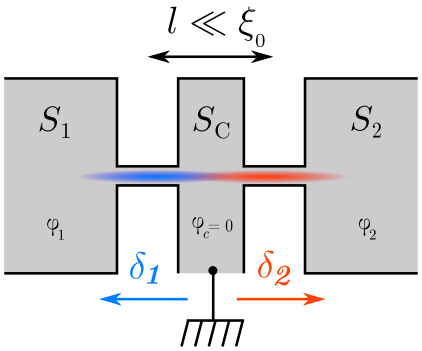

Figure 1.3: Two Josephson junctions separated by a distance $l \ll \xi_0$ which individually hosts an ABS. The first Josephson junction is composed of one outermost and central superconductor S_1 and S_C, and the second junction is composed of the central and the other outermost superconductor S_C and S_2. The two junctions share the central slab which is connected to the ground. Due to the small separation between the junctions, there is an overlap between the ABS hosted by each junction.

single electronic channel as described in the precedent section. From this device, an Andreev molecule can be engineered by connecting in series two of these junctions separated by a short distance l. The resulting device is then composed of three superconductors connected by two closely spaced weak links. Using the derivation from the previous section 1.1.1, we can craft this device by connecting a second junction to the first one. The junctions will share a terminal but will have a distinct phase difference across it due to the connection to ground of the central terminal. As illustrated in Fig. 1.3 and Fig. 1.5(a), by connecting an electrode to the central conductor, one can flow current independently through each junction or apply superconducting phase differences $\delta_{1(2)}$ using magnetic fields. Electrons in such a circuit can be described by a 2×2 Hamiltonian H in Nambu space:

$$H = \begin{pmatrix} H_0 + H_{DWL} & \Delta(x) \\ \Delta^*(x) & -H_0 - H_{DWL} \end{pmatrix}, \tag{1.8}$$

where $H_0 = \frac{-\hbar^2}{2m}\partial_x^2 - \mu$ is the single particle energy (m is the electron mass, μ the chemical potential) and $H_{DWL} = U_1\delta(x + l/2) + U_2\delta(x - l/2)$ models scattering at the weak links with amplitudes $U_{1(2)}$. The off-diagonal terms of the Hamiltonian describe electron pairing in each superconductor,

$$\Delta(x) = \begin{cases} \Delta e^{i\varphi_1} & \text{if } x < -l/2 \\ \Delta & \text{if } |x| < l/2 \\ \Delta e^{i\varphi_2} & \text{if } x > l/2 \end{cases},$$

using the same system but extend Δ is constant along the whole device and by gauge invariance we can choose the phase of the central superconductor to be zero such that $\delta_{1(2)} = \varphi_{1(2)}$. In the one- to few-channel limit considered here the weak link supercurrents are much smaller than the critical currents of the superconducting regions and it is justified to ignore additional spatial variations in the order-parameter amplitude or phase. By connecting a ground electrode to the central conductor, one can flow current independently through each junction or apply

individual phase differences $\delta_{1(2)}$ using magnetic fields. The eigenstates and eigenenergies of H respectively give the orbital states and the spectrum of the Andreev molecule. This minimal model is sufficient to capture the essential features of the nonlocal Josephson effect.

1.1.2.2 Resolution of the Hamiltonian

We use the same strategy as in the last section to solve the system. We build wave functions ψ that are continuous along the x-axis and obey the BdG equation $H\psi = E\psi$, where E is the eigenenergy. The spectrum is composed of discrete ABS with energies smaller than the superconducting gap $|E| < \Delta$ and a continuum of states for $|E| > \Delta$.

• **Sub-gap states $|E| < \Delta$**

The sub-gap states of the BdG equation for an infinite superconductor are evanescent waves. These solutions are spinors of electron or hole type ($\eta = e$ or h), as in Eq. 1.2,

$$\psi^{\delta}_{\eta\pm}(x) = \frac{1}{\sqrt{L}} \left(u^{\delta}_{\eta}, v^{\delta}_{\eta}\right)^{T} e^{\pm i k_{\eta} x}$$

where L is the total size of the system and we have defined coherence factors and $u^{\delta}_{\eta}, v^{\delta}_{\eta}$ are defined similarly as in Eq. 1.3. We also apply the Andreev approximation which decomposes the wave vector into a slow and a fast part. With all the transformation mentioned above, the wave functions of Andreev molecules are defined piecewise in the following way

$$\psi(x) = \begin{cases} \gamma_{1e}\psi^{-}_{e}(x) + \gamma_{1h}\psi^{+}_{h}(x) & \\ \quad \gamma^{+}_{ce}\psi^{+}_{e}(x) + \gamma^{-}_{ce}\psi^{-}_{e}(x) & \\ +\gamma^{+}_{ch}\psi^{+}_{h}(x) + \gamma^{-}_{ch}\psi^{-}_{h}(x) & \\ \gamma_{2e}\psi^{+}_{e}(x) + \gamma_{2h}\psi^{-}_{h}(x) & \end{cases} \begin{array}{ll} & \text{if } x < -l/2 \\ \Big\} & \text{if } |x| < l/2 \\ & \text{if } x > l/2 \end{array}$$

where, as previously, we exclude non-physical diverging spinors on sides 1 and 2 and we introduce two sets of four coefficients $\Psi_e = (\gamma_{1e}, \gamma_{2e}, \gamma^{+}_{ce}, \gamma^{-}_{ce})^{T}$ and $\Psi_h = \left(\gamma_{1h}, \gamma_{2h}, \gamma^{-}_{ch}, \gamma^{+}_{ch}\right)^{T}$ which give the respective weight of each component (1 for superconductor 1, 2 for superconductor 2 and $c^{\pm}$ for the center superconductor). These wave functions must be continous at $x = \pm l/2$, $\psi(\pm l/2^{-}) = \psi(\pm l/2^{+})$. Similarly, the BdG equation imposes boundary conditions on the derivative of ψ

$$\partial_x\psi\left(\pm l/2^{+}\right) - \partial_x\psi\left(\pm l/2^{-}\right) = \frac{2m}{\hbar} U_{2(1)}\psi(\pm l/2)$$

due to the δ Dirac function that we use to model scattering on the weak links. Continuity and the BdG Hamiltonian impose conditions which give eight equations for eight unknown coefficients

$$\Psi_e = a(\epsilon) A \Psi_h \quad \text{and} \quad \Psi_h = a(\epsilon) A^{*} \Psi_e \ , \tag{1.9}$$

with $a(\epsilon) = e^{-i \arccos\epsilon}$ the probability amplitude for an electron to be Andreev reflected into a hole at the interface between a normal metal and superconductor. The matrix $A(\Phi) = e^{-i\Phi} M^{-1} M^{*} e^{i\Phi}$ depends on superconducting phase differences contained in the diagonal matrix $\Phi = \mathrm{diag}(\delta_1/2, \delta_2/2, 0, 0)$ and scattering amplitude at the weak links through matrix M

$$M = e^{ik_F l/2} \begin{pmatrix} i & 0 & -ie^{-ik_e l} & -i \\ 0 & i & -i & -ie^{-ik_e l} \\ -u_1 & 0 & -u_1 e^{-ik_e l} & u_1^* \\ 0 & u_2 & -u_2^* & u_2 e^{-ik_e l} \end{pmatrix}$$

with reduced scattering potential

$$u_{1(2)} = 1 + iU_{1(2)}/\hbar v_F,$$

which are directly related to the transmissions of each junction $\tau_{1(2)} = 1/\left|u_{1(2)}\right|^2$. Combining the two parts of Eq. 1.9 we get

$$\left(1 - a\left(\epsilon\right)^2 A\left(\Phi\right) A^{-1}\left(-\Phi\right)\right) \Psi_e = 0,$$

which has a solution only if $a\left(\epsilon\right)^2 A\left(\Phi\right) A^{-1}\left(-\Phi\right)$ has eigenvalues. So we have non-trivial solutions only if

$$\mathrm{Det}\left(1 - a\left(\epsilon\right)^2 A\left(\Phi\right) A^{-1}\left(-\Phi\right)\right) = 0. \tag{1.10}$$

This is equivalent finding energies for which

$$a\left(\epsilon\right)^2 \lambda_A = 1,$$

where λ_A are eigenvalues of $A\left(\Phi\right) A^{-1}\left(-\Phi\right)$ and $\lambda_A \in U(1)$. Writing equation $\mathrm{Det}\left(A\left(\Phi\right) - \lambda_A A\left(-\Phi\right)\right) = 0$, we can show that λ_A are roots of a symmetric polynomial

$$\alpha_0 \lambda_A^4 + \alpha_1 \lambda_A^3 + \alpha_2 \lambda_A^2 + \alpha_1 \lambda_A + \alpha_0 = 0$$

with coefficients given by

$$\alpha_0 = \left|u_1 u_2 e^{-i2k_F l} - e^{-\frac{2l}{\xi}}\left(u_1 - 1\right)\left(u_2 - 1\right)\right|^2$$

and

$$\begin{cases} \alpha_1 = & -4\alpha_0 + \epsilon_1 \\ \epsilon_1 = & 4e^{-\frac{2l}{\xi}} \sin^2\left(\frac{\delta_2 - \delta_1}{2}\right) \\ & -4\left[\left(1 - e^{-\frac{4l}{\xi}}\right)\left(u_1 - 1\right)^2 + \left(e^{-\frac{2l}{\xi}} - 1\right)\right] \sin^2\left(\frac{\delta_2}{2}\right) \\ & -4\left[\left(1 - e^{-\frac{4l}{\xi}}\right)\left(u_2 - 1\right)^2 + \left(e^{-\frac{2l}{\xi}} - 1\right)\right] \sin^2\left(\frac{\delta_1}{2}\right) \end{cases}$$

and

$$\begin{cases} \alpha_2 = & -2\left(\alpha_1 + \alpha_0 - \epsilon_2\right) \\ \epsilon_2 = & 8\left(e^{-\frac{2l}{\xi}} - 1\right)^2 \sin^2\left(\frac{\delta_2}{2}\right) \sin^2\left(\frac{\delta_1}{2}\right). \end{cases}$$

Since $\lambda_A \in U(1)$ the symmetric polynomial can be simplified to obtain the eigenenergies of the Andreev molecule,

$$\epsilon^2 = 1 - \frac{1}{8\alpha_0}\left(\epsilon_1 \pm \sqrt{\epsilon_1^2 - 8\alpha_0 \epsilon_2}\right). \tag{1.11}$$

In the general case, solutions to this transcendental equation can only be found numerically. It is, however, useful to obtain analytical results in particular cases such as infinitely close ($l \approx 0$) or far junctions ($l \to \infty$). If we consider the limit of large transmission $\tau_0 \to 1$ (or equivalently $u_{1(2)} = 1$), it simplifies into two compact transcendental equations

$$e^{-2\frac{l}{\xi_0}\sin\beta} \sin\frac{\delta_1}{2}\sin\frac{\delta_2}{2} = \sin\left(\frac{\delta_1}{2} \mp \beta\right)\sin\left(\frac{\delta_2}{2} \pm \beta\right) \tag{1.12}$$

where $\beta = -\arccos\epsilon$ and $\epsilon = E/\Delta$, from which one can deduce interesting spectral features. For example, we can recover spectra for well-known particular cases. If the junctions are infinitely far ($l \to \infty$), the left-hand side cancels and we get $\epsilon = \pm\cos\frac{\delta_{1(2)}}{2}$, which are the usual ABS for two independent perfectly transmitted junctions. Similarly, if the junctions are merged into a single one ($l = 0$), we recover the spectrum $\epsilon = \pm\cos\left(\frac{\delta_1-\delta_2}{2}\right)$ of a single junction with a phase drop $\delta_1 - \delta_2$. From the solutions of Eq. 1.10, we generally obtain up to four eigenenergies E_{ABS}, from which we can deduce the contribution of ABS to the supercurrent flowing through the first junction

$$I_1^{ABS} = -\frac{1}{\varphi_0}\sum_{E_{ABS}<0}\frac{\partial E_{ABS}}{\partial\delta_1} .$$

In an Andreev molecule, the energies E_{ABS} depend both on δ_1 and δ_2, which leads to nonlocal phase dependencies of the supercurrent.

• **Continuum states** $|E| > \Delta$

The continuum of Andreev molecules is obtained with a similar approach as for the subgap states but with energies larger than the superconducting gap $|E| > \Delta$. We look for wave functions ψ_E that are continuous along the x-axis and obey the BdG equation $H\psi_E = E\psi_E$, where E is the eigenenergy and H is given by Eq. 1.1. They are built from the eigenstates of an infinite superconductor, which are plane waves of electron or hole type ($\eta = e$ or h)

$$\psi^{\delta}_{\eta\pm}(x) = \frac{1}{\sqrt{L}}\left(u^{\delta}_{\eta}, v^{\delta}_{\eta}\right)^T e^{\pm ik_\eta x}$$

where L is the total size of the system and the coherence factors $u^{\delta}_{\eta}, v^{\delta}_{\eta}$ are defined similarly as in Eq. 1.3.

The main difference with the preceding treatment is the form of the wave vectors $k_{e(h)}$ which do not contain any imaginary part since the solutions are only propagating states. Assuming $\Delta \ll E_F$, we can make the Andreev approximation. Here $\xi_0 = \hbar v_F/\Delta$ is the bare superconducting coherence length, v_F is the Fermi velocity and $\epsilon = E/\Delta$ is the normalized energy. Since momenta k_η are real, there is no bound states but only propagating solutions called scattering states. They are superpositions of an incoming wave and an outgoing wave resulting from scattering at the weak links

$$\psi^{\eta\pm}_E = \psi^{\eta\pm}_{inc}(x) + \psi^{\eta\pm}_{out}(x) \tag{1.13}$$

with four possible types of incoming wave (here Θ is the Heaviside step function)

$$\begin{aligned}
\psi^{e+}_{inc}(x) &= \psi^{\delta_1}_{e+}(x)\,\Theta[-x-l/2]\\
\psi^{e-}_{inc}(x) &= \psi^{\delta_2}_{e-}(x)\,\Theta[x-l/2]\\
\psi^{h+}_{inc}(x) &= \psi^{\delta_2}_{h+}(x)\,\Theta[x-l/2]\\
\psi^{h-}_{inc}(x) &= \psi^{\delta_1}_{h-}(x)\,\Theta[-x-l/2]
\end{aligned}$$

and resulting outgoing wave

$$\psi_{out}^{\eta\pm}(x) = \begin{cases} c_1^{\eta\pm}\psi_{e-}^{\delta_1}(x) + c_2^{\eta\pm}\psi_{h+}^{\delta_1}(x) & \text{for } x < -\frac{l}{2} \\ \left.\begin{array}{l} c_3^{\eta\pm}\psi_{e-}^{0}(x) + c_4^{\eta\pm}\psi_{h+}^{0}(x) \\ +c_5^{\eta\pm}\psi_{e+}^{0}(x) + c_6^{\eta\pm}\psi_{h-}^{0}(x) \end{array}\right\} & \text{for } |x| < \frac{l}{2} \\ c_7^{\eta\pm}\psi_{e+}^{\delta_2}(x) + c_8^{\eta\pm}\psi_{h-}^{\delta_2}(x) & \text{for } x > \frac{l}{2} \end{cases}$$

For each type of incoming wave, we have a set of eight coefficients

$$\Psi_E^{\eta\pm} = \left(c_1^{\eta\pm}, c_2^{\eta\pm}, c_3^{\eta\pm}, c_4^{\eta\pm}, c_5^{\eta\pm}, c_6^{\eta\pm}, c_7^{\eta\pm}, c_8^{\eta\pm}\right)^T$$

giving the respective weights for the outgoing wave on the three superconductors. The continuity of the wave functions and the conditions imposed on their derivatives by the BDG equation [33] give the relations

$$\Psi_E^{\eta\pm} = -M_E^{-1}\Psi_{inc}^{\eta\pm} \tag{1.14}$$

where M_E is a 8×8 matrix given

$$M_E = \begin{pmatrix} m_{\delta_1}m_k^+ & -m_k^+ & -m_k^- & 0_2 \\ 0_2 & -m_k^- & -m_k^+ & m_{\delta_2}m_k^+ \\ m_{\delta_1}m_k^+m_u^1 & -m_k^+m_u^{1*} & m_k^-m_u^1 & 0_2 \\ 0_2 & m_k^-m_u^2 & -m_k^+m_u^{2*} & m_{\delta_2}m_k^+m_u^2 \end{pmatrix}$$

where 0_2 are 2×2 matrix of zeros and we define three submatrices depending on the parameters of the device

$$m_u^{1(2)} = \begin{pmatrix} u_{1(2)} & 0 \\ 0 & -u_{1(2)}^* \end{pmatrix}, \quad m_\delta = \begin{pmatrix} e^{\frac{i\delta}{2}} & 0 \\ 0 & e^{-\frac{i\delta}{2}} \end{pmatrix}$$

$$m_k^\pm = \begin{pmatrix} e^{\pm\frac{ik_el}{2}} & a(\epsilon)\, e^{\mp\frac{ik_hl}{2}} \\ a(\epsilon)\, e^{\pm\frac{ik_el}{2}} & e^{\mp\frac{ik_hl}{2}} \end{pmatrix}.$$

The vectors $\Psi_{inc}^{\eta\pm}$ can have four different forms depending on the nature of the incoming waves (e or h) and their directions of propagation ($+$ for $x>0$ and $-$ for $x<0$)

$$\Psi_{inc}^{e+} = e^{-i\frac{k_el+\delta_1}{2}}\begin{pmatrix} e^{i\delta_1} \\ a(\epsilon) \\ 0 \\ 0 \\ -u_1^*e^{i\delta_1} \\ -u_1^*a_\epsilon \\ 0 \\ 0 \end{pmatrix}, \Psi_{inc}^{e-} = e^{-i\frac{k_el+\delta_2}{2}}\begin{pmatrix} 0 \\ 0 \\ e^{i\delta_2} \\ a(\epsilon) \\ 0 \\ 0 \\ -u_2^*e^{i\delta_2} \\ -u_2^*a(\epsilon) \end{pmatrix}$$

$$\Psi_{inc}^{h-} = e^{i\frac{k_h l-\delta_1}{2}} \begin{pmatrix} a(\epsilon)e^{i\delta_1} \\ 1 \\ 0 \\ 0 \\ u_1 a(\epsilon)e^{i\delta_1} \\ u_1 \\ 0 \\ 0 \end{pmatrix}, \Psi_{inc}^{h+} = e^{i\frac{k_h l-\delta_2}{2}} \begin{pmatrix} 0 \\ 0 \\ a(\epsilon)e^{i\delta_2} \\ 1 \\ 0 \\ 0 \\ u_2 a(\epsilon)e^{i\delta_2} \\ u_2 \end{pmatrix}$$

with $a(\epsilon)$ the probability amplitude for an electron of normalized energy ϵ to be Andreev reflected at the interface between a normal metal and a superconductor. This gives then four degenerate states for each energy ϵ. The solutions obtained from Eq. 1.13 with sets of coefficients 1.14 can therefore be written in the following way

$$\psi_E^{\eta\pm}(x) = \frac{1}{\sqrt{L}} \begin{pmatrix} U_E^{\eta\pm}(x) \\ V_E^{\eta\pm}(x) \end{pmatrix},$$

where $U_E^{\eta\pm}$ is the electron part and $V_E^{\eta\pm}$ is the hole part of the wave functions. In one dimension and at zero temperature, the current at equilibrium carried by these states is given by [34, 35]

$$I(x) = \frac{2e\hbar}{mL} \sum_{\eta,\sigma} \sum_{|k|>k_F} \mathrm{Im}\left[V_E^{\eta\sigma}(x)^* \partial_x V_E^{\eta\sigma}(x)\right].$$

The current flowing through the first junction is obtained by evaluating this expression at $x = -l/2$. We substitute the sum by an integral $\sum_k \to \int_k dk \times L/2\pi$ and sum over energy rather than momentum by making use of $d\xi_k/dk \approx \hbar^2 k_F/m$ and $d\xi_k/dE = \epsilon/\sqrt{\epsilon^2-1}$ where ξ_k is the kinetic energy. The current carried by the continuum through the first junction is therefore given by

$$I_1^{cont} = \frac{1}{\varphi_0} \sum_{\eta\sigma} \int_\Delta^\infty \frac{dE}{2\pi k_F} \frac{E}{\sqrt{E^2-\Delta^2}} \mathrm{Im}\left[V_E^{\eta\sigma}\left(-\frac{l}{2}\right)^* \partial_x V_E^{\eta\sigma}\left(-\frac{l}{2}\right)\right]$$

where φ_0 is the reduced flux quantum. The current through the second junction I_2 is obtained similarly by taking $x = +l/2$.

1.1.3 Wave functions and spectra of Andreev molecules

Once we have solved for the eigenenergies, we obtain the Andreev molecule wave functions from Eq. 1.9. These wave functions arise from the hybridization of the independent ABS at each junction. As with real atoms, ABS form a coherent quantum system with spatially localized wave functions. As a consequence, if ABS are separated by a distance $l \sim \xi$, the overlap of their wave functions leads to their hybridization and the formation of the Andreev artificial molecule. Two microscopic mechanisms underlie this process: (i) double elastic cotunneling of Cooper pairs (dEC) and (ii) double-crossed-Andreev reflections (dCAR). As pictured in Fig. 1.4(a), the supercurrent in a single Josephson junction corresponds to the elastic tunneling of Cooper pairs from one superconducting electrode to the other directly linked by that junction. For two junctions which are located close to each other (Fig. 1.4(b)), Cooper pairs can also

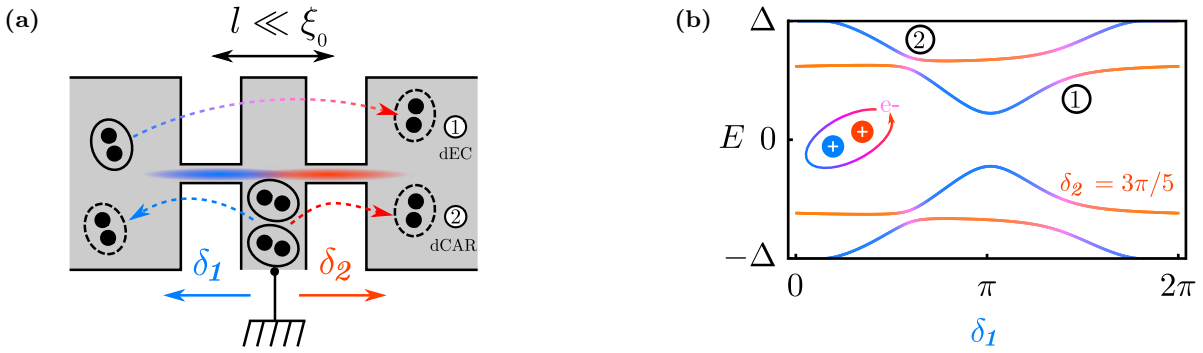

Figure 1.4: (a) When two junctions are placed in close proximity, the ABS wave functions overlap. In this three-electrode geometry, where phases δ_1 and δ_2 can be controlled independently, two new non-local mechanisms carry the supercurrent: double elastic cotunneling (dEC) and double-crossed Andreev reflection (dCAR). (b) The spectrum of the device, plotted for varying δ_1 and fixed $\delta_2 = 3\pi/5$, shows avoided crossings which indicate the formation of Andreev molecules by hybridization of the individual ABS. ABS as two-level systems can be interpreted as artificial atoms. By bringing these atoms together an artificial molecule made of Andreev Bound States is formed. An analogy can be made with the formation of a dihydrogen molecule originating from the hybridization of two hydrogen atoms.

be transferred directly across the whole device (dEC,Fig. 1.4(b) top, 1). In contrast, dCAR (Fig. 1.4(b)) bottom, 2), is the joint splitting of two Cooper pairs in the center of the device and their crossed recombination in the two outermost electrodes. These processes respectively confer $\delta_1 - \delta_2$ and $\delta_1 + \delta_2$ dependence to the energy spectra. As a corollary, current due to dEC flows in one direction between the two outermost electrodes, whereas dCAR consists in two counterpropagating currents from the central electrode outwards. Without electrical connection to the central superconductor, dCAR processes are not possible. When the independent ABS energies are degenerate, their wave functions may be spread out over both junctions.

Fig. 1.5(a) and (c) show a one-dimensional single-channel conductor with weak links separated by a distance l, a device which can be fabricated from epitaxially coated superconducting nanowires [25]. For l comparable to ξ_0, the wave functions hybridize as shown in Fig. 1.5. In the general case, degeneracy occurs when a Snell's law like condition, $\sqrt{\tau_1}\sin(\delta_1/2) = \pm\sqrt{\tau_2}\sin(\delta_2/2)$ is satisfied. For the case of symmetric junctions considered here, this equation takes the simple form $\delta_1 = \mp\delta_2 \pmod{2\pi}$. For $\delta_1 = -\delta_2$, corresponding to dEC, the wave function has a significant weight in the central superconductor. On the contrary, for the dCAR process at $\delta_1 = \delta_2$ the wave functions are zero at the origin and peak at the positions of the weak links. For infinitely far junctions ($l \gg \xi_0$), these two processes are negligible and the wave functions are localized at one of the junctions (Fig. 1.5(c) and (d)) and correspond to distinct, non-overlapping pairs of ABS. As expected the spectrum is that of two isolated junctions (Eq. 1.6). Only local tunneling of Cooper pairs occurs and there is no non-local Josephson effect.

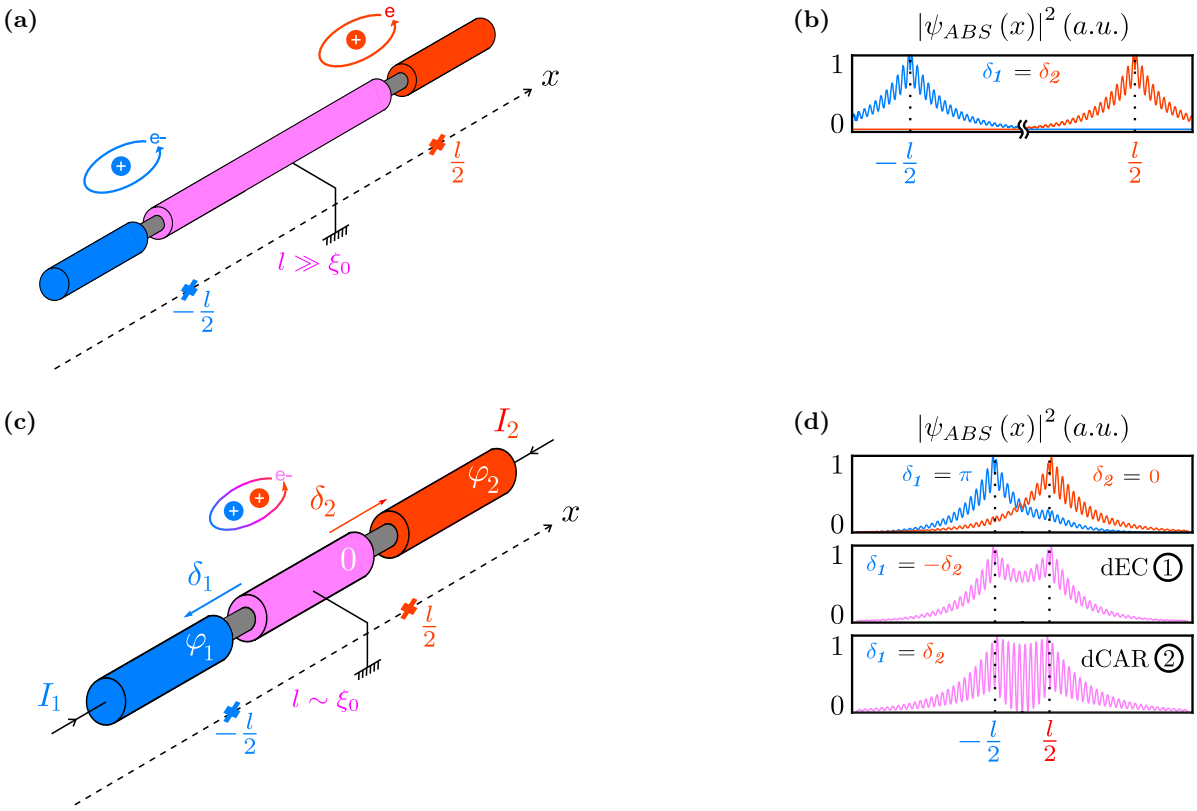

Figure 1.5: Andreev molecule wave functions in a one-dimensional device. (c) and (a) A single-channel conductor (gray) with superconducting regions (blue, magenta, red) defining two Josephson junctions respectively separated by a distance $l \sim \xi_0$ and $l \gg \xi_0$. (d) For large separation ($l = 10\xi_0$), there is essentially no hybridization and the junctions remain independent artificial atoms. When ABS are almost degenerate ($\delta_1 = 0.99\delta_2$), the wave functions are localized separately on the two weak links. The parameters chosen for calculations are $U_1 = U_2 = 0.25\hbar v_F$ ($\tau_1 = \tau_2 \approx 0.94$), $\delta_2 = 3\pi/5$ and $k_F\xi_0 = 10\pi$. The square modulus is defined as $|\psi_{ABS}|^2 = |u|^2 + |v|^2$, where u and v are the electron and hole components of ψ_{ABS}. (b) Plot of the last occupied ABS wave functions for small separation ($l = \xi_0$). For $\delta_1 = \pi$ or $\delta_1 = 0$ the wave functions are localized to one side. When dEC or dCAR are dominant processes, the ABS hybridize and the wave function is spread out over both junctions.

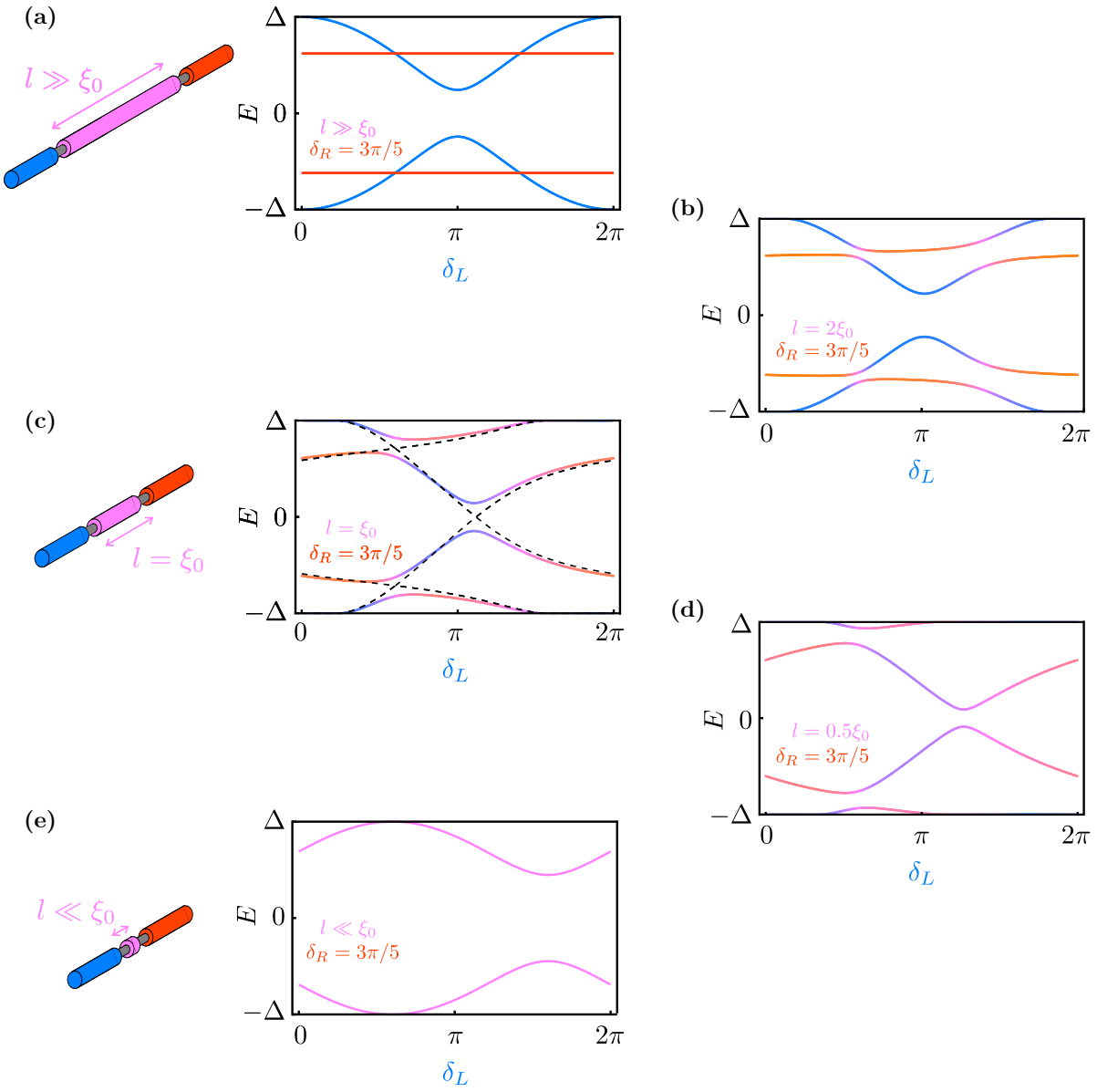
(a)
$l \gg \xi_0$
Δ
E
0
$-\Delta$
$l \gg \xi_0$
$\delta_R = 3\pi/5$
0
π
2π
δ_L
(b)
Δ
E
0
$-\Delta$
$l = 2\xi_0$
$\delta_R = 3\pi/5$
0
π
2π
δ_L
(c)
$l = \xi_0$
Δ
E
0
$-\Delta$
$l = \xi_0$
$\delta_R = 3\pi/5$
0
π
2π
δ_L
(d)
Δ
E
0
$-\Delta$
$l = 0.5\xi_0$
$\delta_R = 3\pi/5$
0
π
2π
δ_L
(e)
$l \ll \xi_0$
Δ
E
0
$-\Delta$
$l \ll \xi_0$
$\delta_R = 3\pi/5$
0
π
2π
δ_L

Figure 1.6: *(previous page)* Spectra of Andreev molecules for varying separation. (a) For $l \gg \xi_0$, energies of ABS in the first junction (blue lines) modulate with δ_1 (x-axis) while those of the second junction are constant (red lines). (b-c-d) When the junction separation l is comparable to ξ_0, the ABS hybridize among each other, leading to the appearance of avoided crossings which grow as l decreases. Colors indicate relative localization of the wave function on the weak links (left: blue, right: red, center: magenta). The extremal ABS are gradually pushed into the continuum ($|E| > \Delta$) as a result of hybridization. The dashed line in the graph (c) ($l = \xi_0$) shows the spectrum for $U_1 = U_2 = 0$ ($\tau_1 = \tau_2 = 1$), where dCAR splitting is absent. (e) For $l \ll \xi_0$, the two junctions merge into a single one, leaving only one pair of ABS. Parameters used for these calculations are $U_1 = U_2 = 0.25\hbar v_F$ ($\tau_1 = \tau_2 \approx 0.94$), $\delta_2 = 3\pi/5$ and the Fermi momentum is chosen such that $k_F l \gg 1$ and $k_F l = \pi/2$ (mod2π), maximizing the avoided crossings at $\delta_1 = \delta_2$.

Fig. 1.6(a) to 1.6(e) shows how the spectrum evolves, for fixed $\delta_2 = 3\pi/5$, as the junction separation is reduced from $l = \infty$ to $l = 0$. For moderate distance, $l = 2\xi_0$, ABS of the first and second junction start to hybridize into bonding and anti-bonding states producing avoided crossings around the points of degeneracy where dEC or dCAR is optimal (respectively at $\delta_2 = \mp\delta_1$ for symmetric junctions). In the particular case of weak links with perfect transmissions ($\tau_2 = \tau_1 = 1$), avoided crossings disappear at $\delta_1 = \delta_2$ where the dominant nonlocal process is dCAR.

As explained in Section 1.2, this process relies on the interconversion of electrons and holes propagating in the same direction and requires backscattering, which is suppressed for $\tau_0 = 1$. In contrast avoided crossings at $\delta_1 = -\delta_2$ produced by dEC, a momentum conserving process, are preserved for $\tau_0 = 1$. The inequivalence of the two processes of dEC and dCAR lead to the unusual asymmetry about $\delta_1 = \pi$ in the spectra for fixed δ_2. Such asymmetry, absent in the spectra of isolated junctions, is permitted by time-reversal invariance which only requires $E(\delta_1, \delta_2) = E(-\delta_1, -\delta_2)$ and not $E(\delta_1, \delta_2) = E(-\delta_1, \delta_2)$. As the junction separation is reduced, the size of the avoided crossings increases until some of the ABS are partially pushed out from the superconducting gap into the continuum. For any state with $|E| > \Delta$ the momentum $k_{e(h)}$ must be real and therefore the corresponding ABS are no longer localized for all values of the phase difference. These non-evanescent "leaky" Andreev states [36], which also exist in asymmetric gap Josephson junctions, can make an important contribution to the total supercurrent in Andreev molecules and significantly affects the nonlocal Josephson effect, but unlike ABS they are delocalized plane waves [37, 38, 39].

Another interesting phenomenon that results from level repulsion due to hybridization is the reduction in the gap between ABS around zero energy ($\delta_1 \approx 4\pi/3$) in the spectrum Fig. 1.6(d) for $l = 0.5\xi_0$. This gap is smaller than both the unhybridized gap at $\delta_1 = \pi$ in the case of separate junctions ($l/\xi_0 \gg 1$, Fig. 1.6(a)) and the gap at $\delta_1 = \pi + \delta_2$ in the case of fused junctions ($l/\xi_0 \ll 1$, Fig. 1.6(e)). This can be explained by the competition between scattering, which pushes the innermost spectral lines away from zero energy, and molecular hybridization due to dEC ($\delta_1 = -\delta_2$), which pushes them inward. When the distance l becomes negligible compared to ξ_0, the two junctions fuse into a single junction with twice the scattering amplitude and one pair of ABS pushed entirely into the continuum. Instead of having two junctions in

series with transmissions $\tau_0 \approx 0.94$ at large separation $l \gg \xi_0$, there is now a single junction with a larger scattering amplitude $U_1 + U_2$ (or equivalently a smaller transmission $\tau_0' \approx 0.8$) and an additional continuum state. The spectrum, shown in Fig. 1.6(e), is effectively that of a single junction of transmission τ_0' shifted by $\delta_2 = 3\pi/5$ to account for the fact that the total phase drop is $\delta = \delta_1 - \delta_2$. The mechanism of dCAR is no longer possible since there is no central superconducting electrode and dEC is simply transformed into regular tunneling. The two cases $l \gg \xi_0$ and $l \ll \xi_0$ are conventional in that the nonlocal mechanisms are absent and that the energy spectrum can be described by the single-junction expression Eq. 1.6, albeit with different transmissions and a shift in phase.

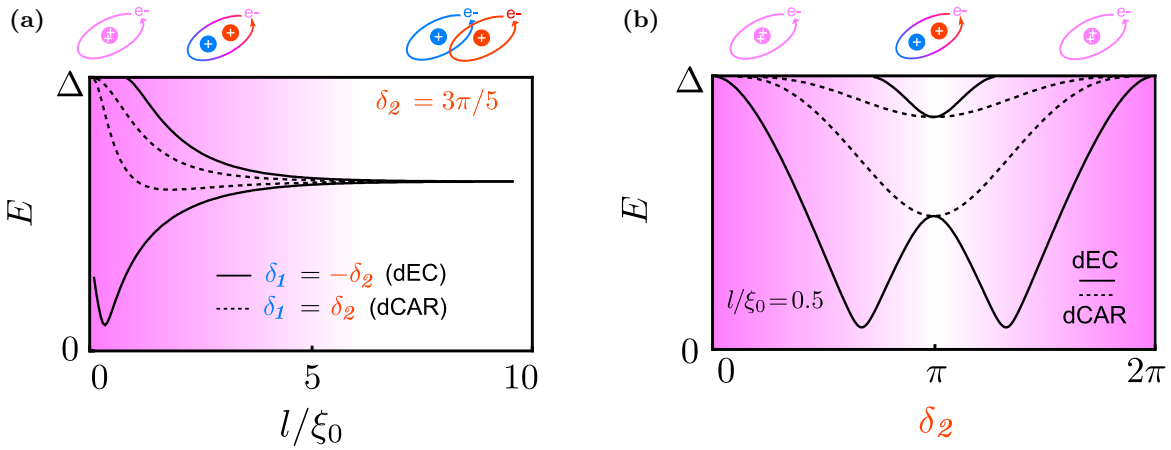

Figure 1.7: From artificial atoms to molecules and fusion. (a) Continuous evolution of the positive part of the spectrum at the avoided crossings $\delta_1 = -\delta_2$ (dEC, solid lines) and $\delta_1 = \delta_2$ (dcar, dashed lines) as a function of l/ξ_0 for fixed $\delta_2 = 3\pi/5$. at large separation, ABS are degenerate and each junction behaves as an artificial atom with only one state below the energy gap δ. As the separation is reduced, these atoms hybridize to form a molecule, indicated by the splitting due to dEC and dCAR, and eventually fuse into a single new artificial atom leaving only one sub-gap state. (b) The strength of hybridization can be controlled by adjusting δ_2. Here we see a transition from an Andreev molecule, near $\delta_2 = \pi$, where there are two possible positive-energy states (pair of dashed or solid lines), to a single artificial atom near $\delta_2 \approx 0 \pmod{2\pi}$. Parameters used for these calculations are $u_1 = u_2 = 0.25\hbar v_f$ ($\tau_1 = \tau_2 \approx 0.94$), $\delta_2 = 3\pi/5$ and $k_f l = \pi/2 \pmod{2\pi}$ with $k_f l \gg 1$.

The transition from two independent artificial atoms to a single one with an intermediate molecular state can be visualized in Fig. 1.7(a) where only the positive spectral lines for $\delta_1 = \pm\delta_2$ are plotted as l/ξ_0 is varied for fixed $\delta_2 = 3\pi/5$. At large separation $l/\xi_0 \gg 1$ all positive ABS converge to the same energy, $E^+(\delta = \pm 3\pi/5, \tau_0) \approx 0.62\Delta$. For the dominant dEC mechanism at $\delta_1 = -\delta_2$ (solid lines), with decreasing l/ξ_0 the two degenerate ABS of the two junctions gradually split to form bonding and anti-bonding molecular states until the higher-energy ABS escapes into the continuum. Beyond that point the device hosts only one pair of ABS, symmetric in energy, such that it behaves as a single artificial atom rather than a molecule. Incidentally, around this transition from molecule to atom, the lower ABS reaches a minimum

resulting in an overall shape which suggests the interatomic potentials used to describe the formation of molecules. Physically, this minimum corresponds to the point where the single quasiparticle occupying the lower ABS has been maximally localized and isolated from the continuum. At $l/\xi_0 = 0$, in contrast to a real interatomic potential, the energy of this lower state does not diverge and is smaller than the energy at large separation, $l/\xi_0 \to \infty$. On the other hand, for $\delta_1 = \delta_2$ (dashed lines) dCAR is the dominant mechanism. The corresponding ABS hybridize as l/ξ_0 decreases and then escape into the continuum, leaving no discrete states for small l/ξ_0. As the size l of the central superconductor approaches zero, the probability for dCAR to happen shrinks to zero and, since the effective phase difference becomes zero, the bound states enter the continuum. The strength of the two mechanisms dEC and dCAR can be adjusted by tuning δ_2 as shown in the spectra of Fig. 1.7(b), where the junction separation is fixed at $l/\xi_0 = 0.5$. Different regimes can be identified by the number of ABS. For δ_2 increasing from 0 to π at first, there is only a single dEC line, which is then joined by two dCAR lines whose splitting increases with δ_2, and then finally by a second dEC line near π. The dCAR splitting, or hybridization strength, is maximal at $\delta_2 = \pi$ whereas for dEC this maximum splitting occurs at the point where the second dEC line passes below the gap approaching $\delta_2 = \pi$, and then decreases as δ_2 goes to π. By changing δ_2 one can thus control the degree of hybridization or the molecular nature of the system. These properties could be exploited for quantum simulations of elaborate molecules, including those with strong Coulomb repulsion since one could use weak links with large charging energy such as carbon nanotubes [40, 41, 42, 43]. In addition this tunable multi-level qubit may have applications for quantum information. It is also possible that the ability to tune levels into the continuum may be useful for preparing or resetting quantum states.

1.1.4 Signatures of Andreev molecules

The formation of an Andreev molecule dramatically modifies the Josephson effect. The three-terminal devices we described in previous sections are not simply a series connection of two-terminal devices.

For two closely spaced junctions, the supercurrent through the first junction I_1 will also depend on the phase drop across the second junction δ_2, making it possible to obtain φ-junctions. A φ-Joseph junctions are junctions which have a non-zero phase difference δ in the ground state or, equivalently, which have a non-zero supercurrent when $\delta = 0$. A particular case of known φ-junctions are the π-junctions which have a phase difference $\delta = \pi$ in their ground state. This behavior results from the unusual asymmetry in the spectrum of Fig. 1.6 with respect to $\delta_1 = 0$ or π. For an isolated Josephson junction (Fig. 1.8(a)), the spectrum is always symmetric and therefore, according to Eq. 1.7, the supercurrent cancels at these points. In particular, unless the weak link breaks time-reversal symmetry such that $I_1(-\delta_1) \neq -I_1(\delta_1)$, there is no zero-phase supercurrent: $I_1(\delta_1 = 0) = 0$ [44]. However when two junctions are close enough for an Andreev molecule to form their current-phase relations depends on two phases. In this case, time-reversal symmetry imposes $I_1(-\delta_1, -\delta_2) = -I_1(\delta_1, \delta_2)$, which means that the current $I_1(\delta_1, \delta_2)$ does not need to cancel at $\delta_1 = 0$ if δ_2 it is non-zero. In an Andreev molecule, the total supercurrent can be divided in two contributions: one from the ABS I_1^{ABS} and one from the continuum I_1^{cont} such that $I_1 = I_1^{ABS} + I_1^{cont}$. The ABS contribution to the supercurrent flowing through the first junction is obtained similarly to the case of a single

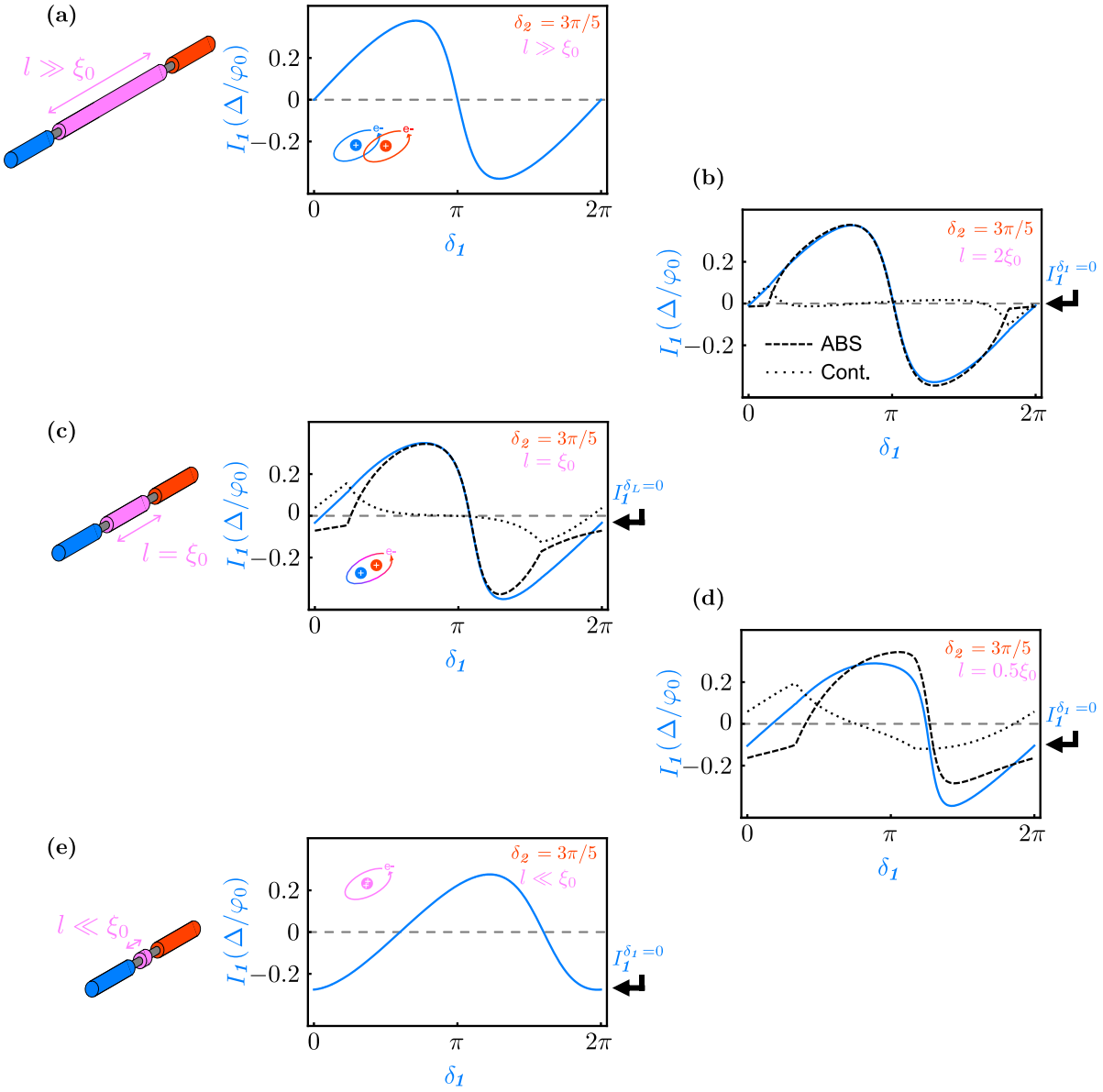

Figure 1.8: Current-phase relation of Andreev molecules. (a) For infinitely far junctions, the current-phase relation $I_1(\delta_1)$ is identical to that of a single junction. (b-c-d) As the junction separation l approaches ξ_0, the current-phase relation is modified. It shifts to the right such that a 0-phase supercurrent $I_1^{\delta_1}$ appears and the amplitude decreases. Both ABS and the continuum contribute significantly when $l \sim \xi_0$, which is unusual in the short limit. (e) When junctions merge into a single one, the current-phase relation of the first junction is shifted by δ_2. Parameters used for these calculations: $U_1 = U_2 = 0.25\hbar v_F$ ($\tau_1 = \tau_2 \approx 0.94$), $\delta_2 = 3\pi/5$ and $k_F l = \pi/2$ (mod 2π) with $k_F l \gg 1$.

junction

$$I_1^{ABS}(\delta_1, \delta_2) = -\frac{1}{\varphi_0} \sum_{E_{ABS}<0} \frac{\partial E_{ABS}}{\partial \delta_1} \tag{1.15}$$

where we sum over all the ABS of negative energy E_{ABS}.

Fig. 1.8(a) to (e) show current-phase relations of the first junction $I_1(\delta_1)$ for a fixed superconducting phase difference δ_2 across the second junction and for different values of the separation l. We observe that the curve gradually shifts to the right as l decreases (from top to bottom). As a result of this shift, the current cancels at $\delta_1 = \varphi(\delta_2)$ rather than at $\delta_1 = 0$. When the current carried by the continuum is negligible and for junctions with large transmission ($\tau_0 \sim 1$), the shift $\varphi(\delta_2)$ is given by $\varphi \approx 2\arctan\left[e^{-2l/\xi_0}\tan(\delta_2/2)\right]$ simplifying Eq. 1.12, which becomes $\varphi = \delta_2$ for infinitely close junctions ($l = 0$), Fig. 1.8(e). As a consequence, the current flowing through the first junction is finite as soon as $\delta_2 \neq 0$ even though no phase is applied across it ($\delta_1 = 0$). The existence of a non-zero supercurrent at zero phase difference, which we denote $I_1^{\delta_1=0}$, is the signature of a φ-junction. The sign of $I_1^{\delta_1=0}$ for small φ is negative, indicating that the current flows in the same direction as the phase difference δ_2 from electrodes S_1 and S_C in 1.4(a). The φ-supercurrent $I_1^{\delta_1=0}$ increases exponentially as the junction separation becomes small compared to ξ_0 and converges to zero for large l with an oscillatory behavior (Fig. 1.8). These oscillations have a period $\sim \xi_0$ and result from the interference of plane waves from the continuum with momenta $k_e = k_F + 1/\xi$ and $k_h = k_F - 1/\xi$. The exponential dependence of $I_1^{\delta_1=0}(l/\xi_0)$ is a direct result of the overlap of the ABS wave functions and a signature of the non-local nature of the φ-junction effect. In the case of zero separation ($l = 0$), the device only has two terminals and as expected the supercurrent is zero at $\delta_1 = \varphi = \delta_2$ since the total phase drop $\delta = \delta_1 - \delta_2$ is also zero. The φ-supercurrent $I_1^{\delta_1=0}(0)$ for the symmetric case is given by the single junction expression (Eq. 1.7) with $\tau_0 = \tau_0'$ and $\delta = -\varphi$. In addition to the rightwards shift of the current-phase relation, since $\tau_0 > \tau_0'$ the overall amplitude decreases as $l/\xi_0 \to 0$ (Fig. 1.8, top to bottom). For single junctions in the short limit, the continuum carries a negligible supercurrent [35] and one can accurately describe the Josephson effect by considering only the ABS. Here, we note that while in the extreme cases $l \ll \xi_0$ and $l \gg \xi_0$ the supercurrent is entirely carried by ABS (Fig. 1.8(a) and (e), this is not the case for intermediate separation $l \sim \xi_0$. The contribution of the continuum (states with $E > \Delta$) becomes comparable in magnitude and tends to flow in the opposite direction. Comparing Fig. 1.6 and 1.8, we observe cusps in both contributions to the supercurrent each time a discrete state escapes from the gap. The total supercurrent, however, evolves smoothly, indicating that the ABS hybridize as much with the continuum as with each other and that the distinction is somewhat artificial.

Andreev molecules can be exploited to engineer nonlocal Josephson devices. As an example, Fig. 1.9(b) shows a circuit where two superconducting loops interrupted by Josephson junctions are connected to each other by a single superconducting wire. In the absence of hybridization, assuming the superconducting loops have negligible inductances and that there is no flux in the first loop ($\Phi_1 = 0$), we expect that the applied flux Φ_2 results in a phase difference $\delta_2 = \Phi_2/\varphi_0$ and a supercurrent in the second loop. However, if the length of this wire is short such that the junction separation is small $l \lesssim \xi_0$, applying a magnetic flux Φ_2 will not only induce a current in the second loop but also give rise to a non-local current in the first loop, even though δ_1 is zero. This zero-phase supercurrent $I_1^{\delta_1=0}$ periodically depends on δ_2 (Fig. 1.9(b)) with a

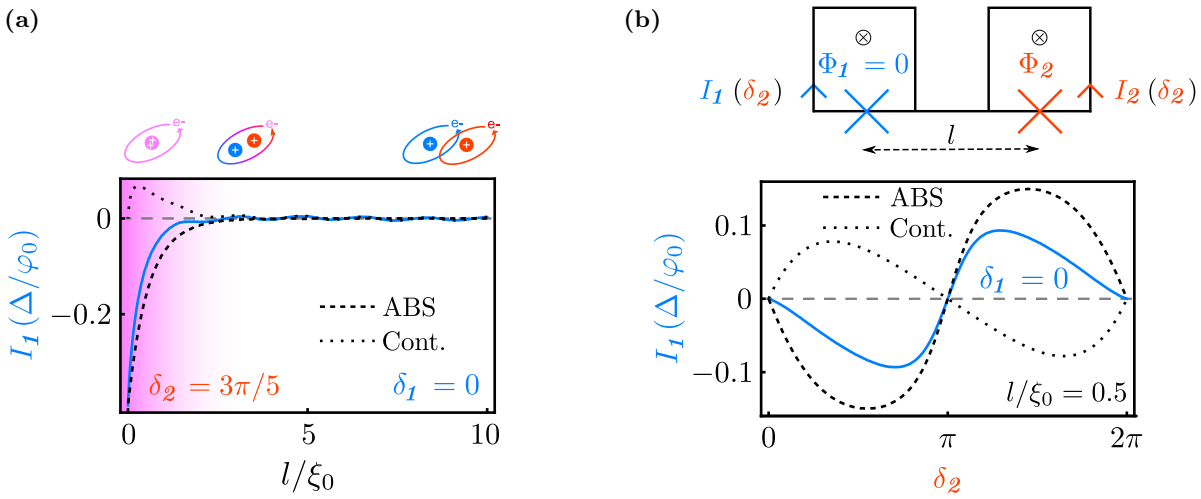

Figure 1.9: Zero-phase current and φ-junction behavior. (a) Evolution of the 0-phase current as a function of l/ξ_0 for fixed $\delta_2 = 3\pi/5$. Contributions of the continuum (dotted lines) and ABS (dashed lines) are indicated. (b) Circuit (top) to demonstrate a nonlocal Josephson effect. If hybridization between the two junctions is strong enough, the current I_1 flowing through the first junction can be modulated by the flux Φ_2 threading the second loop (bottom plot, calculated for $l/\xi_0 = 0.5$). Parameters used for these calculations: $U_1 = U_2 = 0.25\hbar v_F$ ($\tau_1 = \tau_2 \approx 0.94$), and $k_F l = \pi/2$ (mod2π) with $k_F l \gg 1$.

negative slope near the origin.

1.1.5 Particular case study: tunnel Josephson junctions

1.1.5.1 Spectrum for small transmission $\tau_0 \ll 1$

A wide variety of superconducting devices including most superconducting qubits are based on tunnel Josephson junctions. In that case, ABS are very close to the edge of the superconducting gap ($\epsilon \sim 1$) such that their wave functions extend over a large distance ($\xi_0/\xi \ll 1$). For devices made, for example, with aluminum, the distance l between the junction is typically comparable to the bare superconducting coherence length ξ_0 and the overlap of ABS wave functions $e^{-2l/\xi} \sim 1$ becomes important (Fig. 1.10). One could thus naively expect a strong hybridization of their ABS leading to spectacular nonlocal effects. However, for small transmission τ_0, nonlocal microscopic mechanisms (dEC and dCAR) are very unlikely as they require double tunneling of Cooper pairs through the barriers with a probability proportional to τ_0^2. This competes with local tunneling of Cooper pairs (EC) whose probability is proportional to $\tau_0\left(1 - e^{-2l/\xi}\right)$ where the second factor corresponds to the portion of the ABS wave functions in the central superconductor. As a consequence, local events will generally dominate unless wave functions spread over a very large distance $\xi \sim l/\tau_0$. In standard devices, the distance between tunnel junctions is a few μm and the transmissions are around $\tau_0 \sim 10^{-6}$ (for 1 μA.μm^{-1}). Wave functions would have thus to extent over more than a meter in order to fulfill this condition, which suggests that non-local effects are weak in these devices and one expects to observe

standard Josephson effect.

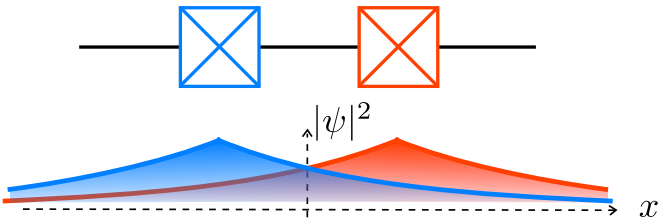

Figure 1.10: For tunnel junctions, $\xi \gg \xi_0$, which can lead to a strong overlap of the ABS wave functions ψ even for $l > \xi_0$.

However in the case of an ideal central superconductor, the tunnel barriers form a Fabry-Perot cavity, which leads to interference that drastically affects the transmission. This interference results in the formation of normal discrete electronic levels in the central part of the device that will serve as channels for local and non-local microscopic events to happen. One can distinguish "off" or "on" resonance conditions, depending on the value of $k_F l$, for which the transmission is respectively reduced or increased. In that case, the Josephson effect, including non-local processes, is modified. The tunnel limit is interesting as it provides a compact analytical expression of the Andreev spectrum giving insight in the mechanism leading to ABS hybridization. In the tunnel limit ($\tau \ll 1$) in Eq. 1.11 leads to the following ABS spectrum

$$\epsilon^{\pm\pm} \approx \pm\sqrt{1 - \tau\left(\epsilon^{\pm\pm}\right)\mathcal{F}_{\pm}\left(\delta_{1,}\delta_2\right)} \tag{1.16}$$

where energy has been normalized by the superconducting gap Δ. This expression is an approximation, which remains correct if $\sin^2\left(k_F l\right) \neq 0$ or if the junctions are not too close $l/\xi \gg \tau_0$. Here, $\tau\left(\epsilon\right)$ is an energy-dependent effective transmission and $\mathcal{F}_{\pm}$ are combinations of trigonometric functions of $\delta_{1(2)}$

$$\mathcal{F}_{\pm}\left(\delta_{1,}\delta_2\right) = \mathcal{F}_1 \mp \sqrt{\mathcal{F}_1^2 - \mathcal{F}_2}$$

with

$$\begin{cases} \mathcal{F}_1 & = s_1^2 + s_2^2 + \frac{\tau_0 \xi}{4l} s_{12}^2 \\ \mathcal{F}_2 & = 4\sin^2\left(k_F l\right) s_1^2 s_2^2 \end{cases}$$

where we have introduced compact notations

$$\begin{cases} s_1 & = \sin\left(\frac{\delta_1}{2}\right) \\ s_2 & = \sin\left(\frac{\delta_2}{2}\right) \\ s_{12} & = \sin\left(\frac{\delta_1 - \delta_2}{2}\right) \end{cases}$$

Intuitively, one can see that combinations of $s_{1(2)}$ and s_{12} will result in contributions proportional to $\sin\left(\delta_1 \mp \delta_2\right)$, emerge respectively from dEC and dCAR and others to $\sin^2 \delta_{1(2)}$ linked to local processes. The secular Eq. 1.16 reminds of the energy spectrum of ABS (see Eq. 1.6) in a single junction except that the apparent transmission $\tau\left(\epsilon\right)$ depends on ξ, and therefore on the energy, and momentum k_F. At first order in l/ξ, this transmission is given by

$$\tau\left(\epsilon\right) \approx \frac{\tau_0}{2} \frac{l/\xi}{\left(l/\xi\right)^2 + \sin^2\left(k_F l\right)} \tag{1.17}$$

This function of $k_F l$ peaks and becomes larger than the bare transmission of the junctions τ_0 when $k_F l = 0 \ (\mathrm{mod}\pi)$ but still with $\tau(\epsilon) < 1$ thanks to the condition $l/\xi \gg \tau_0$. This results in periodic Lorentzian shaped peaks of width l/ξ. This width is reminiscent of the decay $e^{-l/\xi}$ of quasiparticles propagating between the tunnel barriers in the central part of the device such that interference gradually disappears as l tends to infinity. For other values of $k_F l$, $\tau(\epsilon)$ becomes much smaller. These variations of the transmission cause ABS to respectively go deeper into the superconducting gap or closer to its edge, which makes ξ vary by orders of magnitude. At the same time, the probabilities for local and non-local processes to happen are also affected as they depend on how ABS wave functions spread over the different parts of the device. This incidentally changes the nature of the Josephson effect as we will subsequently demonstrate.

1.1.5.2 Off resonance ballistic devices

Interference as described above would only be observable if quasiparticles could propagate ballistically in the device and preserve their phases. In hypothetical devices made with ballistic superconductors, effects of ABS hybridization through dEC and dCAR can have spectacular consequences on the properties of the circuits whether they are resonant or not. Off resonance ($\sin^2(k_F l) \approx 1$, Fig. 1.11(a)), the transmission can be approximated as $\tau \approx \tau_{off}\sqrt{1-\epsilon^2}$ with $\tau_{off} = \tau_0 l/(2\xi_0)$ and becomes much smaller than the bare transmissions of the junctions since $\epsilon \approx 1$. Under this condition, Eq. 1.16 at first order in l/ξ leads to the following ABS energies

$$\epsilon_{off}^{\pm\pm} = \pm\sqrt{1-\tau_{off}^2\left[s_1^2+s_2^2 \mp \sqrt{\left(s_1^2-s_2^2\right)^2+\frac{\xi_0^2}{l^2}s_{12}^2}\right]^2}$$

This is very different from the standard ABS spectrum of a single junction (Eq. 1.6). First, energies depend on two superconducting phase differences $\delta_{1(2)}$ rather than on a single one. Moreover the amplitude of ABS oscillations with these phases is proportional to τ_0^2 rather than τ_0, which drastically suppresses the supercurrent carried by ABS. This is due to destructive interference in the Fabry-Perot resonator formed by the two barriers, and this suppression becomes even more efficient as the junctions are placed closer to each other. On top of these interference effects, the formation of an Andreev molecule, due to hybridization of ABS, materializes in the term proportional to s_{12}, due to dEC, with an amplitude that slowly tends to zero when junctions are far from each other compared to ξ_0. As shown in Fig. 1.11(b), it manifests itself in the spectrum as avoided crossings between ABS of the two junctions at $\delta_1 = -\delta_2$. Remarkably, the avoided crossing is much less pronounced at $\delta_1 = \delta_2$ and even cancels at first order in l/ξ. This result from dCAR being strongly suppressed by destructive interference in the central part of the device, while dEC involving a direct tunneling between the two parts remains important. Similarly to the case of junctions with large transmissions described before, using a fixed δ_2, this introduces large asymmetry with respect to $\delta_1 = \pi$ in the spectra. Note that here we can recover the spectrum of a single junction by taking $l \to 0$. The contribution of ABS to the Josephson energy is given by the sum of ABS of negative energies

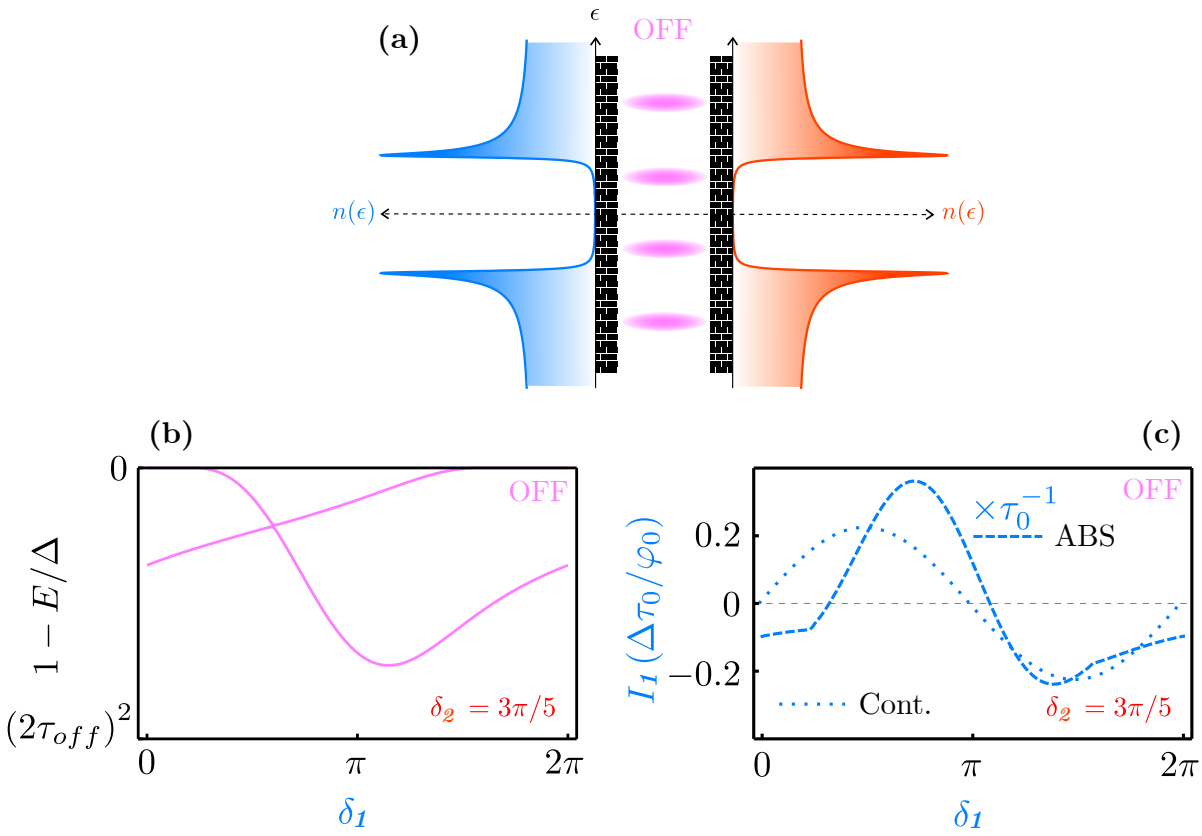

Figure 1.11: (a) When $\sin^2(k_F l) \approx 1$, the device is off resonance and the density of states in the central part of the device is small because of destructive interference. This limits the transmission of the two junctions and reduces the Josephson effect drastically. (b) The spectrum for a tunnel device off resonance shows a strong hybridization of ABS with large avoided crossings, but the discrete spectrum is close to the edge of the gap. (c) Off resonance, the supercurrent carried by the first tunnel junction has two contributions: one from the discrete spectrum (dashed line) and the other from the continuum (dotted line). The ABS contribution shows a φ-junction behavior but it is much smaller than the continuum contribution. Here we multiply the ABS contribution by a factor τ_0^{-1} for visibility.

$E_{ABS} = \Delta\left(\epsilon_{off}^{-+} + \epsilon_{off}^{--}\right)$ and, since $\tau_{off} \ll 1$, it can be approximated as

$$E_{ABS} \approx \frac{\Delta}{2}\tau_{off}^2 \left[\sum_{i=1,2}(1-\cos\delta_i)^2 + 2\frac{\xi_0^2}{l^2}s_{12}^2\right]$$

where we have discarded a constant term. This expression has the same 2π-periodicity with $\delta_{1(2)}$ than the Josephson energy of a single junction ($E_J \propto \cos\delta$) but also additional harmonics with a π-periodicity. As a consequence, the current carried by ABS deviates from the usual Josephson relation ($I_J = I_c \sin\delta$)

$$I_{1(2)}^{ABS} = I_c^{off}\left[4s_{1(2)}^2 \times \sin\delta_{1(2)} \pm \frac{\xi_0^2}{l^2}\sin\left(\delta_1 - \delta_2\right)\right] \tag{1.18}$$

The off-resonance critical current $I_c^{off} = \Delta\tau_{off}^2/2\varphi_0$ is much smaller than the bare critical current of individual Josephson junctions $I_c = \Delta\tau_0/4\varphi_0$ since $\tau_{off}^2 \ll \tau_0$ and would be therefore only detectable for moderately low transmissions, for example $\tau_0 \approx 0.1$. The second term in Eq. 1.18 is of non-local nature and is the consequence of ABS hybridization between the junctions. We see that if one junction is polarized with a finite phase, for example with $\delta_2 \neq 0$, the ABS will carry a supercurrent through the other junction if when no phase is applied across it (Fig. 1.11(d)). Maintaining $\delta_1 = 0$, ABS have thus a perfect nonlocal behavior with a 0-phase current $I_1^{ABS}(0,\delta_2) = -I_c^{off}\xi_0^2/\left(4l^2\right) \times \sin\left(\delta_2\right)$. This behavior is, however, extremely hard to detect experimentally because the continuum is carrying a much larger supercurrent than the ABS. Numerical calculations show us that the total current–phase relation is the same as the one of a single bare junction up to a factor (Fig. 1.13). In order to see the formation of Andreev molecules, we would need to be able to measure selectively the current carried by ABS and the continuum.

1.1.5.3 On resonance ballistic devices

The behavior of the device is completely different in the resonant case (Fig. 1.12(a)). If $\sin^2(k_F l) \approx 0$, the transmission then peaks at $\tau \approx \tau_{on}\sqrt{1-\epsilon^2}^{-1}$ with $\tau_{on} = \tau_0\xi_0/(2l)$. In this configuration, two ABS merge with the continuum at $\epsilon = 1$ leaving a spectrum of a single ABS pair

$$\epsilon_{on}^{\pm} = \pm\sqrt{1 - \left[2\tau_{on}\left(s_1^2 + s_2^2\right)\right]^{2/3}}$$

The exponent 2/3 of the second term under the square root is due to the joined effects of dEC and dCAR, which are enhanced by the fact that a resonant level lies at the Fermi energy level of the electrodes. This can be understood by looking at the evolution of the ABS spectrum under resonant condition when the two junctions are gradually brought together from infinity, which makes nonlocal processes more and more effective. This causes the formation of larger and larger avoided crossings between ABS of the two junctions. Once the limit $l/\xi \ll 1$ has been reached, one pair of ABS vanishes into the continuum while the other one lies within the superconducting gap and always remains detached from the edge provided that one of the phases $\delta_{1(2)}$ is finite (Fig. 1.12(b)). The remaining pair is fully delocalized over the two junctions. Moreover, due to constructive interference, the amplitude of ABS oscillations is proportional to $\tau_0^{2/3}$, which can

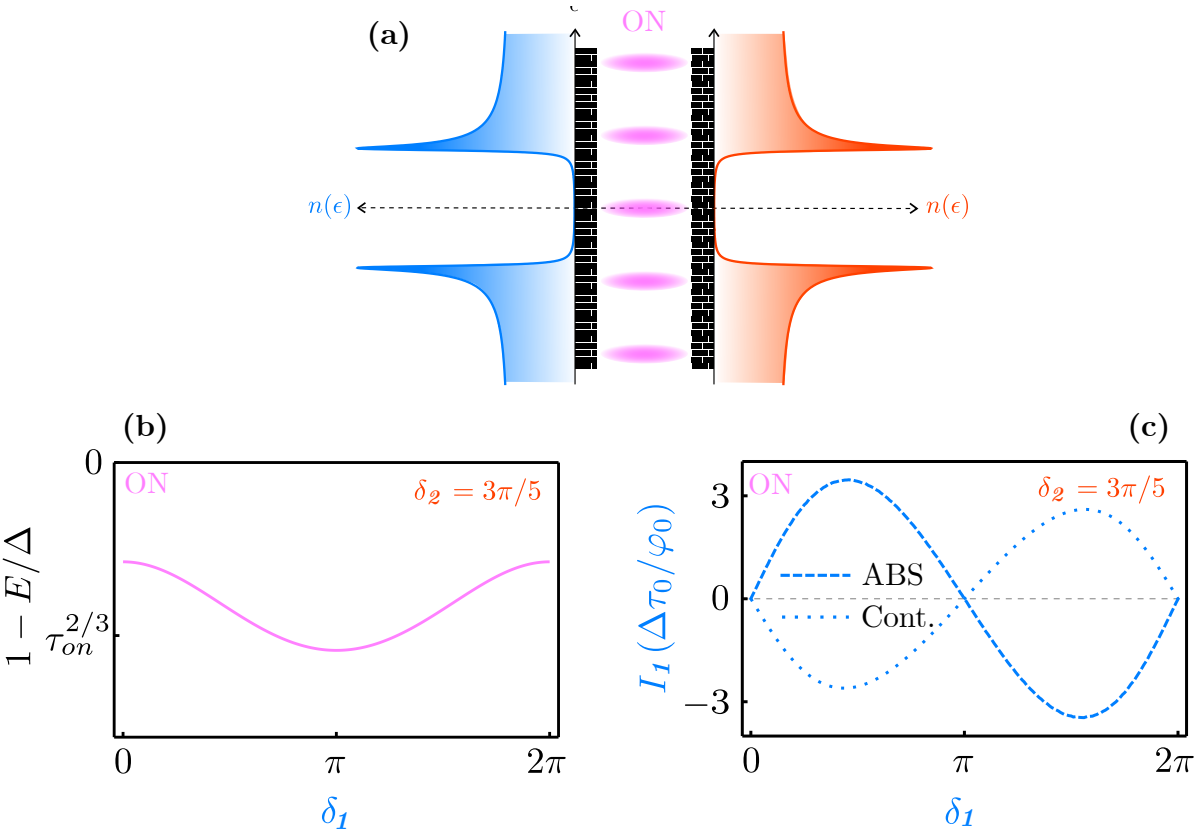

Figure 1.12: (a) On resonance, $\sin^2(k_F l) = 0$, the density of states in the central part of the device is expected to be large, which favors the flow of supercurrent. (b) The spectrum then shows only one pair of ABS, which are detached from the edge of the gap. ABS go deeper in the gap than in a single junction. (c) The contribution of ABS and continuum to the supercurrent are of the same order of magnitude but in opposite direction. Parameters used for these calculations: $\delta_2 = 3\pi/5$, $l/\xi_0 = 1$, $U_1 = U_2 = 100\,\hbar v_F$ ($\tau_1 = \tau_2 \approx 10^{-4}$), and $k_F l \gg 1$.

be orders of magnitude larger than for isolated tunnel junctions. Note that, in this expression, we cannot take the limit $l \to 0$ to merge the two junctions and recover the spectrum of a single one because the conditions of validity ($\sin^2(k_F l) \neq 0$ or $l/\xi \gg \tau_0$) would not be respected. In that case, we would obtain transmission $\tau(\epsilon) \sim \tau_0 \xi/l$ larger than 1, which is non-physical. Similarly, to the off-resonance case, one can deduce the contribution of ABS to the Josephson energy

$$E_{ABS} \approx -\frac{\Delta}{2}\tau_{on}^{2/3}\left(2-\cos\delta_1+\cos\delta_2\right)^{2/3}$$

as well as the current carried by ABS

$$I_{1(2)}^{ABS} = I_c^{on}\sin\delta_{1(2)}\left(2-\cos\delta_1-\cos\delta_2\right)^{-1/3} \tag{1.19}$$

with the critical current $I_c^{on} = \Delta\tau_{on}^{2/3}/(3\varphi_0)$. Similarly to the off-resonance case, the contribution of the continuum is important and the total current–phase relation is the same as the one of a single bare junction (Fig. 1.12(c) and 1.13). In practice, ballistic superconductors are extremely rare in superconducting circuits, but semiconducting nanowires covered with epitaxial aluminum or Van der Waals materials such as $NbSe_2$ are potential candidates for the observation of an Andreev molecule in ballistic tunnel devices. Non-local effects are, however, much weaker than in devices of larger transmission and it would be a challenge to detect them. For example, the $\varphi-$junction behavior seems almost suppressed (Fig. 1.13).

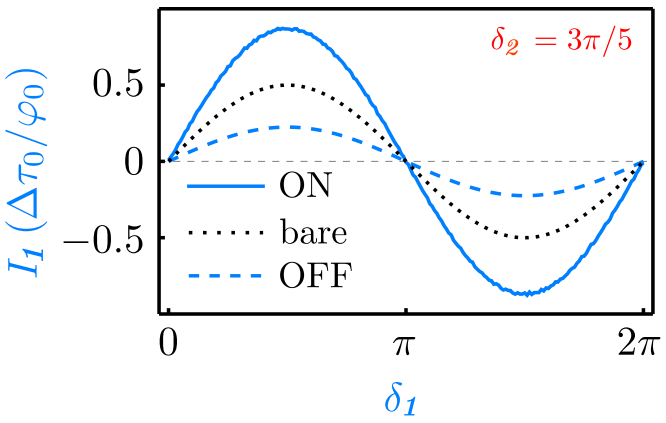

Figure 1.13: Taking into account both contributions, the current-phase relation of the first tunnel junction is $I_1 \approx I_c \sin\delta_1$ with no φ-junction behavior. The critical current is larger (on resonance, solid line) or smaller (off resonance, dashed line) compared to a single tunnel junction with $\tau_0 \approx 10^{-4}$ (dotted line).

1.1.5.4 Diffusive devices

In most experiments involving tunnel Josephson junctions, superconductors are diffusive. Each electronic channel carries a supercurrent through diffusive paths over which electrons take random phases $k_F l$ where l can vary by several Fermi wavelengths. As a consequence, the interference effects that we described previously are suppressed and non-local effects are essentially negligible. The total Josephson energy of the system is obtained by averaging the phase

over all channels

$$E_J \approx \frac{\Delta}{\pi}\int_{-\pi/2}^{\pi/2}(\epsilon^{-+}+\epsilon^{--})dk_F l$$

Where $\epsilon^{-\pm}$ are the energies of ABS of negative energies in Eq. 1.16 and the integral is summing over all the possible values of $k_F l$ within one period of $\tau(\epsilon)$. This can either be done numerically or by approximating $\tau(\epsilon)$ as a Dirac delta distribution $\tau_0\pi\delta(k_F l)/2$ leading at first order in$\tau_0$to

$$E_J \approx \frac{\tau_0\Delta}{2}(\cos\delta_1+\cos\delta_2)$$

where we have dismissed a constant term. This simply corresponds to the Josephson energy of two independent tunnel Josephson junctions. The next-order correction in τ_0 is given by

$$\delta E_J \approx \frac{\tau_0^{5/3}\xi_0^{2/3}}{8l^{2/3}}\frac{s_{12}^2}{\left(s_1^2+s_2^2\right)^{1/3}}$$

which is completely negligible since $\tau_0^{5/3} \ll \tau_0$. In fact, even taking into account the contribution of the continuum, the current-phase relations correspond to the standard Josephson formula $I_{1(2)} \approx I_c \sin\delta_{1(2)}$ where I_c is the bare critical current of the junctions. The effects of ABS hybridization are therefore hardly measurable in conventional devices with superconducting tunnel junctions. Although the common technologies used to build Josephson junction, like epitaxial superconductor/semiconductor nanowires or 2D electron gas, lead to devices with high transmission but more importantly with more than one channel. This structure changes the landscape seen by one ABS as now it has more ABS to interact and potentially hybridize with. To study this more complex devices, one could apply the same BdG approach we used in this section, however, even if this formalism is useful to develop an intuitive understanding of the phenomenon, it is unwieldy for complicated structures like those. A more tailored formalism to investigate multi-channel devices is the Landauer-Büttiker scattering formalism which will be used in the next section

1.2 Multi-channel Andreev molecule in 1D

In a Josephson junction with multiple conduction channels, each channel hosts independent ABS. The total supercurrent is given by the sum of all of their contributions (Eq. 1.7) and the Josephson effect is qualitatively the same as for a single channel. However, when two multi-channel junctions are placed close to each other, each ABS at the first junction can potentially couple to every ABS at the sedonc junction to form complex Andreev molecules. This is equivalent to increasing the number of valence electrons leading to Andreev molecules of larger atomic number. Experimentally, the multi-channel case is relevant since many quantum conductors used in weak links have lateral dimensions larger than the Fermi wavelength and thus host a large number of channels. A convenient approach to deal with conduction through mesoscopic systems is the Landauer-Büttiker scattering formalism [45]. As in the last section, we will first describe briefly the simple case of a single Josephson junction and then consider the Andreev molecule.

1.2.1 Andreev Bound States in a multi-channel Josephson junction

The Landauer-Büttiker formalism permits to describe coherent conductors in terms of independent channels. In this approach, electrons and holes (e and h) are described by an ensemble of waves propagating backwards ($\leftarrow$) or forwards ($\rightarrow$), which are connected to each other by normal scattering processes at the weak link or Andreev processes on the two superconductors. These waves can be labeled with two sets of four coefficients

$$\begin{cases} \mathcal{A} = & (a_e^{\rightarrow}, a_e^{\leftarrow}, a_h^{\rightarrow}, a_h^{\leftarrow})^T \\ \mathcal{B} = & (b_e^{\leftarrow}, b_e^{\rightarrow}, b_h^{\leftarrow}, b_h^{\rightarrow})^T \end{cases} \tag{1.20}$$

where $\mathcal{A}$ describes waves propagating towards weak links with amplitudes a and $\mathcal{B}$ describes outgoing waves with amplitudes b. The scattering equation for the weak links is given by:

$$\mathcal{B} = S_N \mathcal{A} \tag{1.21}$$

with

$$S_N = \begin{pmatrix} S_e & 0 \\ 0 & S_h \end{pmatrix}$$

where $S_{e(h)}$ is the normal state scattering matrix describing scattering of electrons and holes in the weak link. The matrices S_e and S_h can be linked by: $S_e = S_h^* S_e = S_h^*$. The specific form of S_e and S_h will depend on the weak links. For example, the scattering matrix corresponding to a Dirac δ-potential as used in the BdG analysis of the Andreev molecule [26] is given by

$$S = \begin{pmatrix} \frac{-iu}{1+iu} & \frac{1}{1+iu} \\ \frac{1}{1+iu} & \frac{-iu}{1+iu} \end{pmatrix} \tag{1.22}$$

where the constant u is related to the strength of the δ-potential, U_0, and the Fermi velocity, v_F, by $u = U_0/\hbar v_F$. For simplicity, in the following analysis for a multi-channel weak link we use random symmetric unitary matrices for S. Other classes of scattering matrices corresponding to breaking time-reversal symmetry or spin-rotation symmetry can be used to model the effect of a magnetic field or spin-orbit interaction [46, 47, 48]. The dimensions of S_N is therefore $4N \times 4N$ where N is the number of channels.

It remains to determine scattering on the superconductors. In contrast to scattering at the normal weak links, which need not preserve momentum, scattering on the superconductors occurs through Andreev processes which are momentum-conserving when the Fermi energy is much larger than the superconducting gap. For the semi-infinite outermost superconducting electrodes, for energies smaller than the superconducting gap ($|E| < \Delta$), the only scattering process possible is Andreev reflection, in which an incident electron is retroreflected as a hole and an incident hole is retroreflected as an electron. This Andreev reflection amplitude is $r_A = e^{-i(\alpha \pm \phi_{1,2})}$, where $\phi_{1,2}$ is the superconducting phase of the first (second) superconductor and $\alpha = \cos^{-1}\epsilon$ with $\epsilon = E/\Delta$[49]. Since the Andreev reflection probability, $|r_A|^2$, is unity the semi-infinite electrodes act as perfect phase-conjugating mirrors for electrons and holes [50]. The phase shift acquired in reflection is the sum of α, which is energy dependent, and the

superconducting phases $\phi_{1,2}$. We can depict the Andreev scattering matrix as a process for which b states become incident and a are emergent :

$$\mathcal{A} = S_A \mathcal{B} \tag{1.23}$$

where S_A is a block matrix:

$$S_A = \begin{pmatrix} 0 & 0 & e^{-i\phi_1} & 0 \\ 0 & 0 & 0 & e^{-i\phi_2} \\ e^{i\phi_1} & 0 & 0 & 0 \\ 0 & e^{i\phi_2} & 0 & 0 \end{pmatrix} \otimes \mathbb{I}_N,$$

With $\mathbb{I}_N$ a $N \times N$ matrix where N corresponds to the number of channels.

In order to find resonant bound states, one needs to cascade the scattering matrices S_N and S_A to define a closed loop for the states. A stationary state can be defined inside the weak link by mixing Eq. 1.21 and Eq. 1.23 giving

$$\mathcal{A} = S_A S_N \mathcal{A},$$

This condition implies that the roots of the following equation,

$$\mathrm{Det}\left(\mathbb{I}_{4N} - S_A S_N\right) = 0, \tag{1.24}$$

are the energies of the resonant states. These states are ABS, as they correspond to coherent resonant states between two superconductors separated by a weak link and mediated by Andreev reflections. We recover the same formula as the previous section for the energies and the current

$$E_A = \pm\Delta\sqrt{1 - \tau_0 \sin^2\left(\frac{\delta}{2}\right)}, \tag{1.25}$$

$$I^{ABS} = -\frac{1}{\varphi_0}\frac{\partial E_{ABS}}{\partial \delta} = \frac{\Delta}{4\varphi_0}\frac{\tau_0 \sin(\delta)}{\sqrt{1 - \tau_0 \sin^2\left(\frac{\delta}{2}\right)}}$$

With $\varphi_0 = \hbar/2e$, $\tau_0 = 1/\left|1 + iU_0/\hbar v_F\right|^2$ and $\delta = \phi_1 - \phi_2$.

As expected, the two methods give the same results. From Eq. 1.25 we can plot the energy spectra for a single Josephson junction made of 20 random channels. The channels are independent and each of the 40 ABS as shown in Fig. 1.14.

However it is interesting to highlight the difference in the construction process of the ABS. In the BdG approach, we had to explicitly constrain the wave function and its derivative to be continuous. While with the Landauer-Büttiker approach, this constraint is embedded in the scattering matrix and one just has to give wave functions.

In the following section, we will connect another multi-channel Josephson junction to the first one which is a good toy model of an Andreev molecule built from nanowires.

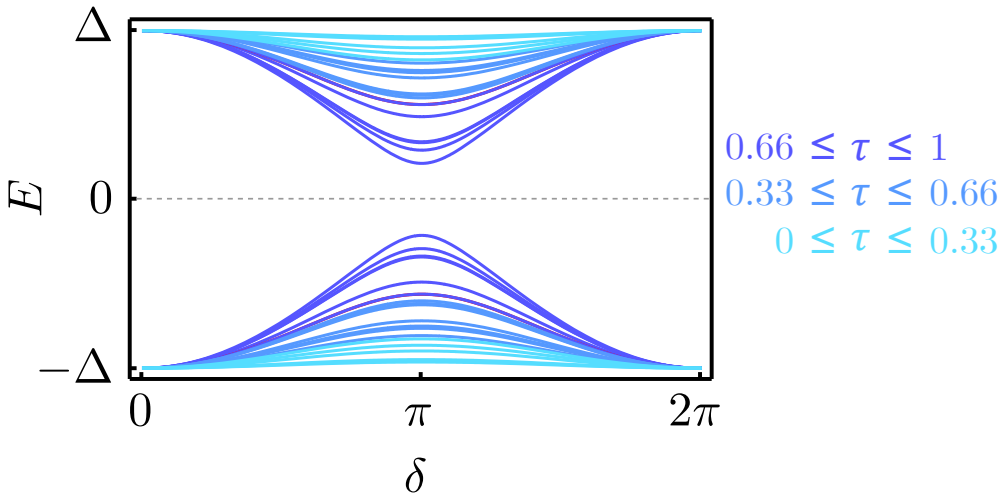

Figure 1.14: Energy spectrum of a single multi-channel junction composed of 20 independent channels. This spectrum represents the 40 ABS carried by each channel for which the transmission was randomly assigned.

1.2.2 Scattering description of Andreev molecule

Similarly to Sec. 1.1.2, we connect a second junction to the first junction we described in the previous section. This new junction shares, as previously, a terminal with the first junction. The common terminal, of size l, is also connected to the ground and allows defining independent phase across each junction. In this configuration, using the Landauer-Büttiker formalism, matrices describe the scattering of propagating electrons or holes on three different types of elements: weak links, semi-infinite superconductors, and a superconductor of finite length, Fig. 1.15(a). In this approach, electrons and holes (e and h) are described by an ensemble of waves propagating forwards ($\rightarrow$) or backwards $\leftarrow$), which are connected to each other by normal scattering processes at the two weak links or Andreev processes on the three superconductors. These waves can be labeled with two sets of eight coefficients

$$\begin{cases} \mathcal{A} = & (a^{\rightarrow}_{1e}, a^{\leftarrow}_{1e}, a^{\rightarrow}_{2e}, a^{\leftarrow}_{2e}, a^{\rightarrow}_{1h}, a^{\leftarrow}_{1h}, a^{\rightarrow}_{2h}, a^{\leftarrow}_{2h})^T \\ \mathcal{B} = & (b^{\leftarrow}_{1e}, b^{\rightarrow}_{1e}, b^{\leftarrow}_{2e}, b^{\rightarrow}_{2e}, b^{\leftarrow}_{1h}, b^{\rightarrow}_{1h}, b^{\leftarrow}_{2h}, b^{\rightarrow}_{2h})^T \end{cases} \tag{1.26}$$

where $\mathcal{A}$ describes waves propagating towards weak links with amplitudes a and $\mathcal{B}$ describes outgoing waves with amplitudes b. The scattering equation for the weak links is given by:

$$\mathcal{B} = S_N \mathcal{A} \tag{1.27}$$

with

$$S_N = \begin{pmatrix} S_1 & 0 & 0 & 0 \\ 0 & S_2 & 0 & 0 \\ 0 & 0 & S_1^* & 0 \\ 0 & 0 & 0 & S_2^* \end{pmatrix}$$

where $S_{1(2)}$ is the normal state scattering matrix describing scattering of electrons in the first (resp. second) weak link. The equivalent for holes is given by $S^*_{1(2)}$. The specific form of

$S_{1,2}$ and $S_{1,2}^*$ will depend on the weak links. For example, the scattering matrix corresponding to a Dirac δ-potential as used in the BdG analysis of the Andreev molecule [26] is given by Eq 1.22. For simplicity, in the following analysis for a multi-channel weak link we used random symmetric unitary matrices for S_1 and S_2. Other classes of scattering matrices corresponding to breaking time-reversal symmetry or spin-rotation symmetry can be used to model the effect of a magnetic field or spin-orbit interaction [46, 47, 48]. The dimensions of S_N are therefore $8N \times 8N$ where N is the number of channels.

It remains to determine scattering on the superconductors. In contrast to scattering at the normal weak links, which need not preserve momentum, scattering on the superconductors occurs through Andreev processes which are momentum-conserving when the Fermi energy is much larger than the superconducting gap. For the semi-infinite outermost superconducting electrodes, for energies smaller than the superconducting gap ($|E| < \Delta$), the only scattering process possible is Andreev reflection. In that configuration an incident electron is retroreflected as a hole and an incident hole is retroreflected as an electron. This Andreev reflection amplitude is $r_A = e^{-i(\alpha \pm \varphi_{1,2})}$, where $\varphi_{1,2}$ is the superconducting phase of the first (resp. second) superconductor and $\alpha = \cos^{-1}\epsilon$ with $\epsilon = E/\Delta$[49]. Since the Andreev reflection probability, $|r_A|^2$, is unity the semi-infinite electrodes act as perfect phase-conjugating mirrors for electrons and holes [50]. The phase shift acquired in reflection is the sum of α, which is energy dependent, and the superconducting phases $\varphi_{1,2}$.

As shown in Fig. 1.15(b), the situation is different for a superconductor of finite length, in which an electron or hole can also propagate across the superconducting slab and emerge on the other side without being retroreflected. For example, in Fig. 1.15(b) an electron incident on the central superconductor from the first side with amplitude $b_{1e}^{\rightarrow}$ and momentum $+k_F$ may either be retroreflected as a backward-propagating hole of amplitude $a_{1h}^{\leftarrow}$ or transmitted as a forward-propagating electron of amplitude $a_{2e}^{\rightarrow}$, both particles having momentum $+k_F$. When there is normal scattering in addition to a finite superconductor, such as in Fig. 1.15(c) where the weak link has transmission probability $\tau < 1$, electrons and holes can also be backscattered (BS) and crossed-Andreev reflected (CAR), which consists of tunneling through the superconductor and conversion from electron to hole or vice versa [51]. As depicted, the CAR process for an electron incident from the first side corresponds to an Andreev reflection followed by backscattering of the retroreflected hole, which then traverses the finite superconductor and exits towards the second side. This mechanism can also be seen as the formation, in the central slab, of a Cooper pair comprised of electrons from both outermost electrodes. The time-reversed equivalent is known as Cooper-pair splitting and has device applications [52, 53, 54]. The CAR process, which does not conserve momentum, requires backscattering in the normal weak links. The probability amplitude associated with the process of partial Andreev reflection, Fig. 1.15(d), can be found using the continuity of wave functions at each interface. These wave functions are built from the electron and hole eigenstates of an infinite superconductor ($\eta = e$ or h),

$$\psi_{\eta\pm}^{\varphi}(x) = \left(u_{\eta}^{\varphi}, v_{\eta}^{\varphi}\right)^T e^{\pm i k_\eta x}, \tag{1.28}$$

where L is the total size of the system and the coherence factors $u_\eta^\delta, v_\eta^\delta$ are defined similarly as in Eq. 1.3 and k_η are complex to account for bound states. Similarly as in Section 1.1.1, if the superconducting gap is much smaller than the Fermi energy, $\Delta \ll E_F$, we use the Andreev approximation. If we focus on the subspace of waves with positive momentum, the

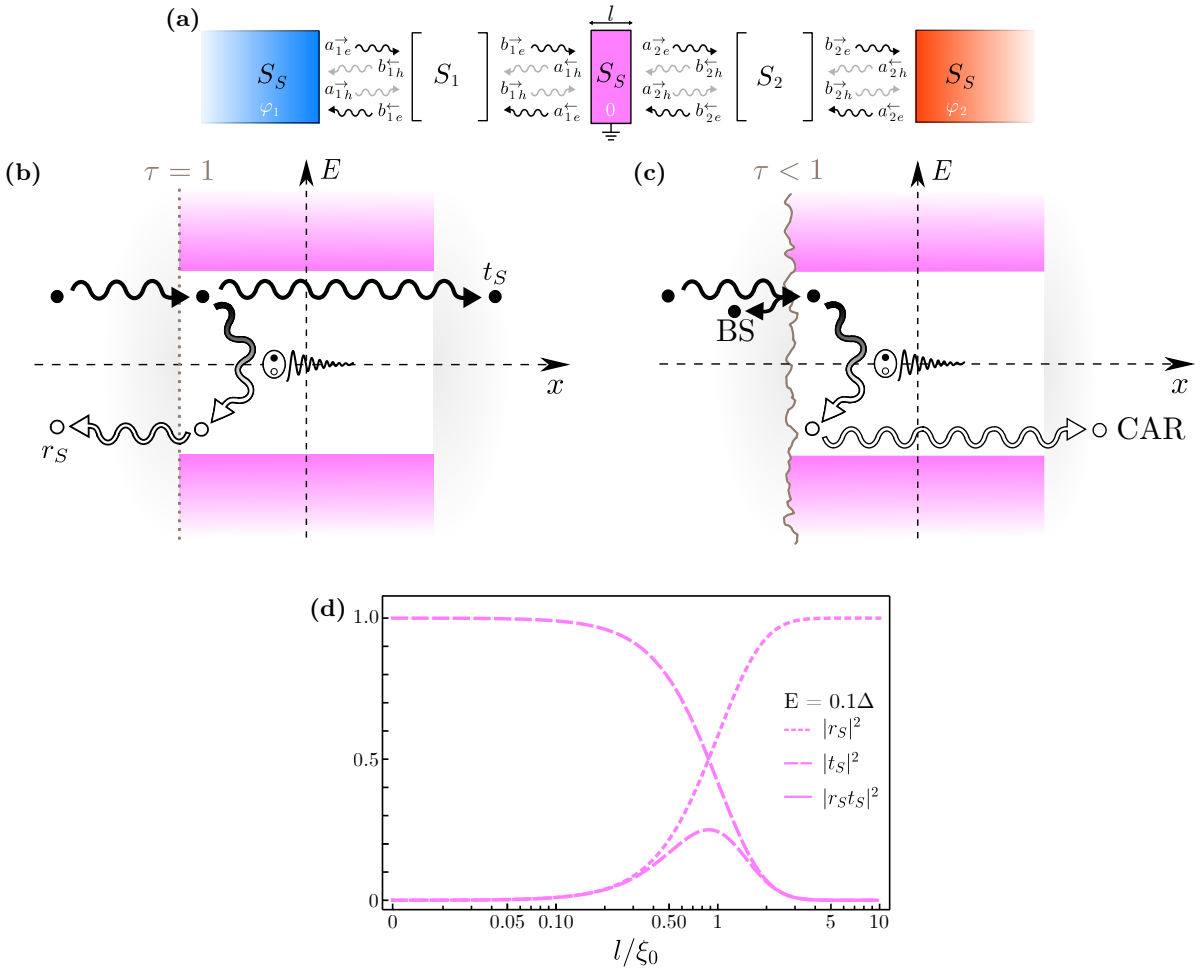
(a)
S_S
φ_1
S_1
S_S
0
l
S_2
S_S
φ_2
(b)
$\tau = 1$
E
t_S
x
r_S
(c)
$\tau < 1$
E
BS
x
CAR
(d)
1.0
0.5
0
0
0.05
0.10
0.50
1
5
10
l/ξ_0
E = 0.1Δ
$|r_S|^2$
$|t_S|^2$
$|r_S t_S|^2$

Figure 1.15: *(previous page)* Scattering description of multi-channel Andreev molecules. (a) Plane waves corresponding to electrons (black arrows) and holes (gray arrows) scatter on superconductors (blue, red and magenta) and weak links. The first (resp. second) superconductor has phase $\varphi_{1,2}$ and the central superconductor of length l is grounded with phase zero. The ground connection allows applying the phase differences $\varphi_{1,2}$ independently. The matrix S_S describes Andreev scattering processes on the superconductors while $S_{1,2}$ describes normal scattering at the weak links. Only one channel is sketched. (b) For $l \lesssim \xi_0$, an electron incident on the central superconductor with energy E less than the superconducting gap Δ can transmit across (elastic co-tunneling, EC) with probability amplitude t_S or be Andreev reflected as a hole with amplitude r_S. (c) In the presence of scattering, such that the first weak link has a channel transmission probablity $\tau < 1$, the electron may also be backscattered (BS) or undergo crossed Andreev reflection (CAR), which converts it into an outgoing hole. (d) The probabilities of Andreev reflection, transmission, and their product, which factors into the probability for CAR, is plotted as a function of l/ξ_0 for fixed energy $E = 0.1\Delta$. In a long superconductor, $l \gg \xi_0$, only Andreev reflection occurs whereas for a short one, $l \ll \xi_0$, only elastic co-tunneling occurs. At intermediate values $l \approx \xi_0$ and in the presence of scattering there is a peak in the CAR probability which goes to zero elsewhere.

wave function on the first side of the superconducting slab ($x < -l/2$) is given by

$$b_{1e}^{\rightarrow} e^{ik_F\left(x+\frac{l}{2}\right)} \begin{pmatrix} 1 \\ 0 \end{pmatrix} + a_{1h}^{\leftarrow} e^{ik_F\left(x+\frac{l}{2}\right)} \begin{pmatrix} 0 \\ 1 \end{pmatrix}$$

while in the center ($x < |l/2|$) it is

$$\gamma_{ce}^{+} \begin{pmatrix} u_e^0 \\ v_e^0 \end{pmatrix} e^{ik_e x} + \gamma_{ch}^{+} \begin{pmatrix} u_h^0 \\ v_h^0 \end{pmatrix} e^{ik_h x}$$

and on the second side where ($x > l/2$)

$$a_{2e}^{\rightarrow} e^{ik_F\left(x-\frac{l}{2}\right)} \begin{pmatrix} 1 \\ 0 \end{pmatrix} + b_{2h}^{\leftarrow} e^{ik_F\left(x-\frac{l}{2}\right)} \begin{pmatrix} 0 \\ 1 \end{pmatrix}$$

The superconducting phase on the central superconductor is fixed at zero and serves as the reference for the phase differences $\varphi_{1,2}$ on the outermost superconductors. Because of the ground connection, there are effectively two loops connecting the outermost superconductors to the central one, which allow tuning $\varphi_{1,2}$ independently with external magnetic fields. In addition, this ground connection allows an additional path for current flow such that the supercurrents through the two weak links may be different. In the weak links ($x < -l/2$ or $x > l/2$) only electron or hole plane waves are possible, with wave vectors $\pm k_F$ and coherence factors either $(1, 0)$ (electrons) or $(0, 1)$ (holes). In the superconducting slab, the wave functions mix electrons and holes and as a result of the complex wave vectors $k_{e,h}$ have an exponential, energy-dependent

envelope. Imposing boundary conditions at the slab edges $x = \pm l/2$ to preserve continuity we have

$$\begin{pmatrix} b_{1e}^{\rightarrow} \\ a_{1h}^{\leftarrow} \end{pmatrix} = e^{-\frac{ik_F l}{2}} \begin{pmatrix} u_e^0 e^{1/2\xi} & u_h^0 e^{-l/2\xi} \\ v_e^0 e^{1/2\xi} & v_h^0 e^{-l/2\xi} \end{pmatrix} \begin{pmatrix} \gamma_{ce}^{+} \\ \gamma_{ch}^{+} \end{pmatrix},$$
$$\begin{pmatrix} a_{2e}^{\rightarrow} \\ b_{2h}^{\leftarrow} \end{pmatrix} = e^{+\frac{ik_F l}{2}} \begin{pmatrix} u_e^0 e^{-l/2\xi} & u_h^0 e^{1/2\xi} \\ v_e^0 e^{-l/2\xi} & v_h^0 e^{1/2\xi} \end{pmatrix} \begin{pmatrix} \gamma_{ce}^{+} \\ \gamma_{ch}^{+} \end{pmatrix}.$$

By eliminating the coefficients, $c_{e,h}^{+}$ we can relate incoming and outgoing waves with a scattering matrix,

$$\begin{pmatrix} a_{1h}^{\leftarrow} \\ a_{2e}^{\rightarrow} \end{pmatrix} = \begin{pmatrix} r_S & t_S^{-} \\ t_S^{+} & r_S \end{pmatrix} \begin{pmatrix} b_{1e}^{\rightarrow} \\ b_{2h}^{\leftarrow} \end{pmatrix},$$

where we define the Andreev transmission amplitude,

$$t_S = \frac{e^{-l/\xi}\left(1 - e^{-2i\alpha}\right)}{1 - e^{-2l/\xi} e^{-2i\alpha}}, \tag{1.29}$$

with $t_S^{\pm} = t_S e^{\pm i k_F l}$, and the partial Andreev reflection amplitude,

$$r_S = \frac{e^{-i\alpha}\left(1 - e^{-2l/\xi}\right)}{1 - e^{-2l/\xi} e^{-2i\alpha}}. \tag{1.30}$$

For the negative momentum wave function, the substitution $k_F \rightarrow -k_F$ yields the same scattering matrix with t_S^{+} and t_S^{-} swapped. This amplitude satisfies $|r_S|^2 + |t_S^{\pm}|^2 = 1$ as expected from quasiparticle conservation. In a realistic system with a three-dimensional central superconductor, the wave functions ψ (Eq. 1.28) will be spherical and the geometric factors $e^{-l/\xi}$ describing the envelope of the probability amplitudes t_S, r_S (Eqs. 1.29 and 1.30) will be different. In general, they will decay faster and acquire additional dependence on the Fermi wavelength or the mean free path [55, 56, 57]. This reduction can be understood from the increase in scattering angle as the number of dimensions is increased.

The following analysis is limited to the one-dimensional case. In addition we ignore fast phase oscillations in t_S and r_S arise from the small Fermi wavelength by fixing $k_F l$ arbitrarily and independent of l while maintaining $k_F l \gg 1$. In Fig. 1.15(d) we plot the Andreev reflection probability $|r_S|^2$ and transmission probability $|t_S|^2$ for fixed energy $\epsilon = 0.1$ as a function of l/ξ_0. The likelihood of elastic co-tunneling (EC), Fig. 1.15(b), in the absence of scattering at the weak links ($\tau = 1$) is quantified by $|t_S|^2$. As the superconductor thickness goes to zero, $l/\xi_0 \rightarrow 0$, Andreev reflections are suppressed and all quasiparticles tunnel across, $t_S \rightarrow 1$. Andreev processes are equally probable when $l/\xi_0 \approx 1$. As we extend the length of the central superconductor, $l/\xi_0 \rightarrow \infty$, one recovers the Andreev reflection amplitude of a semi-infinite superconductor, $r_S \rightarrow r_A = e^{-i\alpha}$, and transmission is squashed, $t_S \rightarrow 0$. The Andreev phase-conjugating mirror is only perfect if it is much thicker than ξ_0, the characteristic length scale for Andreev reflection. Scattering at the weak links will also reduce elastic co-tunneling. If the single-channel transmissions of the weak links are $\tau_{1,2}$, the first order EC probability will be reduced to $\tau_1\tau_2|t_S|^2$. For $\tau < 1$, there will be higher order processes involving multiple reflections at the barriers which will also transmit a particle across the superconductor. Also plotted in Fig.1.15(d) is the probability $|r_S t_S|^2$, which is the Andreev scattering contribution

to the first-order CAR process depicted in Fig.1.15(c). If the first interface has transmission probability $\tau < 1$, this CAR process requires normal barrier transmission (τ), an Andreev reflection ($|r_S|^2$), a normal reflection ($1-\tau$), and an Andreev transmission ($|t_S|^2$). The Andreev contribution, $|t_S r_S|^2$, is maximal at 0.25 for a separation l/ξ_0 such that $|t_S| = |r_S| = 0.5$ and the maximum of the normal part, $\tau(1-\tau)$, is also 0.25 for $\tau = 0.5$. Therefore the maximum likelihood of the first-order CAR process is 6.25%, with higher order processes contributing little as they scale as $\tau^n(1-\tau)^n$. Ignoring higher order processes the likelihood of EC in the presence of scattering at the first weak link, $\tau|t_S|^2$, is approximately four times that of CAR for $\tau = 0.5$ and at a comparable separation $l/\xi_0 \lesssim 1$ such that $|t_S|^2 \approx 0.5$. The optimal separation l/ξ_0 to maximize CAR and EC depends on the energy ϵ but the relative likelihood for CAR over EC remains $(1-\tau)/2$. In a symmetric situation where both weak links have transmission τ, the first-order expressions above are reduced by a factor τ.

In a similar fashion to the derivation of S_N, we use these results for scattering from the three superconductors to define a matrix S_S which relates waves incident on the slab ($\mathcal{B}$) to the outgoing waves, $\mathcal{A} = S_S\mathcal{B}$,

$$S_S = \begin{pmatrix} S_{ee} & S_{eh}e^{-i\Phi} \\ S_{eh}e^{i\Phi} & S_{hh} \end{pmatrix} \otimes \mathbb{I}_N,$$

with blocks S_{eh} on the anti-diagonal for Andreev reflections,

$$S_{eh} = \begin{pmatrix} r_A & 0 & 0 & 0 \\ 0 & r_S & 0 & 0 \\ 0 & 0 & r_S & 0 \\ 0 & 0 & 0 & r_A \end{pmatrix},$$

and blocks S_{ee} and S_{hh} on the diagonal for tunneling through the central superconducting slab,

$$S_{ee} = \begin{pmatrix} 0 & 0 & 0 & 0 \\ 0 & 0 & t_S^+ & 0 \\ 0 & t_S^+ & 0 & 0 \\ 0 & 0 & 0 & 0 \end{pmatrix}.$$

S_{hh} is obtained from S_{ee} with the transformation $t_S^+ \to t_S^-$. The superconducting phases are contained in the diagonal matrix $\Phi = \mathrm{diag}\,(\varphi_1, 0, 0, \varphi_2)$ and $\mathbb{I}_N$ is the $N \times N$ identity matrix. The total size of S_S, like S_N, is $8N \times 8N$, accounting for N conduction channels. We combine the scattering equation for weak links, $\mathcal{B} = S_N\mathcal{A}$, and for superconductors, $\mathcal{A} = S_S\mathcal{B}$, in order to obtain the master equation,

$$\mathcal{B} = S_N S_S \mathcal{B}. \tag{1.31}$$

The scattering product $S_N S_S$ depends on energy ϵ, the scattering properties of the weak links ($S_{1,2}$), and the superconducting phases $\varphi_{1,2}$. Eq. 1.31 is a unity eigenvalue problem in which solutions of the characteristic equation,

$$\mathrm{Det}\,(\mathbb{I}_{8N} - S_N S_S) = 0, \tag{1.32}$$

gives the energy spectrum ϵ, the scattering amplitudes a and b, and the corresponding wave functions of the Andreev molecule [48]. To verify correctness, we numerically solved Eq. 1.32 for the spectra in the case of a single-channel Andreev molecule with symmetric δ-function barriers, i.e. S_1 and S_2 given by Eq. 1.22, and compared it for agreement with the Bogoliubov-de-Gennes solution for the same parameters [26].

1.2.3 Spectra of multi-channel Andreev molecules

In Fig. 1.16 we represent an example of a multi-channel double weak link device formed from a highly doped graphene nanoribbon [58, 59]. We show the evolution in the energy spectra of such a multi-channel Andreev molecule as the size of the central superconductor is reduced. Spectra are obtained by numerically solving the characteristic equation 1.32 for fixed 20-channel random scattering matrices $S_{1,2}$ and fixed phase $\varphi_2 = 3\pi/5$. Each channel of each weak link will have an effective transmission τ which can be extracted from the scattering matrices $S_{1,2}$. The spectra are plotted as a function of the phase φ_1 for four values of the separation l/ξ_0. Each conduction channel of each junction hosts one pair of ABS and as a consequence there are $4N = 80$ lines, some of which are close to the gap edge and difficult to distinguish. For large separation, $l/\xi_0 \gg 1$, there is no coupling between the two weak links, and the spectral lines follow the standard ABS energy dispersion,

$$E^{\pm}_{1n,2n} = \pm\Delta\sqrt{1 - \tau_{1n,2n}\sin^2(\varphi_{1,2}/2)},$$

where $\tau_{1n,2n}$ corresponds to the transmission of the n-th channel in the first or second weak link. Since the second phase is fixed, $\varphi_2 = 3\pi/5$, ABS corresponding to the second weak link (red) do not disperse with φ_1, whereas those of the first junction (blue) dip towards zero as φ_1 approaches π. There is no hybridization between ABS at the two junctions and the spectral lines cross without forming gaps. As the junctions are brought closer, for $l/\xi_0 = 1, 0.5, 0.1$, multiple avoided crossings materialize, signaling the formation of Andreev molecules. Similarly, to the one-channel case [26], the amplitude of the avoided crossings increases as the separation is reduced and some discrete states are gradually pushed out into the continuum. At separation $l = 0.1\xi_0$, where the Andreev molecule fuses into a single weak link, only approximately half of the ABS remain in the gap and the states have shifted in phase to the right by $\varphi_2 = 3\pi/5$. Overall, the spectra of Fig. 1.16(b) for the multi-channel case shows qualitatively the same behavior as for the Andreev molecule in the single-channel case [26]. The most obvious global sign of hybridization remains the breaking of symmetry about the phase $\varphi_1 = \pi$. Since there are often phase offsets in experiments, it is difficult to verify that $\varphi_1 = \pi$. One could instead check for symmetry about the more easily identifiable point, $\varphi_1 = \varphi_1^0$, where the ABS are closest to zero in energy at a fixed phase φ_2. The multi-channel spectra indicate that the symmetry point φ_1^0 shifts from π to $\pi + \varphi_2$ as the separation l/ξ_0 goes from infinity to zero and that symmetry is broken for $l \lesssim \xi_0$.

1.2.4 Molecular Bound States

An eigenvector $\mathcal{B}_0$ which solves Eq. 1.31 corresponds to a closed trajectory or bound state of the Andreev molecule, formed due to interference between forward- and backward-propagating waves. There are three different types of closed cycles, or orbits, with two non-trivial ones which can be built from the EC and CAR processes shown in Fig. 1.15.

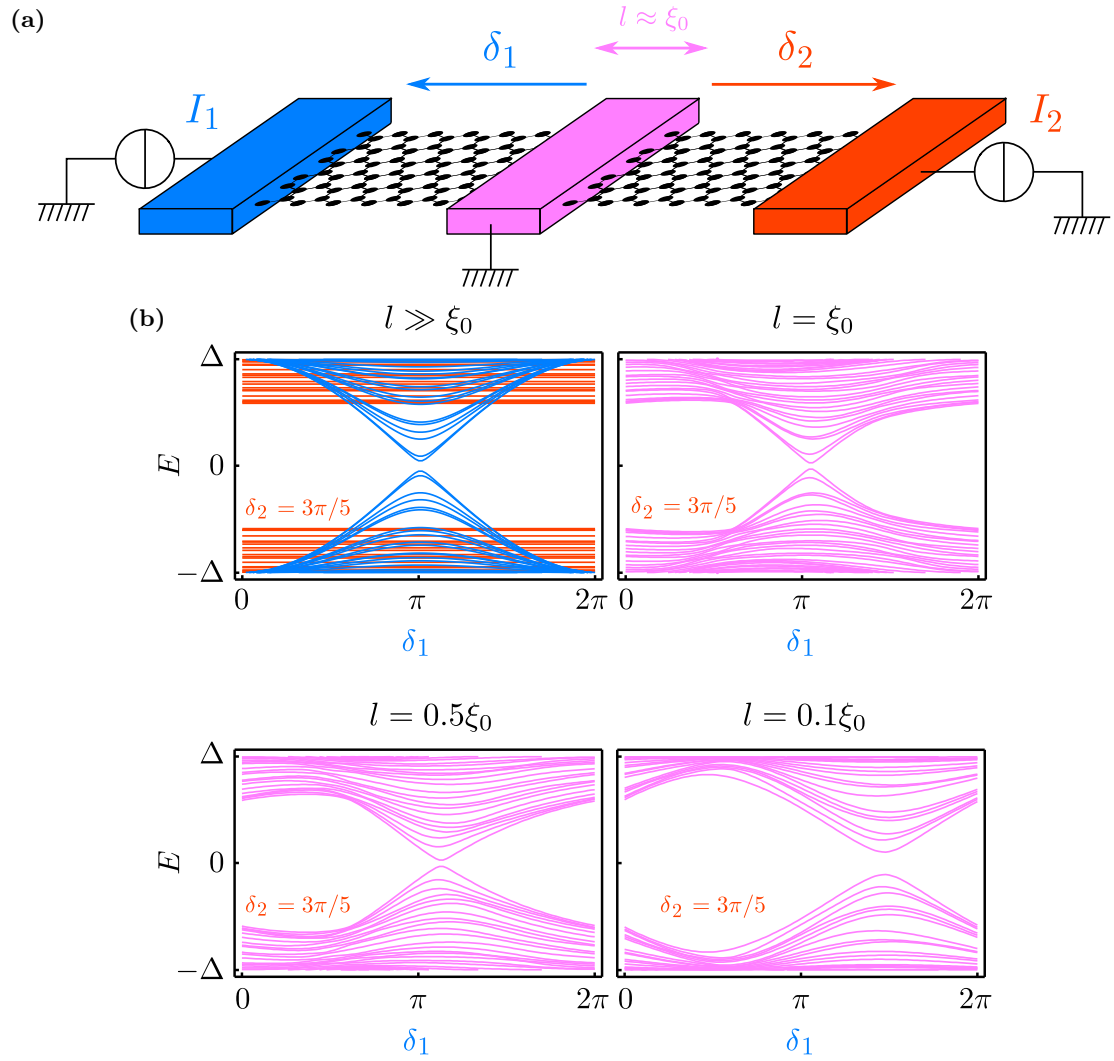

Figure 1.16: Spectra of multi-channel Andreev molecules. (a) An Andreev molecule is formed from a one-dimensional, multiple channel weak link, here a graphene nanoribbon, connected to three superconductors of which the central one has length l comparable to the coherence length ξ_0. (b) Spectra of an Andreev molecule for decreasing l/ξ_0. The randomly generated symmetric unitary matrices S_1 and S_2 are the same for each value of l/ξ_0 and describe scattering of weak links with $N = 20$ channels. Hybridization of Andreev states is indicated by the appearance of avoided crossings for $l/\xi_0 \lesssim 1$. Note that $S_1 \neq S_2$ and, for simplicity, the momentum is chosen such that $k_F l = 0 \ (\mathrm{mod} 2\pi)$, with $k_F l \gg 1$, for every channel.

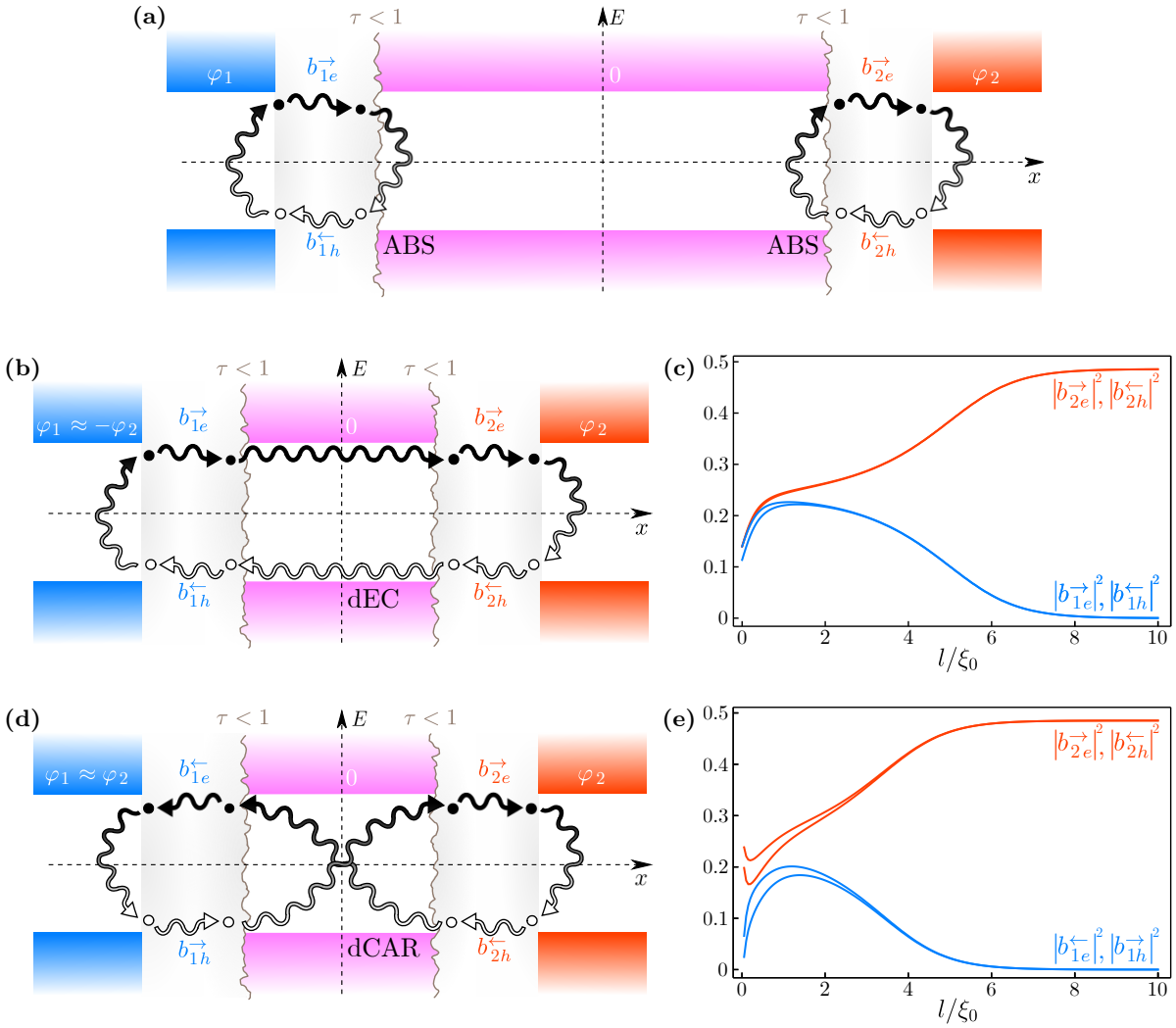
(a)
τ < 1
E
τ < 1
φ1
φ2
0
ABS
ABS
x
(b)
φ1 ≈ −φ2
φ2
dEC
(c)
l/ξ0
(d)
φ1 ≈ φ2
φ2
dCAR
(e)
l/ξ0

Figure 1.17: *(previous page)* Bound states of an Andreev molecule. (a) At large separation $l \gg \xi_0$ the only eigenstate is a conventional ABS, shown here localized at the second weak link by Andreev reflections at the central (purple) and second (red) superconductor. (b) At small separation $l \lesssim \xi_0$ and for superconducting phases $\varphi_1 \approx -\varphi_2$ there is an additional trajectory, double Elastic Co-tunneling (dEC), which extends across all three superconductors. (c) The likelihood of dEC (blue lines) and ABS (red lines) trajectories are plotted as a function of separation l/ξ_0 for $\varphi_2 = 0.5\pi$, $\varphi_1 = -0.48\pi$, $\tau \approx 0.94$ and $k_F l \gg 1, k_F l = 0 \pmod{2\pi}$. The dEC probability increase as the separation is reduced. (d) A second "molecular" trajectory extending across all superconductors is possible at small separation $l \lesssim \xi_0$ but for superconducting phases $\varphi_1 \approx \varphi_2$. This is called double Crossed Andreev Reflection (dCAR) and differs from dEC by additional Andreev reflections in the central superconductor. (e) The likelihood of dCAR and ABS trajectories are plotted as a function of l/ξ_0. Parameters are the same except for $\varphi_1 = 0.52\pi$ and $k_F l = \pi/2 \pmod{2\pi}$. The dCAR probability vanishes for large and small separation and is maximal at $l \approx \xi_0$. Results are obtained by numerically solving the eigenvalue equation, Eq. 1.31.

The trivial cycle is a conventional Andreev bound state at one of the weak links and is represented in Fig. 1.17(a) where the central superconductor is large, $l \gg \xi_0$. The closed orbit consists of two Andreev reflections at the second weak link, with the backward-propagating hole of amplitude $b_{2h}^{\leftarrow}$ being completely transformed into a forward-propagating electron of amplitude $b_{2e}^{\rightarrow}$ at the central superconductor (purple). Since the Andreev transmission probability t_S vanishes for large l/ξ_0, Fig. 1.15(d), the incident hole cannot be transmitted through the central superconductor. Likewise at the infinite first (blue) and second (red) superconductors, only Andreev reflection is possible. A conventional ABS does not connect particles on all three superconductors and therefore the supercurrent associated with it only flows between two superconductors.

With a shorter central superconductor, Fig. 1.17(b), one has the first non-trivial or "molecular" Andreev bound state: the loop passing through all three superconductors. This orbit consists of two simultaneous EC processes, one shown in Fig. 1.15(b), and the other its particle-conjugate dual in which a hole propagates in the opposite direction. Such a double elastic cotunelling (dEC) process transports two electrons from superconductor S_1 to superconductor S_2. Since the phases are fixed and all voltages are zero, this charge transfer corresponds to a unidirectional supercurrent flowing across the device. dEC-type bound states are probable when the normal scattering matrices have high channel transmissions and the phases $\varphi_{1,2}$ have opposing signs and values which result in an energy degeneracy in the limit $l/\xi_0 \to \infty$. In the case of a symmetric single-channel Andreev molecule [26], dEC is maximal when the phases satisfy $\varphi_1 = -\varphi_2$.

Fig. 1.17(c) shows the dEC bound state probability as a function of l/ξ_0 determined by numerically solving the eigenvalue problem, Eq. 1.31, for the lowest positive energy state of a symmetric, single-channel Andreev molecule of transmission $\tau \approx 0.94$. In red we plot the probabilities $|b_{2e}^{\rightarrow}|^2$ and $|b_{2h}^{\leftarrow}|^2$ corresponding to the orbit shown in Fig. 1.17(a) or the right part of Fig. 1.17(b). In blue we plot $|b_{1e}^{\rightarrow}|^2$ and $|b_{1h}^{\leftarrow}|^2$ which correspond to the complementary orbit

passing through the first weak link in Fig. 1.17(b). The eigenvectors are normalized so that the probabilities sum to 1 and the amplitudes a are related to the b's by the scattering matrix S_N. To maximize dEC, the phases are fixed at $\varphi_2 = 0.5\pi$ and $\varphi_1 = -0.48\pi$. The slight detuning of φ_1 from -0.5π allows being sufficiently far from the degeneracy such that there is no mixing between the eigenstates of sides 1 and 2 at $l/\xi_0 = 10$. In principle at the exact degeneracy and arbitrarily large l/ξ_0, a viable eigenstate can consist of equal weights at the first and second weak links.

At large separation, $l/\xi_0 \approx 10$, both probabilities at the second weak link (red) are approximately 0.5 whereas those at the red weak link (blue) are almost zero, indicating that the eigenstate is a conventional ABS as in Fig. 1.17(a).

As the separation is reduced, the weights at the first weak link (blue) start to increase and those at the second weak link (red) decrease, indicating the formation of a dEC state. The position of the step will depend on the detuning of φ_1 from $-\varphi_2$. Near $l/\xi_0 \approx 1$, the orbit is approximately equally distributed between the two weak links. The decomposition of dEC into two simultaneous EC processes leads to the qualitatively similar form of the probabilities in blue with the EC probability $|t_S|^2$ of 1.15(d).

For even smaller separation, both the red and blue probabilities decrease and are compensated by an increase in the amplitudes $|b^{\leftarrow}_{1e,2e}|^2$ and $|b^{\rightarrow}_{1h,2h}|^2$ (not shown) of the counter-propagating orbit given by reversing the directions of the arrows in Fig. 1.17(b). The relative weight of these two trajectories will be determined by the value of the phase difference φ_2. This can be understood by considering the complementary time-reversed ABS trajectory to the one shown in Fig. 1.17(a). When the phase φ_2 is zero or π, such that the supercurrent is zero, these two trajectories have equal weights and compensate each other. At extrema of the supercurrent one trajectory will dominate. This is why with our choice of $\varphi_2 = \pi/2$ the red probabilities in Fig. 1.17(c) approach 0.5 for large l/ξ_0, near a supercurrent extremum for the secon weak link. The situation is similar for a dEC orbit and when the separation approaches zero, the total phase drop across the device is $\varphi_2 - \varphi_1 \approx \pi$, so the dEC supercurrent vanishes and both trajectories coexist. This is why all probabilities approach 1/8 near $l/\xi_0 = 0$ in Fig. 1.17(c), resulting in approximately equal clockwise and counter-clockwise orbits. The additional splitting of the blue lines results from normal scattering and is absent when $\tau = 1$.

The second molecular bound state, dCAR, is shown in Fig. 1.17(d), and with respect to the dEC orbit involves two additional quasiparticle conversions in the central superconductor and a reversal of current direction at the first weak link. During the conversion an incident electron of energy E is reflected as a hole of energy $-E$ which results in the crossing of trajectories at the central superconductor and in the twist relative to the dEC diagram Fig. 1.17(c). dCAR describes supercurrent flowing from the central superconductor to the outer ones and cannot occur for a floating central island, or without a connection to ground.

The dCAR probability is plotted in Fig. 1.17(c) for the same $\varphi_2 = \pi/2$ but with $\varphi_1 = 0.52\pi \approx \varphi_2$ in order to maximize the effect while maintaining a detuning to avoid a trivial degeneracy. Note that although the probabilities in red are identical to those for dEC, Fig. 1.17(c), the probabilities in blue are $|b^{\leftarrow}_{1e}|^2$ and $|b^{\rightarrow}_{1h}|^2$ to take into account the reversal of the trajectory on the first weak link. There is a non-physical numerical instability at exactly $l/\xi_0 = 0$ so the x-axis extends from $l/\xi_0 = 0.05$ to 10. As expected, at large separation, $l/\xi_0 = 10$ the eigenstate is an ABS localized at the second weak link.

As the separation is reduced the probability shifts to the first weak link, much as with

dEC. The increase in probability at the first weak link (blue lines) occurs at smaller l/ξ_0 than for dEC, most likely a result of the high value of transmission which leads to weak dCAR hybridization. After reaching a maximum at $l/\xi_0 \approx 1$ the blue lines take a sharp downturn and approach zero as the separation is further reduced. The probability for dCAR follows the Andreev reflection probability which vanishes as $l/\xi_0 \to 0$. As with dEC the probabilities describing propagation through the second weak link, including the time-reversed ones not shown, approach approximately the same value as $l/\xi_0 \to 0$. However, since the probability of all trajectories at the first weak link must vanish, the red lines approach a value of 1/4 instead of 1/8 as with dEC. The additional splitting of the probabilities for $l/\xi_0 \lesssim 1$ is also due to imperfect transmission. Unsurprisingly, the overall shape of the dCAR probabilities (blue lines) is similar to that of the CAR probability plotted in Fig. 1.15(d).

In the general multi-channel, non-symmetric case and as a function of the separation the eigenstates will be mixtures of conventional ABS and molecular ABS. The phase configuration necessary for molecular orbits will coincide with the position of level crossings in the large separation ABS energy spectrum such as in Fig. 1.16(b) for $l = 10\xi_0$.

1.3 Multi-channel Andreev molecule in 2D: the role of disorder

Up to now, we have treated Andreev molecules without any disorder in the models. However Andreev molecules emerge when ABS of different junctions interfere with each other and form a delocalized state. In mesoscopic systems, interference may be destroyed by disorder and one can legitimately wonder whether or not Andreev molecules can form in realistic devices where weak links are connected to thin film diffusive superconductors. Although the superconducting gap Δ remains largely unaffected by non-magnetic disorder, in the limit $l_0 \ll \xi_0$, where l_0 is the mean free path in the diffusive superconductor, the effective superconducting coherence length is reduced to $\sqrt{\xi_0 l_0}$. As a consequence, for an isolated junction, the spread of the wave function is reduced by disorder but the spectrum, which only depends on Δ, remains unchanged. However, in an Andreev molecule, disorder reduces the overlap of wave functions of adjacent junctions, hence degrading the probability of dEC and dCAR and changing the spectrum. The one-dimensional approach we described so far is powerful to obtain a simple understanding of Andreev molecules but it does not describe the effect of disorder. In this section we present a tight-binding model for Josephson devices made with diffusive superconductors in order to demonstrate that Andreev molecules and the resulting nonlocal effects survive in realistic experimental conditions. Moreover, this approach can easily generalize the concept of Andreev molecule in two dimensions, which is relevant experimentally as thin films of superconductors have typical thicknesses smaller than the superconducting coherence length.

1.3.1 Tight-binding description of Andreev molecules

In this approach to describe Andreev molecules (see Fig. 1.18(a)), we decompose the space over a $N \times N$ square lattice with lattice constant α in discrete sites labeled (i, j) where i and j are integers. In the corresponding base $|i, j\rangle$, the normal part of the Hamiltonian $H_0 =$

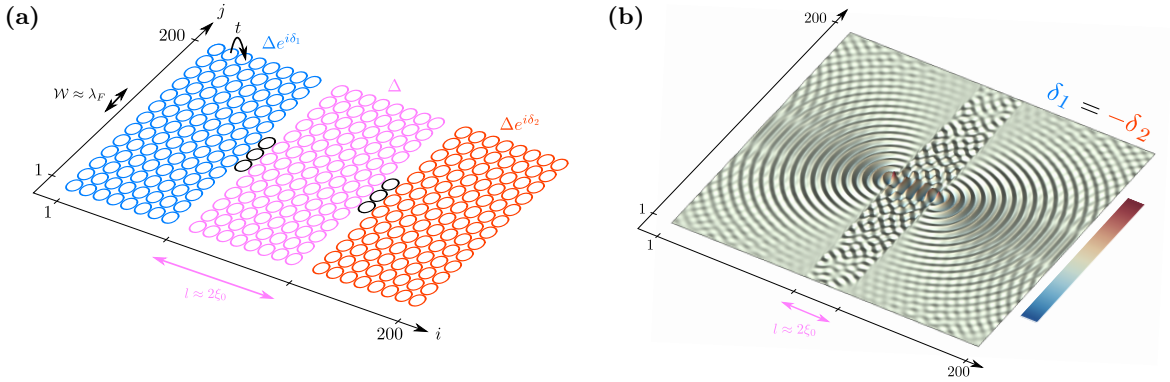

Figure 1.18: Tight-binding description. (a) Illustration of the discretization for the tight-binding approach: each site is a circle. For clarity, we draw fewer sites than we actually use for calculations (200×200). The weak links are in black and their widths are chosen such that each QPC has a single channel. (b) Real part of u_ψ^{ij}, the electron part of the wave function $\psi(i,j)$, when hybridization is maximum ($\delta_1 = -\delta_2$) for a device with no disorder. Interference between ABS leads to the formation of fringes between the junctions, which shows the hybridization into an Andreev molecule. The checkerboard patterns in the corners are finite size effects due to reflections on the edges. Parameters used for calculations are either given in the figures or: $\alpha = 1$, $l = 28$, $t = 10$, $\delta t = 0$, $\Delta = 0.5$, $\delta_2 = \pi/2$, $\mu = 11$ and $\mathcal{W} = 6$. This gives $\xi_0 \approx 12.7$, $l_0 = \infty$ (or rather the size of the device N) and $\lambda_F \approx 6.3$.

$\frac{-\hbar^2}{2m}\left(\partial_x^2+\partial_y^2\right)-\mu$ becomes

$$H_0=\sum_{i,j}\left(4t-\mu_{ij}\right)|i,j\rangle\langle i,j|-t\sum_{\sigma=\pm1}|i+\sigma,j\rangle\langle i,j|+|i,j+\sigma\rangle\langle i,j| \ . \tag{1.33}$$

The first term corresponds to the on-site energy and the second one to the coupling between adjacent sites by a hopping energy $t=\hbar^2/2m\alpha^2$. To describe electrons in continuous media, we require that the Fermi wavelength exceed the lattice spacing ($\lambda_F>\alpha$), a condition satisfied for $\mu\leq t$. In the following, we set $\mu\approx t$ such that the wavelength and superconducting coherence length are given by $\lambda_F\approx 2\pi\alpha$ and $\xi_0\approx 2t\alpha/\pi\Delta$, respectively. Since α is the spatial resolution and ξ_0 is the spread of Andreev molecules, we choose parameters such that $\xi_0>\lambda_F>\alpha$ and our resolution is sufficient to observe effects due to the overlap of ABS wave functions. In order to build a global matrix describing the system, we first define local BDG matrices in Nambu space that describes individual sites of the lattice

$$H_{0D}\left(i,j\right)=\begin{pmatrix}\epsilon_{i,j} & \Delta e^{i\varphi_{i,j}}\\ \Delta e^{-i\varphi_{i,j}} & -\epsilon_{i,j}\end{pmatrix}$$

where $\epsilon_{i,j}=4t-\mu_{i,j}+U_{i,j}$, $U_{i,j}$ is a local electrostatic potential, $\Delta=|\Delta|\,e^{i\varphi_{i,j}}$ and $\varphi_{i,j}$ is the local superconducting phase for the site labeled(i,j). We also introduce an on-site chemical potential μ_{ij} to define the shape of the device. Sites on the boundary of superconductors and weak links have $\mu_{ij}\gg t$ and are therefore kept empty. The i-th line of the lattice corresponds then to the assembly of N these matrices coupled by horizontal hopping terms between adjacent sites $T_{\rightleftarrows}=\mathrm{diag}\left(-t,t\right)$

$$H_{1D}\left(i\right)=\begin{pmatrix}H_{0D}\left(i,1\right) & T_{\rightleftarrows} & 0 & 0\\ T_{\rightleftarrows} & H_{0D}\left(i,2\right) & \ddots & 0\\ 0 & \ddots & \ddots & T_{\rightleftarrows}\\ 0 & 0 & T_{\rightleftarrows} & H_{0D}\left(i,N\right)\end{pmatrix} \ .$$

The total matrix $\mathcal{H}_{2D}$ describing the $N\times N$ lattice in 2 dimensions is then built by coupling N of these lines

$$\mathcal{H}_{2D}=\begin{pmatrix}H_{1D}\left(1\right) & T_{\updownarrow} & 0 & 0\\ T_{\updownarrow} & H_{1D}\left(2\right) & \ddots & 0\\ 0 & \ddots & \ddots & T_{\updownarrow}\\ 0 & 0 & T_{\updownarrow} & H_{1D}\left(N\right)\end{pmatrix}$$

with vertical hopping diagonal matrices $T_{\updownarrow}=\mathrm{diag}\left(t,-t...t,-t\right)$ of dimensions $2N$. The resulting Hamiltonian $\mathcal{H}_{2D}$ is a $2N^2\times 2N^2$ matrix, where the factor two accounts for the electron and hole parts of the electronic states. The energy spectrum of the system corresponds then to the ensemble of eigenvalues of $\mathcal{H}$ while the eigenvectors are the quasiparticle wave functions (see Fig. 1.18(b)).

1.3.2 Andreev molecules robustness against disorder

To reproduce the results of the preceding sections, we focus on a superconducting double quantum point contact (QPC), as shown in Fig. 1.19(a). This geometry also corresponds to

back-to-back superconducting atomic contacts. We choose the width $\mathcal{W} \sim \lambda_F$ of the weak links such that only one conduction channel is open in each QPC. Within the tight-binding approach, the disorder associated with the diffusive nature of superconductors can be described by giving a random Gaussian distribution to the hopping energies with a mean value t_0 and a standard deviation δt. The timescale over which an electron is scattered is then approximately $\hbar/\delta t$ and an order of magnitude estimate of the mean free path is $l_0 \sim t_0\alpha/\delta t$ provided that this is smaller than the size of the device.

Fig. 1.19(b) shows the spectrum obtained for two QPCs separated by twenty sites, which is more than twice the effective superconducting coherence length $\sim 2.5\sqrt{\xi_0 l_0}$. For varying δ_1 and fixed $\delta_2 = 3\pi/5$, we recover the main features that we observed in the one-dimensional case. We see the appearance of avoided crossings at $\delta_1 = \pm\delta_2$ between ABS that were originally localized at different junctions. In the absence of disorder in Fig 1.19, the hybridization of ABS is revealed by the interference pattern in the wave function, which consists of circular waves of period λ_F centered at the QPCs and decaying exponentially into the outermost superconductors. In between the QPCs, the circular waves overlap and interfere leading to parallel fringes demonstrating the hybridization of ABS into an Andreev molecule.

As we add disorder, this regular interference pattern is severely destroyed and the wave functions resemble a random speckle pattern. As expected, we also observe that the wave functions are more localized than for a ballistic sample with no disorder. The probability distribution of the wave function is plotted in Fig. 1.19(c), (d) and 1.19(e) for fixed $\delta_2 = 3\pi/5$ and three different superconducting phases δ_1 indicated in Fig. 1.19(b) (red, blue and magenta circles). As in Fig. 1.5(b) where the wave function envelope is calculated in one dimension, regions of high probability correspond to the localization of a single Cooper pair. Away from the avoided crossings (red and blue circles), the probability peaks on one of the QPCs only, which is natural as the ABS are not hybridized. On the other hand, for maximum hybridization (magenta) the probability is equally distributed over the two QPCs. We have shown that tight binding can capture the formation of Andreev molecules in 2D and in the presence of disorder. The technique can easily be extended to model more sophisticated structures, Andreev analogs of multi-atomic molecules such as polyacetylene, or even cyclic molecules such as benzene.

When the distance between QPCs becomes smaller than ξ_0 (Fig. 1.20), the ABS start to hybridize more strongly since the overlap of their wave functions becomes significant. In this regime, the Andreev molecule shows a large nonlocal Josephson effect. In Fig. 1.20(a), we show three current-phase relations of the first junction for three different superconducting phase differences across the second junction. As in the one-dimensional case, we observe the appearance of a zero-phase current, which modulates with δ_2 and represents a significant fraction of the maximum supercurrent. Moreover it is clear in this comparison that the critical current of the first junction (i.e. the maximum of I_1) modulates with δ_2. The same calculations performed for a ballistic sample (Fig. 1.20(b)) provides similar results, showing that disorder does not affect qualitatively the formation or behavior of an Andreev molecule.

In conclusion, as for ABS in a single junction, we observe that the main consequence of disorder on Andreev molecules is to effectively reduce the superconducting coherence length. This imposes the junctions to be close enough such that l is smaller than the diffusive superconducting coherence length, but it does not induce qualitative changes and non-local effects are still substantial. Andreev molecules can thus be detected in devices made of diffusive aluminum since the diffusive superconducting coherence length is 150 nm [60], as compared to 3 μm in

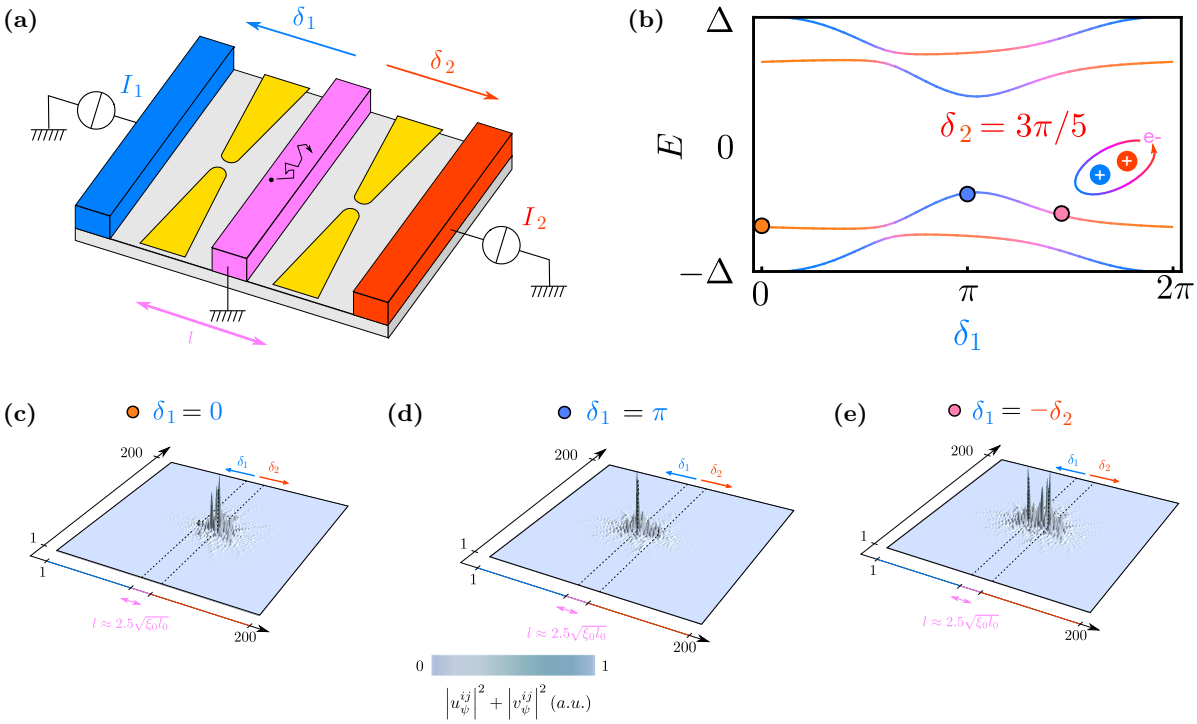

Figure 1.19: Andreev molecule in a double superconducting quantum point contact. (a) Schematic of a device based on two point contacts (QPC) used as weak links between disordered superconducting electrodes (blue, magenta and red). In these electrodes, quasiparticles propagate in a diffusive way. (b) Spectrum of a two-dimensional Andreev molecule as a function of δ_1 at fixed δ_2 for a disordered device ($\delta t/t_0 = 0.2$). (c-d-e) Square modulus of the wave function for three different phases δ_1 at fixed $\delta_2 = 3\pi/5$ (see b). The red (resp. blue) dot corresponds to an electronic state localized on the second (resp. first) junction with $\delta_1 = 0$ (resp. $\delta_1 = \pi$). For the magenta point, hybridization is maximum ($\delta_1 = -\delta_2$) and the electronic states are fully delocalized on the two junctions. Parameters used for calculations are either given in the figures or: $\alpha = 1$, $l = 20$, $t_0 = 10$, $\delta t = 0.2$, $\Delta = 0.5$, $\mu = 11$ and $\mathcal{W} = 6$. This gives $\xi_0 \approx 12.7$, $l_0 \approx 5$, $\sqrt{\xi_0 l_0} \approx 8$ and $\lambda_F \approx 6.3$. The number of sites is 200×200. Separations between the three superconductors are indicated by dashed lines and colors along one axis. The weak links are small openings in the center of these separations.

the ballistic limit. A Josephson device showing nonlocal effects could therefore be fabricated using conventional techniques of nanofabrication, which have a resolution down to 10 nm.

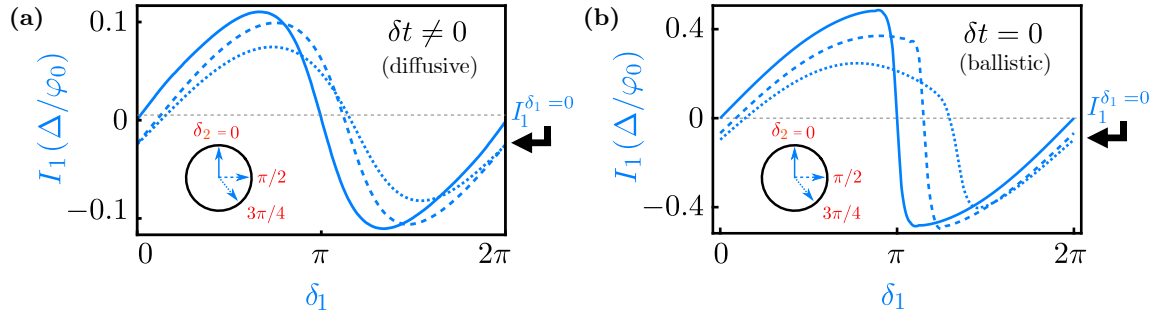

Figure 1.20: φ-junction in disordered two-dimensional devices. (a) Supercurrent I_1 flowing through the first junction as a function of δ_1, for three different superconducting phase differences across the second junction δ_2, in a two-dimensional disordered device ($\delta t/t_0 = 0.2$). We choose $l = 4\alpha$ such that $l \lesssim \sqrt{\xi_0 l_0}$. We observe an important 0-phase current $I_1^{\delta_1=0}$, which modulates with δ_2. (b) Current-phase relation calculated for a ballistic device ($\delta t/t_0 = 0$). Here, we choose $l = 8\alpha$ such that $l \lesssim \xi_0$. We observe that nonlocal effects are qualitatively the same with or without disorder. For these calculations, we use the following parameters with $\alpha = 1$: $l = 4$, $t_0 = 10$, $\delta t = 0.2$ (for the diffusive case), $\Delta = 0.5$, $\mu = 11$ and $\mathcal{W} = 6$. This gives $\xi_0 \approx 12.7$, $l_0 \approx 5$, $\sqrt{\xi_0 l_0} \approx 8$ (for the diffusive case) and $\lambda_F \approx 6.3$. The number of sites is 200×200. The supercurrent is obtained from the highest 1000 eigenstates of negative energies found numerically. They include the ABS of negative energies, from zero down to approximately -3Δ.

1.4 Implications for experiments

The preceding theory is necessary to understand the different aspects of the formation of an Andreev molecule. To perform actual experiments, we must identify the physical constraints and find a technological platform to realize devices.

- **Main physical constraints**

The three main ingredients to engineer Andreev molecules are the distance between the junctions, the transmission and the number of conduction channels in the junctions. The most crucial dimension in the design is the distance between the junctions. The splitting of the energy levels, i.e. the intensity of the hybridization, is in a best-case scenario of the order of $e^{-\frac{l}{\xi_d}}$ with l the distance between the junctions and ξ_d the dirty coherence length of the superconductor, as shown in Eq. 1.11. The fundamental idea behind this dependence is the size of the overlap of the ABS of the junctions. Since the two junctions host ABS with a size ξ_d, we need to place the junction at a distance of the order of ξ_d to get a measurable effect.

All the more, in a general quantum physics problem the overlap of two wavefunctions of finite size varies on the dimension of the system. In one dimension, a Josephson junction is made of

a weak link considered as a Dirac point and one-dimensional superconducting islands. In this configuration, the wavefunction of an ABS of a junction is centered at the weak link and its wave function has an envelope proportional to $e^{-\frac{x_{wl1}-x}{\xi_d}}$ with x_{wl1} the position of the weak link and x the distance from the weak link. If a second junction is placed at a distance l from the first junction with a wavefunction envelope similar $e^{-\frac{x_{wl2}-x}{\xi_d}}$ but centered at its weak link x_{wl2}, the overlap of the wavefunction will happen on the distance l separating the junctions. With the exponential decrease of the wavefunctions along the x-axis, it is considered that the ABS of each junction are overlapping and so hybridizing if $l \leq \xi_d$. One important remark is that since the system is in one dimension all the weight of the wavefunctions is along one axis, giving no space to the wavefunctions to spread other than this one axis. And so, the dimension of the system is favoring the hybridization of the junctions.

In a three-dimension system, the weak links are still considered as Dirac points but the superconducting islands are now considered as three-dimensional spaces where the ABS wavefunctions can spread. Thin films superconducting island, sketched on Fig.1.21, can be approximate as such systems, for example. In these systems, the ABS are spread on a wider space than in one dimension. If two junctions are placed at the same distance l as in one dimension one could be thinking that the overlap of the would be the same. However, the ratio of wavefunctions overlapping is smaller compared to the one-dimensional case, and correspond to a smaller overlap. If the overlap is smaller so is the hybridization of the junctions and the spectrum of such Andreev molecule will contain smaller avoided crossings. To obtain the same ratio of the wavefunctions overlapping hence the same hybridization of the junctions, the junctions have to be brought closer to one another. A similar explanation can be given for two-dimension systems. So, the dimensionality of the system can make the hybridization harder to happen.

In a deeper theoretical work has been made by Kornich et al. [57, 61] which takes into account the change in dimensionality of the wave function. They find for a "concrete setup" made of two Josephson junctions in aluminum with high transmission separated by 50 nm that the energy splitting would be around few µeV. For comparison in our theoretical work considering only one-dimensional systems, we would get splitting one order of magnitude bigger.

The second and third important points are the transmission and the number of conduction channels in the junctions. The transmission of the conduction channels is critical. For low transmission junctions, $\tau \ll 1$, as we have seen in Sec 1.1.5.1, the fraction of non-local current compared to the conventional supercurrent will be in the best case proportional to τ. So maximizing this value is important. Also, the number of conduction channel has its importance depending on the type of measurement intended. Since the non-local current is proportional to a fraction of the critical current of the junction, higher critical current leads to higher non-local current. However, higher current for a given voltage means more dissipation and superconducting Josephson junctions needs to be operating at cryogenic temperature. A point of equilibrium needs to be found in order to get the maximum critical current in the junctions without risking dissipating too much heat in the cryostat. Considering the cooling power of a typical dry cryostat to be of few tens µW to maintain a temperature of few mK, the current of one perfectly transmitting channel in aluminum to be of 50 nA and necessary in series resistance for measurement to be of 10 000 Ω, it seems reasonable to aim at the order of ten conduction channels per junction. More than this order of magnitude will result in current too high to be easily measurable at cryogenic temperature due to heat dissipation.

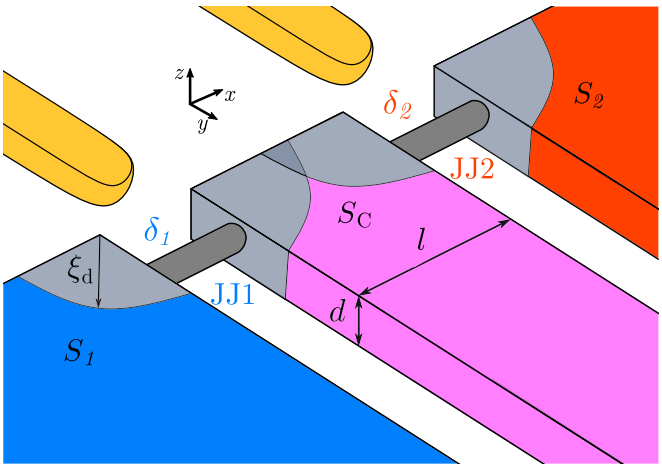

Figure 1.21: Perspective drawing based on Fig. 2(a) from [57].The two junctions are represented with superconducting islands, S_1 S_2 and S_C, made with thin films. Each junction, JJ1 and JJ2, has respectively a phase difference of δ_1 and δ_2. Each junction has side gates represented in yellow. The spreading of the ABS wave function in the superconducting leads is represented in shade of grey. The overlap is the darker grey part. The spreading in two dimensions exhibits that, for a distance l, the overlap of the wave function is reduced since y component do not interact as much as in one dimension.

And with less than this value, the variation of the switching current of the junctions would be too small to be measurable. For spectroscopy measurement, we want ideally only one channel per junction. The size of the energy gap for dEC and dCAR is determined by the channel with the smallest transmission which makes it possibly smaller for multi-channel junctions. In addition, the spectral lines will have some width, so that if the number of channels is high the energy spectrum will be dense, as we show in Fig 1.16, and it will not be possible to distinguish them.

Finally, with all these constraints in mind we can discuss which technological platform is most promising to build an Andreev molecule device.

- **Choice of technological platform**

We need to determine the most suitable technology with which it is possible to craft Josephson junctions with few high-transmitting channels and to place two of these junctions close to one another with a middle island connectable. Among the possibilities for fabricating Josephson junction, two technologies stand out: stacked aluminum tunnel junctions and InAs-Al nanowire based junctions.

The stacked aluminum tunnel junctions design is made of two tunnel junctions vertically stacked. The device is composed of three aluminum layers and two aluminum oxide layers at the interface of two aluminum layers. Each junction is made of two aluminum layers and one oxide layer. And the two junctions share the middle aluminum layer which plays the role of a common electrode, as shown in Fig. 1.22. We end up with two vertically stacked Josephson

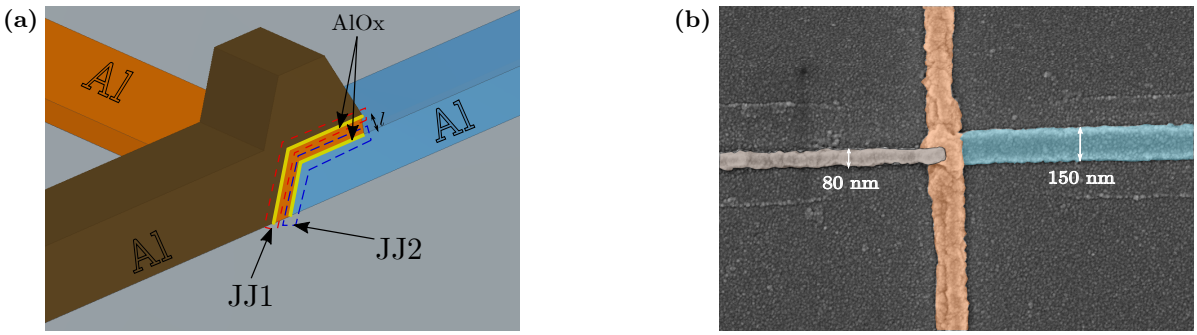

Figure 1.22: Stacked aluminum tunnel junctions. (a) 3D scheme of a cut of stacked junctions. The stacked junctions are a superposition of three aluminum layers, in blue, orange and brown, with two oxidized layers ,in yellow. This setup defines two junctions JJ1 and JJ2 with a spacing l corresponding to the thickness of the orange layer. (b) SEM image with false color of stacked junctions. The three layers define in (a) are colorized. The thickness of the orange layer is $l \approx 50\,\mathrm{nm}$

junctions for which the separation length is defined by the thickness of the second aluminum layer, in orange. The biggest advantage of this design is the possibility to determine the spacing between the junctions with great precision on the order of a few nanometers. This precision is possible using metal evaporator with electronic gun which allows evaporating aluminum at 0.5 nm/s. However, this design has some drawbacks. It is not a common technique and needs to be developed from scratch. Also, the number of channels, their transmission and the distance between the junction are fixed for each device and cannot be tuned inside the cryostat, for example. Another drawback is the difficulty to create few high transmission channels in a tunnel junction. The oxidation process used to create the weak links of the junctions results in low transparency barriers. The junctions have S/λ_f^2 number of channels available, with S the surface of the junctions and λ_f the Fermi wavelength, with low transmission. One strategy to create few high transmission channels in tunnel junctions is to send electrical pulses to the junctions as in [62]. However, this technique is not easy to master and creating only few channels is demanding. Lastly, this design is not scalable if we want to create more complex molecules with an increasing number of junctions.

The first part of this thesis was an attempt to develop a working recipe to fabricate Andreev molecules based on stacked Josephson junctions. This try was motivated by the work of Tolpygo et al. [62]. The most advanced recipe permits to craft two stacked junctions with in the order of a hundred well-transmitted channels. Even if promising the number of channels was too high to be measurable. Unfortunately, no recipes were found to overcome this limit, which leads to start a new design based on InAs nanowires which became a more promising technological platform.

The second strategy is to use InAs-Al nanowires as the canvas to create two Josephson junctions. These nanowires are made with a semiconducting core of InAs and an epitaxially grown Al shell, this specific fabrication process allows having a hard gap and makes them a very interesting platform to make Josephson junctions. It is achieved by removing the Al shell of the nanowire at two places and exposing the core. The exposed parts in InAs represent the

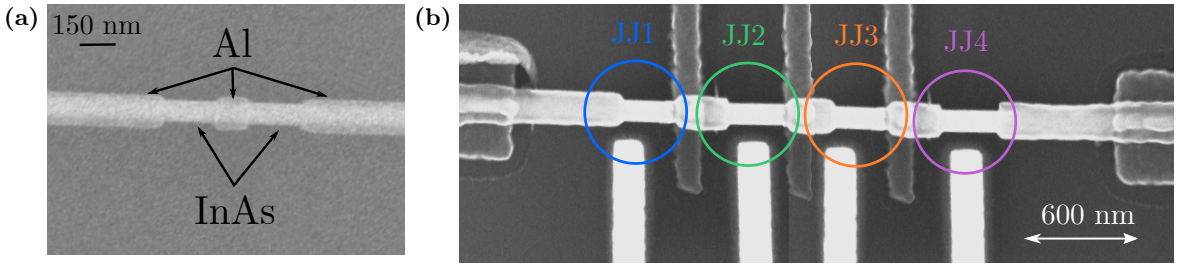

Figure 1.23: (a) A full-shell nanowire etched in two places, exposing the core of the nanowire made of InAs. The nanowire is not connected to the rest of the circuit. (b) SEM image showing multiple junctions Andreev molecules. The design is easy to scale to multiple junctions by juxtaposing them. The nanowire is connected to the rest of the circuit with also the presence of side gates for each junction by electrodes (left, right, and top) and side gates (bottom) allow tuning the channel transmissions of each junction independently.

weak links of the junctions and the rest with the aluminum shell still in place represents the superconducting islands, as shown in Fig 1.23(a). This technology has many advantages. One of the most noticeable is the capability to tune the number and the transmission of the conduction channels. It is feasible because of the semiconducting nature of InAs which can be depleted by applying an electric field with a side gate. This technology is also very common nowadays with all the effort put towards the detection and the manipulation of Majorana fermions. It helps to find new and more reliable fabrication technique. Lastly, the design is scalable as shown in Fig 1.23(b). Once we have tackled the way to fabricate an Andreev molecule with two junctions, adding more junctions to engineer more complex molecules is straight forward. The only two drawbacks of this technique are the reliability of the etching process to precisely remove the aluminum shell and the numerous precise lithography steps needed to build a device. A deeper review of the fabrication process is presented in Chap. 3.

2 Experiments to observe Andreev molecules

The two main signatures of Andreev molecule at equilibrium are the spectral avoided crossings and the non-local current-phase relations, which are formed when ABS hybridize through non-local processes. The non-equilibrium case, in which the junction voltages are non-zero, was considered by Freyn et al. [17] and has been investigated experimentally [23, 24]. The interpretation of their results is complex as dynamic phenomena such as mutual phase locking [63] can lead to similar signatures. On the contrary, the equilibrium experiments at zero voltage, detailed below, should provide a signature easier to interpret as the detection of Andreev molecules.

In this chapter, we present one experiment and two proposals of experiments which aim to probe the signatures of an Andreev molecule. The experiment is a current bias switching measurement which probes the nonlocal Josephson effect by applying and measuring supercurrent across the junctions. The first experiment proposal presents a phase bias switching measurement which explores further the nonlocality of the Josephson effect by applying phase and measuring supercurrents. The second proposal is a Josephson spectroscopy of an Andreev molecule, which aims to access the transition between the ground state and the first excited state of the Andreev molecule to witness the avoiding crossings.

2.1 Current bias switching measurement

As seen in Chap. 1, the hallmark of hybridization of Josephson junctions is the dependence of one junction's switching current on the supercurrent passing in the other junction. The objective of this experiment is to measure this dependence in a two junction Andreev molecule. Due to technical difficulties and time constraints, a full measurement of the junction's current-phase relation was not performed. However the experiment described below is similar and helps to determine with precision the supercurrent of one junction while current biasing the other junction.

2.1.1 Circuit design and principle

The Andreev molecule, made of two Josephson junctions, defined by the dotted rectangle in the center of Fig. 2.1 is the heart of the circuit. The two junctions JJ1 and JJ2 composing the molecule are made out of epitaxial InAs-Al full-shell nanowires coming from a collaboration with Peter Krogstrup from the University of Copenhagen [25]. These nanowires allow crafting superconductor-semiconductor-superconductor junctions in which the supercurrent can be modulated by an electric field. The junctions share a common superconducting island in pink in fig. 2.2(b) which separates the junctions by $l \approx 300\,\mathrm{nm}$. This island is connected to ground,

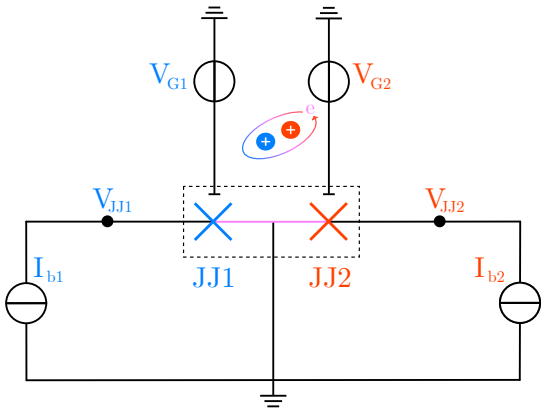

Figure 2.1: Simplified equivalent circuit of sample AM14. The central part inside the dotted line is the Andreev molecule. It is composed on one side of a Josephson junction JJ1 (in blue) and on the other side of another Josephson junction JJ2 (in red). The middle line in pink connected to ground represents the central island of the molecule made of aluminum. The upper part of the scheme corresponds to the two gates voltage connected to voltage sources (V_{G1}, V_{G2}) necessary to adjust the weak link characteristics of each junction. Two independent current sources (I_{b1}, I_{b2}) bias each junction independently.

which allows current biasing each junction independently with sources I_{b1} and I_{b2}. An electrode placed near each weak link is used to apply a gate voltage and modulate the junction conductance (Fig. 2.1, V_{G1}, V_{G2}). Lastly, two voltage probes are used to measure the junction voltages V_{JJ1} and V_{JJ2}. With this setup, it is then possible to tune the channel transmissions, current bias and measure the voltage of each junction independently. Details of sample fabrication and the measurement setup are given in Sec. 3.1 and Sec. 3.1. The advantages of the design shown in Fig. 2.1 are:

- The sample is the simplest possible while allowing independent measurement of the current-voltage characteristics of each junction.
- We can tune and measure each junction independently before performing more complex measurements. For example, the first junction can be measured with the second junction grounded.
- It is straight forward to add more junctions or atoms to the molecule.
- It is easy to short one of the junctions to form a superconducting loop and perform a phase bias switching measurement as in Fig. 2.12.

To measure the hybridization of Andreev Bound States in this circuit, one needs to measure the variation of the switching currents which should be larger than the switching noise. Since the expected variations are relative to the size of the switching current of the junctions, one firstly needs to maximize them. Higher supercurrent leads to higher relative variation of amplitude and would be more detectable. The conductance of the InAs-Al nanowire based semiconducting

PARAMETER	SAMPLE AM14
Length weak link 1 l_{wl1}	331 nm
Length weak link 2 l_{wl2}	322 nm
Length between weak links l	329 nm
Parasitic resistor R_{p1}	41.6 Ω
Parasitic resistor R_{p2}	41.2 Ω
Parasitic resistor R_{p3}	33.8 Ω

Table 2.1: Parameters of sample AM14 presented in this chapter.

weak links determines their critical currents. The semiconducting nature of the weak links makes them tunable by an electric field. Their conductance can be either enhanced or reduced by an electrical field in close proximity.

One can use the side gates maximize their supercurrent. After adjusting the gate voltages to have high switching currents, we perform a current bias switching measurement. The variation in the switching current of JJ1 is measured for different fixed values of current in JJ2. We start by applying a fixed current bias to JJ2, using I_{b2}, then ramp the current in the other junction, JJ1 using I_{b1}, until it switches. This sweep gives the switching current value of JJ1 for a defined value of current in JJ2. After one sweep, the bias current I_{b2}, is changed and JJ1 is swept again from zero until it switches. If the two junctions are hybridized, the switching current of JJ1 should depend on the supercurrent of JJ2. In Sec. 2.1.3, this current bias switching protocol is used to measure the hybridization of the junctions in device AM14 (Fig. 2.2(a)).

It is important to note that fixing the current bias does not fix the phase in the case of hybridized junctions. The current-phase relation (CPR) of one junction might involve the phase of the other junction, as it is the case for example for the analytical CPR for small transmission junctions in Eq. 1.18.

Even if the exact value of the phases is not known, their sign is related to the sign of the current and spans an interval from zero to approximately π for a single high-transmission conduction channel (Fig. 1.2(b)). As both junctions can be biased in a large range from $-I_{sw}$ to I_{sw}, one can measure the two specific configurations $\delta_1 = \delta_2$ and $\delta_1 = -\delta_2$. These configurations correspond to the two microscopic mechanisms, dEC and dCAR respectively. Being capable of putting the device in these two configurations greatly help

The results presented in this chapter were obtained with the sample AM14 (see Fig. 2.2) whose parameters are listed in Table 2.1.

2.1.2 Control measurements

Control experiments allow characterizing each junction individually before any measurement of hybridization. We present three experiments: the individual current-voltage characteristics of the two junctions, gate voltage map of one junction and current-voltage of one junction for different gate values.

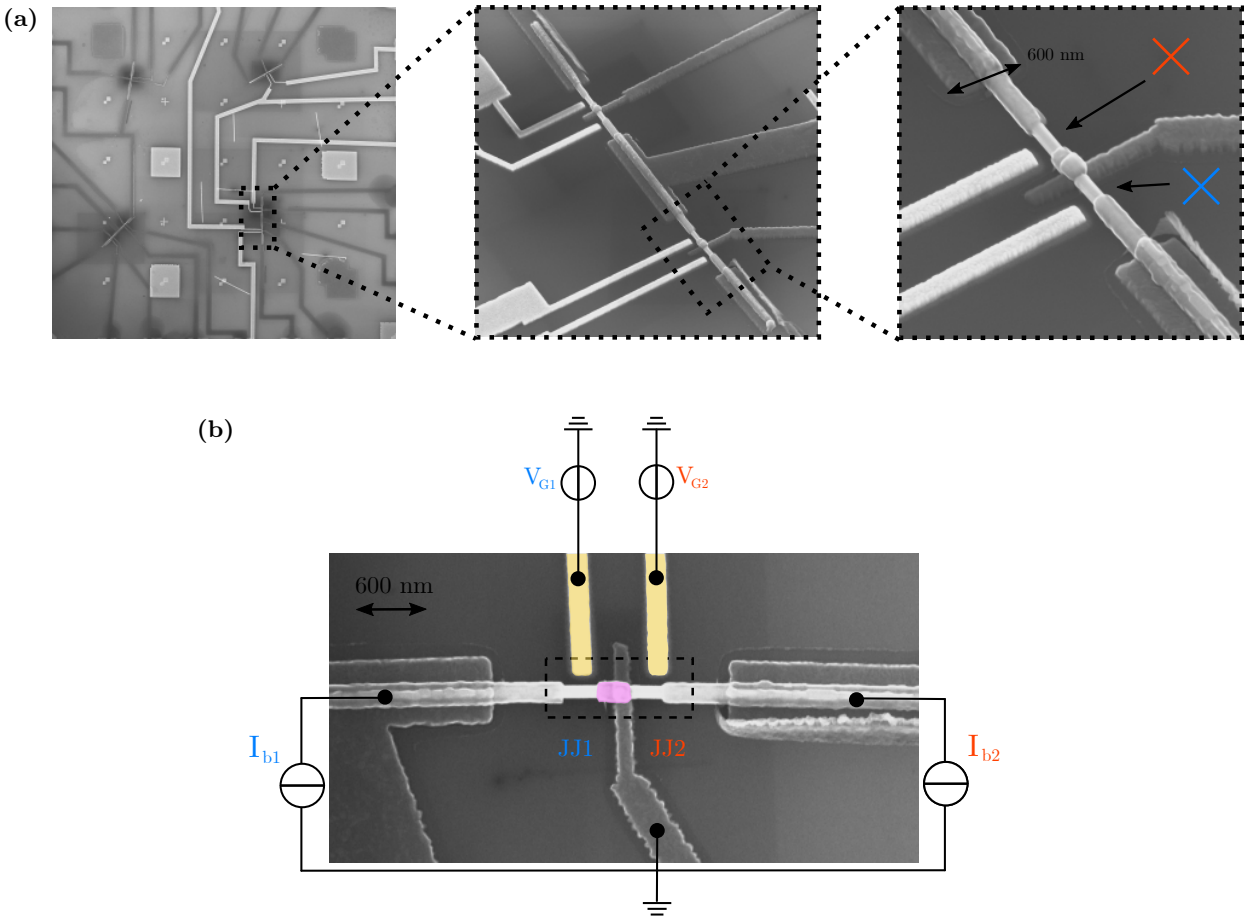

Figure 2.2: SEM images and design superposition of the sample AM14. (a) Three SEM pictures at different zoom levels. The photo on the left shows the sample with multiple nanowires and their corresponding connections. The middle picture is a zoom of the dotted black square on the left picture with a tilt. There are two Andreev molecules on a single nanowire. Each molecule has two gates which corresponds to the parallel white lines and two weak links. The image on the right is a focus on a single Andreev molecule from the middle picture. We can clearly see the two Josephson junctions with the weak links where the arrows are pointing. (b) A top-down view SEM image of an Andreev molecule with the superposition of the simplified circuit described in Fig 2.1. The pink part underlines the middle island, the AM and the yellow lines are the voltage gates closed to each weak link.

2.1.2.1 Individual current-voltage characteristics

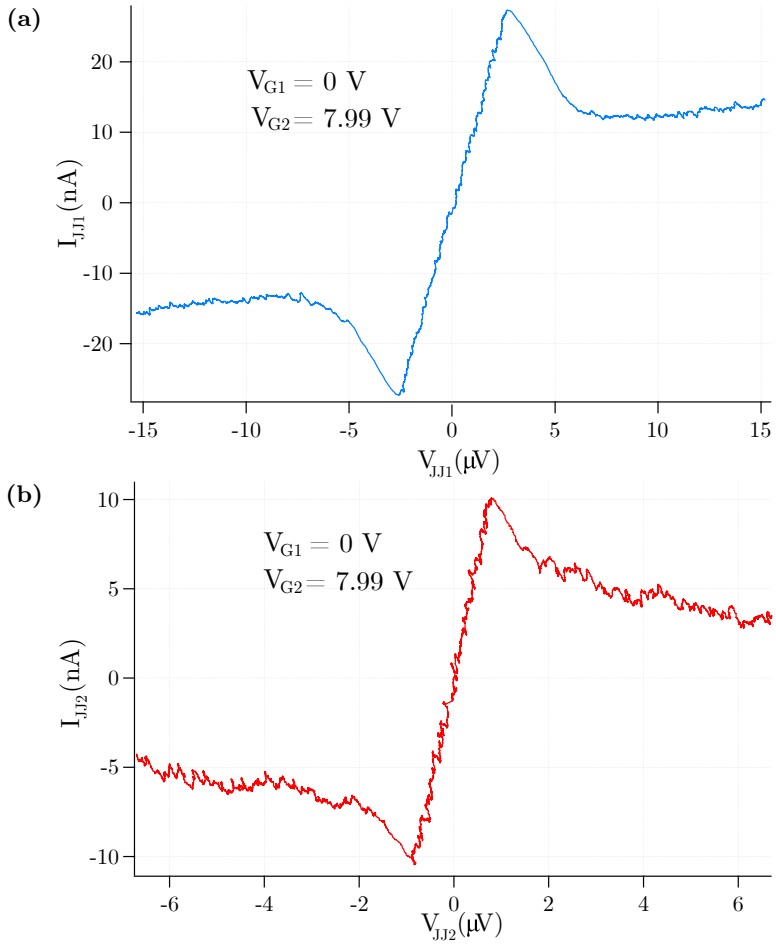

Figure 2.3: Current-voltage $I_J(V_J)$ characteristic of the two Josephson junctions (JJ) comprising the Andreev molecule at gate voltages $V_{G1} = 0\,\mathrm{V}$ and $V_{G2} = 7.99\,\mathrm{V}$. (a) Josephson Junction 1 (JJ1) IV with an equivalent resistance in series $R_{eq1} = 75.4\,\Omega$ and a switching current $I_{sw1} = 27\,\mathrm{nA}$ (b) Josephson Junction 2 (JJ2) IV with an equivalent resistance in series $R_{eq2} = 75\,\Omega$ and a switching current $I_{sw2} = 10\,\mathrm{nA}$.

When measuring the current-voltage characteristic of one junction, we set the bias current in the second junction to zero. The current of the junction is measured on a calibrated bias resistor in series with the junction and the voltage at the measurement point V_{JJ}. Despite being at zero current bias, the second junction may have non-zero phase due to hybridization when the junction separation is small (Eq. 1.19). An alternative would have been to configure the second junction in the pinch-off regime but due to crosstalk this would require adjusting both gate voltages.

Fig. 2.3 shows the current-voltage $I_J(V_J)$ of the two junctions (JJ1 and JJ2) for fixed gate voltages (V_{G1} and V_{G2}) which maximize the two critical currents. The measured average switching currents are $I_{sw1} = 27\,\mathrm{nA}$ and $I_{sw2} = 10\,\mathrm{nA}$.

One striking important of Fig. 2.3 is the slope of the critical current peaks indicating the presence of unwanted resistances in series with the junctions. These parasitic resistances are due to the use of gold lines on the chip as shown in Fig. 2.4(b). The gold leads were made before the fabrication, they help to define a zone to deposit the nanowires with the help of a micromanipulator. Without this zone finding the nanowires on the substrate would be difficult. The leads play the role of bonding pads at one end and contact pads for the aluminum leads of the Andreev molecule, at the other end. A revised circuit including these unanticipated resistances is presented in Fig. 2.4(a). Since there are three aluminum leads coming from the device which are connected to three gold lines, there are three parasitic resistances. The parasitic resistances R_{p1} and R_{p2} increase the effective value of the bias resistances R_{b1} and R_{b2}. However, the third parasitic R_{p3} is common to both junctions and results in a common voltage measured at V_{JJ1} and V_{JJ2}. If a current goes through JJ1, V_{JJ2} will be non-zero even if JJ2 has no current through it. This spurious signal needs to be accounted for by determining the values of the parasitic resistors and removing the unwanted contribution.

Three measurements are required to obtain the values of R_{p1}, R_{p2} and R_{p3}. The first measurement is a current-voltage characteric (IV) of JJ1 and JJ2 at zero current which gives us access to $R_{eq1} = R_{p1} + R_{p3} = 75.4\,\Omega$. The second measurement is the IV of JJ2 with JJ1 current which gives us access to $R_{eq2} = R_{p2} + R_{p3} = 75\,\Omega$. These measurements correspond to fitting the slopes in the IVs in Fig. 2.3. The last measurement is to bias both junctions in series with a current source which is not connected to the ground. To perform this measurement, with the sample in the fridge, the trick is to bias via the lines used for voltage probes V_{JJ1} and V_{JJ2}. The resistances of the measure lines $R_{lead1,2}$ in the cryostat are known from previous cooldowns and can be substracted from the measurements. In this configuration the current will pass through R_{lead1}, R_{p1}, JJ1, JJ2, R_{p2} and R_{lead2}, as defined in Fig. 2.4. By measuring the voltage drop across the voltage points V_{JJ1} and V_{JJ2} and substracting $R_{lead1,2}$, as defined in Fig. 2.4(a), we obtain $R_{eq3} = R_{p1} + R_{p2} = 82.8\,\Omega$. With these three equations the parasitic resistances are $R_{p1} = 41.6\,\Omega$, $R_{p2} = 41.2\,\Omega$ and $R_{p3} = 33.8\,\Omega$. These values are reasonable given the square resistance of gold leads (approximately $1\,\Omega/\square$) and their geometry corresponding to 350 squares.

Finally, the contribution of the parasitic resistances can be subtracted from our measurements of V_{JJ1} and V_{JJ2} and one can obtain independent IV characteristics for the two junctions. We underline that these corrections do not change the value of current in the junctions, it only changes the voltage V_{JJ1} and V_{JJ2}. The switching currents are still the same as the one shown in Fig. 2.3.

2.1.2.2 Gate voltage dependence

The gate electrodes allow tunning the junction conductance to obtain, in the ideal case, only a few highly-transmitted channels. In this section, we explore the influence of the gate voltages on the current-voltage characteristic of JJ2. For brevity we do not show similar measurements for JJ1.

Fig. 2.5(a) shows a map of the calculated differential conductance of JJ2 versus voltage V_{JJ2}, the y-axis, for different values of gate voltage V_{G2}, the x-axis. This map is obtained by measuring IVs at fixed V_{G2}. The same technique as described in Sec. 2.1.2.1 is used to measure the IVs. The differential conductance is obtained by numerical differentiation.

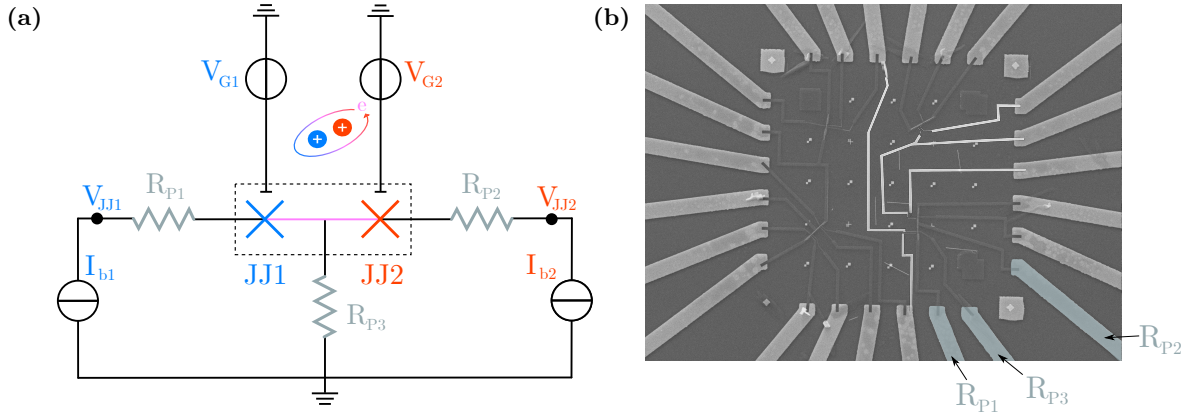

Figure 2.4: Parasitic resistances in device AM14. (a) Simplified circuit of AM14 with parasitic resistances. The main difference with the circuit presented in Fig. 2.1 is the presence of R_{p1}, R_{p2} and R_{p3}. Both measurements of V_{JJ1} and V_{JJ2} include a contribution from the total current flowing into the common resistor R_{p3}. To properly determine the voltage drop across the individual junction this contribution must be removed after determining the value of R_{p3}. Note that these resistances do not lead to corrections in the junction currents. (b) Modified SEM image of the sample AM14. The wide traces entering from outside the image and used to connect the sample to bonding pads are made of gold and have a low-temperature square resistance of approximately $1\,\Omega$. These parasitic resistances are colorized in blue and are connected by aluminum leads (dark gray) directly to the nanowire. These lines are connected to three aluminum leads connecting the nanowire directly to form the molecule.

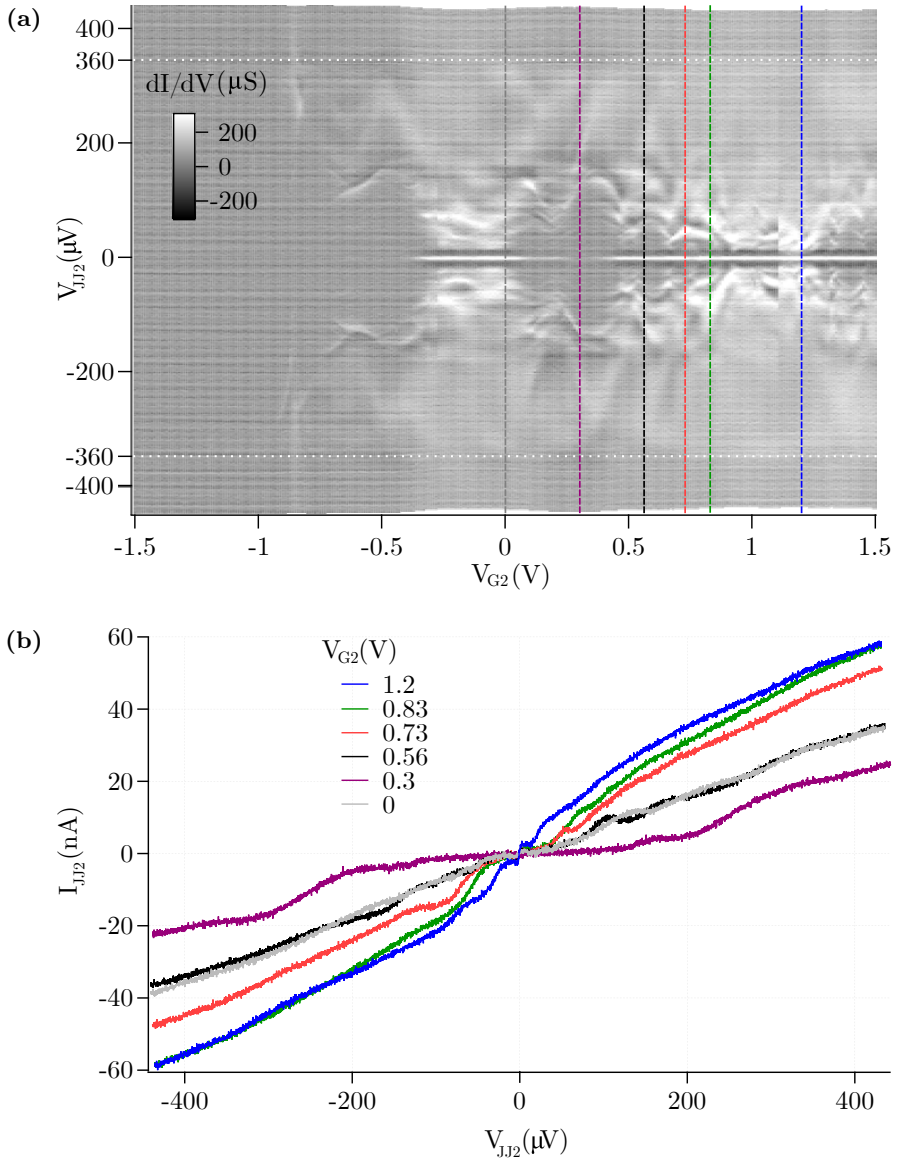

Figure 2.5: (a) Differential conductance map of JJ2. The electrical field effect in the exposed InAs nanowire results in modulation of the differential conductance and supercurrent as a function of gate voltage. The pinch off region is below $V_{G2} \approx -0.8\,\mathrm{V}$. Above $V_{G2} = 0.8\,\mathrm{V}$, the map shows complicated structure with high differential conductance indicative of multiple Andreev reflections as well as supercurrent peaks at $V_{JJ2} = 0\,\mathrm{V}$. (b) Current-voltage characteristic of JJ2 for different values of the gate voltage V_{G2}. The color corresponds to the cuts (dotted lines shown in (a)). The supercurrent peak and subgap structure are strongly influenced by the gate.

In Fig. 2.5(a), one can observe the quasiparticle branches which are the two zones for $|V_{JJ2}| > 360\,\mu V$. In this region, the conductance is reduced as expected. Another distinctive zone is the pinch-off region from $V_{G2} = -1.5\,V$ to $V_{G2} = -0.8\,V$ where the conductance of the junction is zero. Before pinch-off, from $V_{G2} = -0.8\,V$ to $V_{G2} = -0.3\,V$ peaks of conductance start to appear for $|V_{JJ2}| > 100\,\mu V$. Then from $V_{G2} = -0.8\,V$ to $V_{G2} = -0.3\,V$ the supercurrent current peak emerges along with MAR like features of high differential conductance for $|V_{JJ2}| < 100\,\mu V$. Going to higher gate voltage, there is a small high-resistance zone and then the supercurrent peak reemerges. Gate voltage regions with a bright supercurrent peak and significant differential conductance at sub-gap voltages are indicative of highly transmitting channels and are well suited for switching measurements of Andreev molecules.

2.1.2.3 Detection of high transmission features in the subgap

The effect of hybridized states in an Andreev molecule depends strongly on the transmission of the conduction channels in the junctions. A signature of systems with high transmission channels is the presence of subgap features, called Multiple Andreev States (MAR), in the IV of the junctions.

Fig. 2.5(b) represents six IVs of JJ2 taken at different values of V_{G2}, the corresponding slices are marked with dashed lines in Fig. 2.5(a). Among these different IVs, the switching current value of JJ2 is different and the greatest value is obtained when $V_{G2} = 1.2\,V$. One can also see kinks at different values of V_{JJ2} which look similar to MAR. However, using the same Monte-Carlo technique [64] as in the work of Goffman et al. [32], we were unable to fit the MAR-like features in the IVs. The difficulty in fitting the curves can be explained by the different size of the weak links. In the work of Goffman et al. [32], the junction is in the short limit regime where the length of the weak link is greater than the coherence length inside the weak link. However the junctions forming the device AM14 have an average length of 326 nm which is greater than the 230 nm separation of the junction in the device of Goffman et al. This increase of 42% could be sufficient to go from a short to a long limit regime. The Monte Carlo model is only valid for short weak links, possibly explaining the poor fit.

Even though the MAR fit is unsatisfactory, there is a large subgap current, the height of the supercurrent peak and the similarity of the current-voltage characteristics to those in [32] using the same nanowires indicate that the junctions have high transmissions.

From the control experiments, the two closely spaced junctions have some highly transmitted channels. Device AM14 combines the main ingredients to measure the hybridization of two Josephson junctions, although the weak links are in the long regime which is not described by the theory of Ch. 1. With this platform we will perform, in the following section, the measurements towards the characterization of an Andreev molecule.

2.1.3 Measurement of zero voltage region

One of the signatures of the hybridization of the junctions is the modulation of the switching current of one junction for different values of phase on the other junction (Sec. 1.1.4).

To detect any such modulation, we measured the extent of the zero voltage region for both junctions as a function of bias currents, shown in Fig. 2.6. Each point corresponds to a pair of

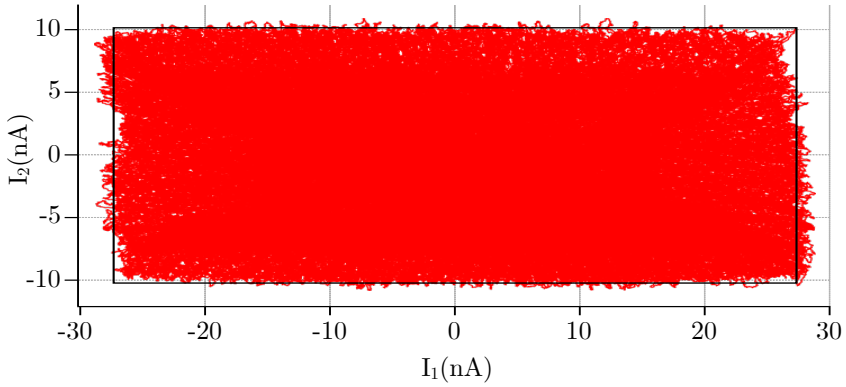

Figure 2.6: Zero voltage region of device AM14. Each red point in the graph corresponds to a pair of junction currents (I_1, I_2) on the supercurrent branches, such that both junction voltages are zero. The points of the graph defining the border of the quadrilateral are the switching points of the device. Any possible hybridization of the junctions would be characterized by a deformation from a rectangle describing two non-interacting junctions.

currents (I_1, I_2) for which both junctions are at zero voltage. In other words, in the red region, both junctions are on their supercurrent branches.

A standard switching measurement was not used to obtain the data of Fig. 2.6 due to a problem with the sample, as explained in Sec. 2.1.4. To acquire this data, we first apply a ramp to each junction, starting at zero current, that will make the junction switch for any value of supercurrent passing in the other junction. We also took care to adjust the ramp height such that the maximum current value passing through the junction during a ramp would always be its switching current. In order to acquire a full map of the switching current dependance of the two junctions, we perform a radial switching sweep. This radial sweep consists of applying a dephasing coefficient α on each ramp. For example, we apply a coefficient of $\cos(\alpha)$ for JJ1 and $\sin(\alpha)$ for JJ2 as shown in Fig. 2.7(a). To complete this radial sweep, we spanned α from 0 to 2π and, for each value of α, we ramped the junctions with the corresponding ramps, as shown in Fig. 2.7(b). Thereby, for each value of α, the junctions are ramped with the corresponding coefficient until one of them switches making the other junction switch as well. Current and voltage of the junctions are measured in the same way as the IVs in Sec. 2.1.2.1.

One remark on the graph, the junctions are biased in such a way that after they switch the junctions are in a state of non-zero voltage and current. These points of non-zero voltage are also visible on the graph. However, the voltage ramp is short enough such that the current, in these post-switch states, is always smaller than the switching current. It was not necessary to explicitly remove these points because they are in the middle of the red region and do not change the interpretation of the graph.

The most important points on the graph are at the border. They represent the last current configuration before switching from the supercurrent branch. If the two junctions are independent, the switching current of one junction does not depend on the current coming through the

other junction. This independence would result in the rectangular border denoted in black in Fig. 2.6 and Fig. 2.7(b). The positions of the sides of this rectangle are the mean switching currents of JJ1 and JJ2. However, as it can be seen in Fig. 2.6, the border defined by the measured points is not a clear quadrilateral due to noise.

One important reminder is that switching is a stochastic process, for each value of supercurrent there is an associated switching probability, which in the case of a bias current pulse will depend on the height and duration of the pulse. For low currents this value is close to zero but for currents close to the critical current this value goes up to one. In the case of our triangular ramps, we do not perform any statistics to extract the switching probability. So the border of the red region defines the switching current for one ramp realization which is different than the mean switching value resulting from multiple realization of the same ramp. Due to single ramp realization and noise we have a variability for each switching value which gives these loose edges.

However even with these poorly defined edges, we can see from the data in Fig. 2.6 that the top right and bottom left corners of the red region are set back from the corners of the black rectangle. On the contrary the upper left and bottom right corners are extend outward from the rectangle. These deformations could be interpreted as a sign of hybridization. All the more, the theory developed previously predicts deformation in the same direction as the one appearing in the data and an analysis of this will be developed in the next section. However the quantity of noise in the measurements does not permit drawing conclusions. The causes of unwanted noise and strategies to filter it are discussed in Sec. 2.1.3.1.

Lastly, with the noise, there are other unexpected features on the map which are not expected by the theory that confirm that it is worth interpreting the data with care. One of these features is the dip on the left border where $1\,\mathrm{nA} < I_2 < 4\,\mathrm{nA}$ which could be due to low frequency noise. A detailed explanation of the potential cause for this characteristic is in Sec. 2.1.3.1. Another feature is the relative flatness of the horizontal edges compare to the vertical ones. And to finish in the top left and bottom right corner only a part of the zero voltage region extends outward the black rectangle, instead of the whole region, which is different than what the theory seems to predict.

2.1.3.1 Analysis

The hallmark of hybridization of junctions is a deformation of the switching rectangle in Fig. 2.6. Quantifying this deviation is key to confirming hybridization. For weak hybridization, we expect one side of the rectangle will develop a small tilt, deviating from horizontal or vertical. Therefore it is sufficient to fit only the right side of the zero voltage region. Ramping the bias current on only one junction allows optimizing the measurement and reducing the noise as much as possible. Data acquired this way for device AM14 is shown in Fig 2.8(a). The map (Fig 2.8(a)) plots the voltage on JJ1 as a function of time (x-axis) and the trace number (y-axis). For each trace, the current through JJ1 is ramped up from negative values. The bias current applied to JJ2 is fixed during the ramp, and is stepped up from approximately $-30\,\mathrm{nA}$ at trace 0 to approximately $30\,\mathrm{nA}$ at trace 256. The switching of JJ1 is identified by the jump in voltage around 95 ms. To determine the border an edge detection algorithm was used, giving the red line. From the time at which JJ1 switches, we determine its switching current.

Fig. 2.8(b) shows the fit of the right side of the zero voltage region of Fig. 2.6. The deviation

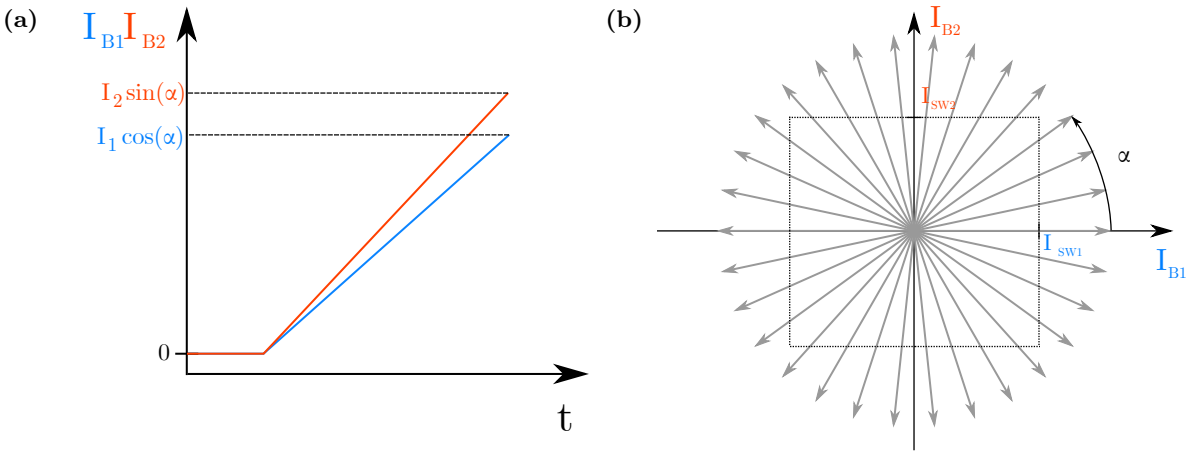

Figure 2.7: Current biasing protocol to acquire a critical current graph I_1 vs I_2. (a) Current bias for JJ1, $I_{B1}(\alpha)$, and JJ2, $I_{B2}(\alpha)$, as a function of time. The current bias is ramped up to a value that guarantees switching for any value of α. The current plateau at the beginning serves as a reference point to correct drift. (b) Resulting sweep profiles as a function of α and zero voltage region for uncoupled junctions (dashed rectangle).

is of $1.4\% \pm 0.3$. Although the slope is small, it is statistically significant, and barring low-frequency noise, systematic error, or an artefact due to other causes, hints at a possible Andreev molecule. To confirm such a detection one needs to perform other measurements such as the one described in Sec. 3.2-3.

In the last chapter, we developed a theory relating the switching current variation of the junctions to the hybridization of their ABS. We focused on the dependence of one junction's switching current on the phase of the other junction (Fig. 1.9(b)) and the junction separation. However in this experiment we measure the switching current variation of one junction for different values of bias current applied to the other junction at fixed separation.

In a current biasing experiment, Fig. 2.9, there are two possible current configurations. The first one is the anti-parallel current state. Given our convention, positive current through each junction means that both currents will go to ground and are in opposite directions. In the anti-parallel current configuration shown in Fig. 2.9(b), the phase differences of the junctions are of the same sign $\delta_2 = \delta_1$. The second configuration is the parallel current state represented in Fig. 2.9(a), where the measured current values are of opposite sign, $I_1 = -I_2$.

Returning to the data of Fig. 2.6, the most noticeable deviation is at the corners. Due to symmetry, opposite corners are expected to have similar characteristics, either stretching out of the boundary of the black rectangle (top left and bottom right), or contracting inwards (top right and bottom left). In these regions, the device has the same current configuration, either parallel (top left and bottom right) or anti-parallel (top right and bottom left), which leads to the same deviation from the rectangle.

Comparing these variations with the numerical simulation from Fig. 2.10(a), showing the

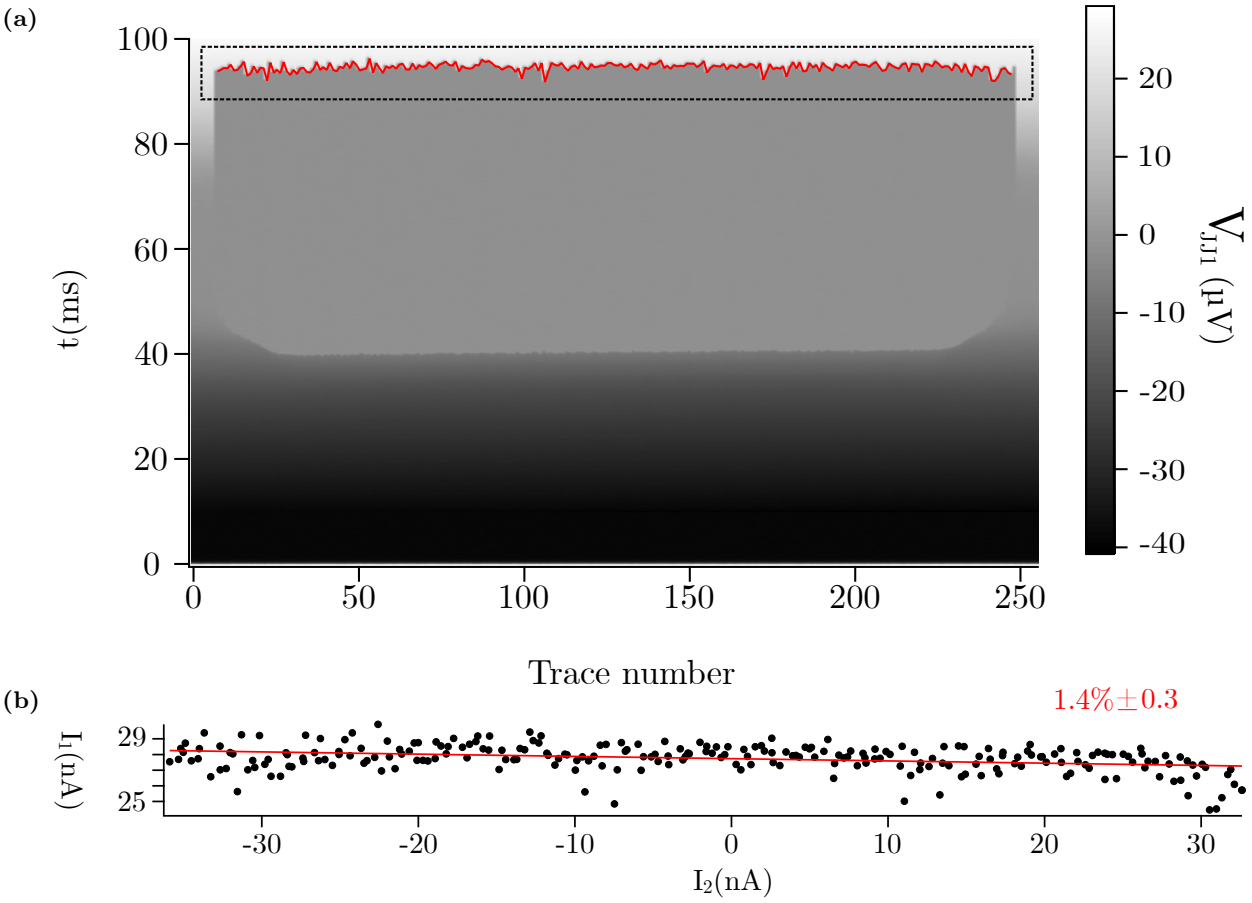

Figure 2.8: (a) Switching map of JJ1. Each trace records the voltage V_{JJ1} as the current bias I_{b1} is ramped up. The bias current applied to JJ2 is fixed during each trace, and is stepped up as the trace number increases. The red line is obtained with an edge detection algorithm and shows when JJ1 switches. (b) Extracted plot of switching currents I_1 vs I_2, with a fit of slope $1.4\% \pm 0.3$ indicating a possible hybridization of the junctions.

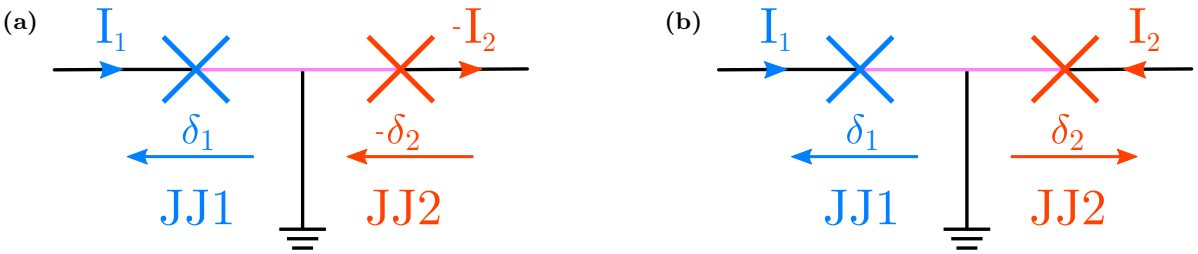

Figure 2.9: The parallel (a) and anti-parallel (b) current configurations of an Andreev molecule. The parallel configuration corresponds to dEC and results in an enhanced total supercurrent $|I_1| + |I_2|$ as compared to dCAR (anti-parallel configuration).

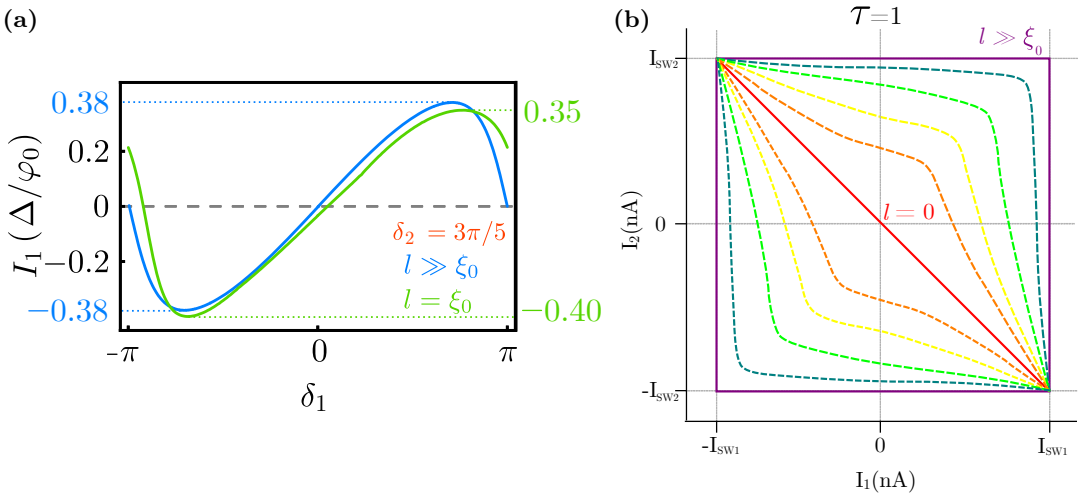

Figure 2.10: (a) Supercurrent variation of JJ1 as a function of its phase difference δ_1 for a fixed value of phase δ_2 on JJ2. The hybridized ($l = \xi_0$) and unhybridized ($l \gg \xi_0$) configurations are shown. The important feature to notice is the shift of the extrema when $\delta_1 = \delta_2$ or $\delta_1 = -\delta_2$. For $\delta_1 = \delta_2$ (dCAR) the supercurrent value is reduced, and this the opposite for $\delta_1 = -\delta_2$ (dEC). (b) Sketch of the boundary of the zero voltage region for $\tau = 1$ and varying separation l. This theoretical prediction for the deformation of the zero voltage region can be compared to the data in Fig. 2.6 and 2.8(a). The full lines are the analytical solution of Eq. 1.12 for the cases $l = 0$ and $l \gg \xi_0$ ($\tau = 1$).

dependence of I_1 on δ_2 at two different separations (reproduced from Fig. 1.8(a,d)), a similar signature is retrieved. The blue line is the current of JJ1 for values of δ_1 ranging from $-\pi$ to π and for a fixed value of $\delta_2 = 3\pi/5$ when the two junctions are in a non-hybridized configuration $l \gg \xi_0$. The magnitude of the positive and negative critical currents, 0.38, are identical. These extrema represent the switching current for a unique phase configuration ($\delta_1 \approx \pm 3\pi/4$, $\delta_2 = 3\pi/5$) when $l \gg \xi_0$. Comparing it to the green line which represents the same current but for hybridized junctions where $l = \xi_0$, one notices a slight shift towards the right and a distortion of the curve. The magnitude of the positive critical current has decreased to 0.35 whereas the negative one has increased to 0.40.

The reduction in the positive critical current is 7.9%. The experimental data of Fig. 2.8(b) and the small slope there is may be related to the theoretically predicted reduction in the critical current for this configuration. The 7.9 % should correspond to the contraction of the red region in the upper right corner when the currents have the same sign (Fig. 2.8(b)). In this area of the graph, we are in the anti-parallel current configuration which is also coherent with the sign of the phase in Fig. 2.10(a). Indeed, the decrease happened for values of δ_1 between 0 and π when the phases have the same signs ($\delta_2 = 3\pi/5$) hence the currents have opposite direction as shown in Fig. 2.9.

As developed in the theory, the phase or current configuration is also associated with the microscopic mechanism at play in hybridization. When the phases of the junctions have the same sign, the dominating mechanism is dCAR. This can be understood since dCAR corresponds to the double splitting of a Cooper pair from the central superconducting island to the island on the sides. The resulting current directions in the junctions are in opposite direction.

Regarding the magnitude of the negative critical current in Fig. 2.10(a) a similar analysis can be performed. The minimum value of switching has decreased by 5.2 %. In Fig. 2.6, this decrease corresponds to extending the zero-voltage boundary beyond the black rectangle in the top left region when the measured current have opposite signs. The decrease happens when δ_1 is between $-\pi$ and 0, and since $\delta_2 = 3\pi/5$, the phases have opposite signs. So the phase and current configuration correspond to the parallel current configuration. The corresponding microscopic mechanism at play is dEC, the dEC is the double tunneling of a Cooper pair through the two junctions and therefore the currents are in the same direction.

With these two regimes corresponding to parallel and anti-parallel current directions, one can compare the coupling of ABS to ferromagnetism. If one considers that the magnitude of the Josephson energy is proportional to the critical current I_c, the highest critical current and thus the lowest energy is reached when the currents and the phases of both junctions are aligned. This is similar to ferromagnet which reaches its lowest energy when its magnetic moments are aligned.

It is possible to expand on Fig. 2.10(a) and plot the theoretically expected zero voltage region, similar to what is shown experimentally in Fig. 2.6, for an ideal symmetric Andreev molecule with perfect transmission. The region is sketched in Fig. 2.10(b) as a function of the junction separation. This graph has been obtained by analyzing the solutions for the Andreev molecule in the case of perfect transmission (Eq. 1.12). For $l \to \infty$, one gets $\epsilon = \pm \cos \frac{\delta_{1(2)}}{2}$ which gives two independent values of I_1 and I_2. The corresponding configuration is the violet square. For $l \to 0$, one gets $\epsilon = \pm \cos\left(\frac{\delta_1 - \delta_2}{2}\right)$ which give $I_1 = -I_2$. These solutions appear in red

on the graph. For intermediate values of separation, the zero voltage region must interpolate between these two extremes. We sketch these solutions by starting from the diagonal ($l = 0$) and expanding it until it reaches the square ($l \to \infty$). It is important to note that the dashed lines in Fig. 2.10(b) are drawings and a further analysis is necessary to solve numerically these intermediate states. A missing feature from this graph is the deformation at the top-left and bottom-right corner. This absence is explained by the lack of dCAR processes at perfect transmission, which inhibits changes in the critical current for the anti-parallel current configuration. Further theoretical work could elucidate the full border of the zero-voltage region for different values of l and τ is pending.

To finish this analysis, we address the defects of the measurement. Using Fig. 2.10 we have explained the main features of the zero voltage region and related them to theory. The fluctuations in the switching current due to noise are of several nanoamperes, corresponding to roughly $5 - 10\%$ of the mean switching current. The lack of better data, including a real switching current measurement, is due to the fact that the device failed due to improper handling. Better measurements were planned before breakage. Unfortunately, the slow acquisition time of the data presented in Fig. 2.7 and Fig. 2.8a made them susceptible to low frequency noise. We suspect this noise to be at the origin of the deep pocket on the left side border between $I_2 = 1\,\mathrm{nA}$ and $I_2 = 4\,\mathrm{nA}$.

Sources of systematic error also need to be considered, such as the role of heating. Due to the parasitic on-chip resistors which are in series with the junctions, one could expect that at higher bias currents the effective electronic temperature will be higher. This could lower the mean switching current of one junction when the applied bias current on the other junction is high, thereby also deforming the zero-voltage region, effectively rounding out all corners equally. However due to the small critical currents, small values of the parasitic resistors, and their adequately large volume, this heating effect is negligible for device AM14. Other sources of systematic error may remain unidentified.

One last identified contribution to the noise in the data is the unbalanced measurement design. One technique to reduce noise in a measurement is to measure the sample in a balanced design where a device under test (DUT), with two pins, is connected such that the impedance to ground is the same for the two pins. In such a design, electromagnetic interference which couples equally to both lines (common mode noise) will be canceled at the DUT. However since Andreev molecules are three-terminal devices, it is not clear how to create a balanced circuit which allows measuring both junctions simultaneously.

2.1.4 Conclusions and perspectives

The experiments described above show possible signatures of hybridization between two Josephson junctions. However, the data is not conclusive. Our observations concur with the theory but they are not complete enough to be fully convincing. A small variation of the switching current of one junction as a function of the current applied to the other junction has been observed. Furthermore, these variations can be partially understood with the theory developed in Chap. 1 and interpreted in terms of the two microscopic phenomena, dEC and dCAR.

However further measurements are compulsory to confirm that these variations are related to an Andreev molecule physics. Unfortunately device failure made it impossible to carry out

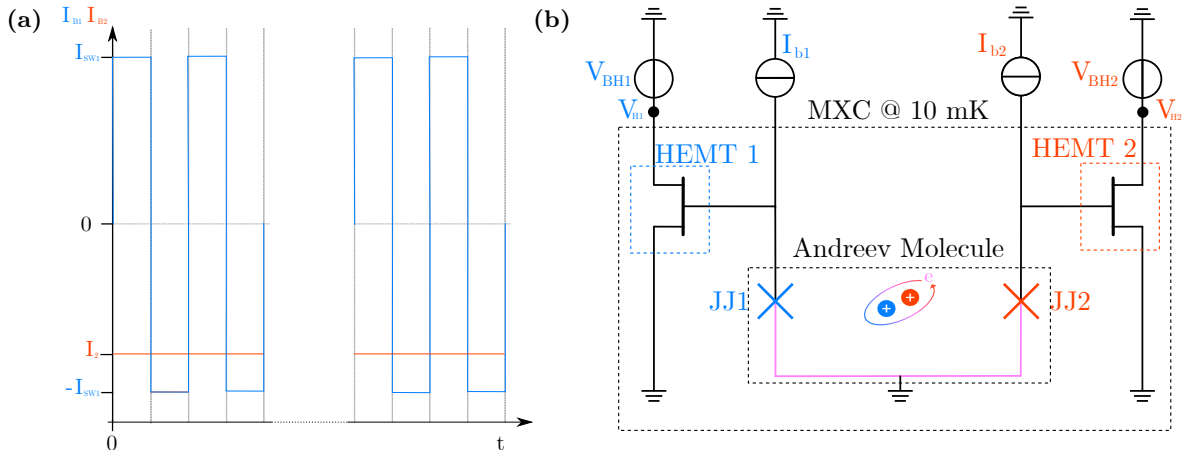

Figure 2.11: (a) Bias protocol to avoid low frequency noise on I vs I graph. By alternating two opposite values on the I vs I, we can do (b) Simplified circuit using HEMT to measure voltage on JJs. There is a HEMT for each junction. The voltage probes V_{JJ1} and V_{JJ2} in Fig. 2.4(a) are replaced with V_{H1} and V_{H2}. The junction is amplified by the HEMT and measured at its terminals.

these measurements. New samples are crucial performing new measurements and confirming these encouraging preliminary results.

Learning from our experience with device AM14 some improvements can easily be made. Regarding the device itself and the fabrication process, one of the easiest improvements is to remove the gold leads to avoid the parasitic resistances and avoid potential errors due to calibration of their values. Also, as explained in Chap. 2 and reinforced by the findings of Kornich et al.[57, 61], the distance between the junctions needs to be the smallest possible. A strategy to fabricate a device with a smaller middle island was underway and is described in Sec. 3.1.

Concerning improvements to the measurement, a proper protocol. Proper switching experiments, with better statistics, needs to be performed. The protocol consists of sending a large number of current pulses of constant value in one junction, JJ1 for example, with a fixed current bias in the other junction, JJ2. From the whole train of pulses sent to JJ1 only a certain percentage would make it switch. This value corresponds to the percentage of switching for a certain height of the pulse [65] and a fixed current on JJ2. The height of pulse which gives a percentage of 50 % is usually defined as the switching current of JJ1 for a fixed value of JJ2. Repeating this protocol for different values of current in JJ2 would give a result similar to Fig. 2.10b with proper switching values. Also since the hallmark of an Andreev molecule is the deformation of the zero voltage region at the corners, four precise measurements, or even only two, could tell if there is a variation. One does not need to span a whole region or a full side.

Lastly, using a switching pulse sequence like the one represented in Fig. 2.11(a) could help to reduce, or drift, in the measurements. This setup aims to determine the boundaries of the zero voltage region in a different fashion. At fixed bias current on JJ2, the switching pulse sequence

for JJ1 alternates between positive and negative polarity. The difference between the measured positive switching probability and the negative switching probability quantifies the deformation of the zero voltage region. Effectively we obtain the difference between opposite sides of the zero voltage region as shown in Fig. 2.10b. This difference is maximal at the corners of the rectangle. This protocol is insensitive to drift since low frequency noise will equally affect the positive and negative switching probabilities.

Another improvement can be made regarding the design of the measurement circuit. Apart from the low noise frequency, two main causes of the noise are the unbalanced circuit and the inadequate filtering of the DC lines used to measure the voltage of the junctions. A possible solution replacing the direct voltage measurement lines with an indirect measurement using a HEMT. A HEMT plays the role of a DC amplifier and isolator. With a HEMT, the voltage of the junction will not be measured by connecting an external amplifier via cabling to the points V_{JJ1} or V_{JJ2}, as in Fig. 2.4(a), but it will be measured through the voltage drop across the gate of a cryogenic HEMT close to the sample at V_{H1} and V_{H2}, as shown in the simplified circuit Fig. 2.11(b). Although this design is still unbalanced, the isolation provided by the HEMTs decouples the noise incident from the measurement lines connecting outside the cryostat. The closer the HEMT is located to the device, the less low frequency external noise will be picked up. Since we are working at cryogenic temperature, the HEMTs need to be working at this temperature. Also the amplification of the signal provided by the HEMT will improve the signal-to-noise ratio.

After the measurement of AM14, we developed such a HEMT-based measurement setup. The cryogenic HEMTs provided by Y. Jin are designed to work at liquid helium temperature [66] so it was necessary to adapt the HEMT biasing protocol for millikelvin temperatures. We succeeded in getting a working HEMT at 10 mK with an amplification of around 10 with a noise of less than $1\,\mathrm{nV}/\sqrt{\mathrm{Hz}}$ at 100 Hz. Unfortunately, we did not have time to measure an Andreev molecule with HEMTs during this thesis. We developed the protocol between the measurement of the AM14 device and we did not get a new working device. However our protocol was tested on single Josephson junction placed in a device similar to an Andreev molecule device. Our protocol and results can be found in Sec. 3.3

2.2 Current bias switching measurement at fixed phase

The experiment described in the previous section gives only probes the zero voltage region of the Andreev molecule. The boundaries of this region is complicated to compute since the phases of the two junctions are not simply related to the bias currents. A simpler measurement would be to control the phase of one junction and measure the switching current of the other junction.

The simplified circuit design is presented in Fig. 2.12(a). The design is very similar to the one presented for the current bias switching measurement in Fig. 2.1. The Andreev molecule corresponds to the junctions JJ1 and JJ2 inside the dotted box with a common superconducting terminal shown in pink. JJ1 is inside a superconducting loop, as shown in the hypothetical SEM image Fig. 2.12(b), which permits defining the phase difference δ_1 of JJ1 as $\delta_1 = 2\pi\Phi_1/\Phi_0$, with n an integer and Φ_0 the flux quantum. JJ2 is current biased by I_{b2} and its voltage is

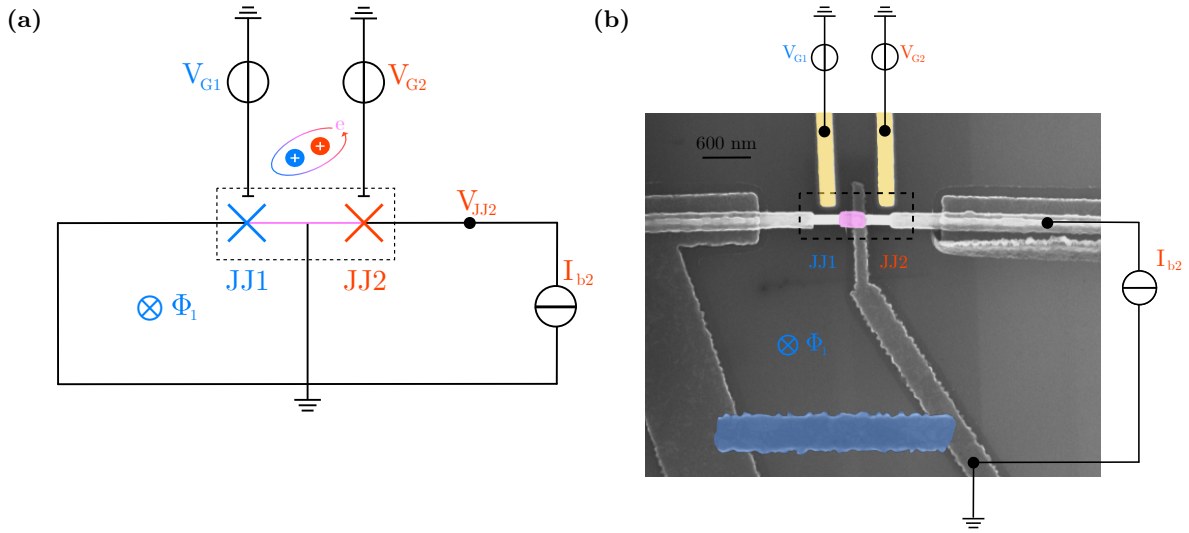

Figure 2.12: (a) Simplified phase bias switching circuit, corresponding to the circuit of Fig. 2.1 with an additional shunt across JJ1 which forms a superconducting loop. The magnetic flux Φ_1 inside the loop is generated by an external electromagnet and allows tunning the phase $\delta_1 = 2\pi\Phi_1/\Phi_0$ of JJ1 from 0 to 2π while measuring the switching current of JJ2. (b) Modified SEM image of a hypothetical sample with a superconducting shunt (blue) corresponding to the circuit in (a). The only difference with the design used for the current bias switching measurement is the addition of the Al trace in blue defining a superconducting loop. In practice the superconducting shunt would be further away from JJ1 to define a bigger loop and thereby reduce the magnetic field necessary for phase biasing.

probed at V_{JJ2}. As usual the conductance of both junctions can be tuned by gate voltages V_{G1} and V_{G2}.

One of the difficulties of this setup is that it is impossible to characterize the conductance of the shunted junction. The gate voltage must be adjusted blindly to move out of the pinch-off region where there is no hybridization. However, the main advantage of this design is its similarity with the current bias switching design. This permits measuring an Andreev molecule first using the design Fig. 2.2(b). Then a single lithography and deposition step allow adding an Al patch to the design and shunting one of the junctions in a superconducting loop, as shown in Fig 2.12(b). This two-step technique is a good solution to fully characterize the junction before it is shunted.

One must ensure that the blue aluminum shunt in Fig. 2.12(b) is properly connected and that the junctions are not harmed or significantly modified during the second fabrication cycle.

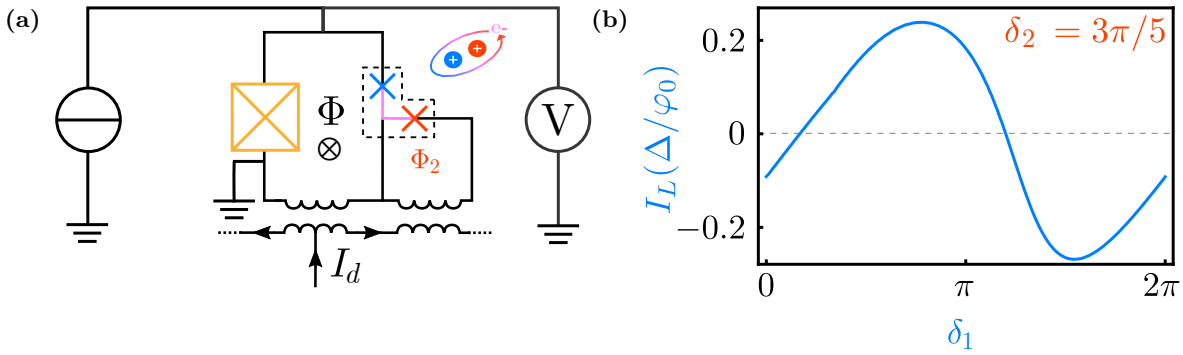

Figure 2.13: (a) Setup for measurement of the current-phase relation of a device hosting Andreev molecules. The Andreev molecule is made of the blue and red junctions. By shunting the blue junction with a tunnel junction (yellow) of larger critical current, it is possible to extract the current-phase relation of the blue junction as a function of the red junction's phase $\delta_2 = 2\pi\Phi_2/\Phi_0$. The big yellow junction is not part of the Andreev molecule and serves as probing device. The fluxes in both loops are controlled independently by a global field for the junction in blue and by a local field generated by a gradiometric loop for the junction in red. (b) An example of the expected current-phase relation for $\delta_2 = 3\pi/5$ which should rise from the setup in (a). The presence of non-zero supercurrent at $\delta_1 = 0$ is indicative of a φ-junction.

With this design by tuning the phase on one of the junctions we can control the strength of hybridization, as shown in Fig. 1.7 and obtaining current-voltage characteristics of one junction as a function of the fixed phase on the other (Fig. 1.9b).

2.3 Phase bias switching measurement

To explore further the non-local current-phase relation of Andreev molecules, one needs to be able to phase bias both junctions. Accessing both phases allows demonstrating a φ-junction

behavior, corresponding to a junction developing a supercurrent without a phase drop across it.

In this proposal the existence of a non-local current-phase relation can be directly determined by measurements of the switching current. This type of experiment has been performed on superconducting atomic contacts [67], graphene [68] and carbon nanotubes [69]. In this circuit, shown in Fig. 2.13(a), a large Josephson junction of critical current $I_0 \gg I_{LC}$ is wired in parallel with the first junction hosting the Andreev molecule, forming an asymmetric SQUID. The second junction is shorted in a loop enclosing an applied magnetic flux Φ_2 such that its superconducting phase difference is $\delta_2 = \varphi_2$. A differential flux line combined with a global applied flux $\Phi = \varphi_0\varphi$ allows independent tuning of δ_1 and δ_2. Due to the asymmetry, the SQUID critical current $I_{SQ}(\varphi, \varphi_2)$ is essentially given by that of the large junction, effectively at a phase difference of $\pi/2$, modulated by the supercurrent of the first junction, $I_{SQ}(\varphi, \varphi_2) \approx I_0 + I_1(\varphi - \pi/2, \varphi_2)$, where flux quantization constrains $\delta_1 = \varphi - \pi/2$. By sending current pulses or ramps and measuring the switching of the SQUID to a non-zero voltage state, one can extract the current-phase relation $I_1(\varphi - \pi/2, \varphi_2)$ and demonstrate that there is a non-local component that depends on δ_2, as shown in Fig. 2.14(b).

2.4 Josephson spectroscopy

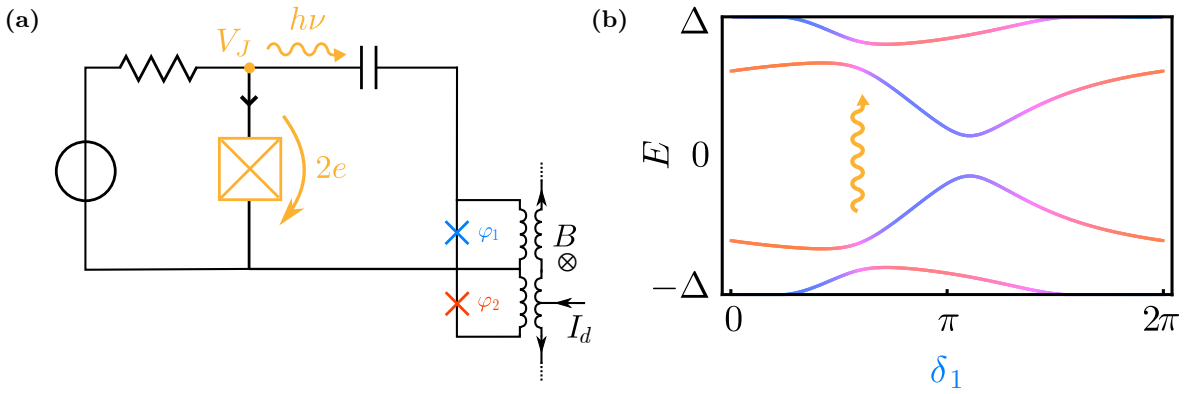

Figure 2.14: (a) Setup to perform Josephson spectroscopy of an Andreev molecule in a Josephson device with two junctions (black crosses connected to red, magenta and blue wires forming two loops). The Andreev molecule is made of the blue and red junctions. The big yellow junction is not part of the Andreev molecule and serves as probing device. A magnetic field B induces a flux Φ in both of the loops of the device. For independent control of φ_1 and φ_2, a gradiometric line with control current I_d (on the right) induces an additional flux coupled only to the first junction loop. (b) Andreev molecule spectra with a figurative representation of an excitation from the ground state to the excited state.

In Fig. 2.14(a), we propose a setup to perform spectroscopy of an Andreev molecule in a similar manner to the spectroscopy of an Andreev "atom" in a superconducting atomic contact

[28].

A large tunnel Josephson junction (yellow) is simultaneously used as an on-chip microwave source and detector. When a voltage V_J is applied across this spectroscopy junction, Cooper pairs tunnel back and forth by emitting and absorbing photons of energy $h\nu = 2eV_J/h$. As long as all emitted photons are reabsorbed, the net current I_J is zero. However if the Andreev molecule, which is capacitively coupled to the spectrometer, absorbs photons (Fig. 2.14(b) at a rate Γ, a non-zero DC current will flow of magnitude $I_J = 2e\Gamma$. The current-voltage characteristic, $I_J(V_J)$ of the spectrometer junction will thus have peaks at voltages $E_T/2e$ corresponding to the transition energies E_T of the Andreev molecule. The magnetic field B and gradiometric control current I_d allow independently tuning the phases δ_1 and δ_2. A full measurement $I_J(V_J, B, I_d)$ would allow reconstructing the spectra of Fig. 1.8. In addition, assuming that the loops have the same area A and their geometric inductances are negligible, by fixing $I_d = 0$ and varying B so that $\delta_1 = -\delta_2 = BA/\varphi_0$ one can directly probe the dEC transitions. Likewise by fixing $B = 0$ and varying I_d such that $\delta_1 = \delta_2 \propto I_d$ one can probe dCAR transitions and thereby obtain the hybridization spectrum of Fig. 1.7. Josephson spectroscopy is well suited for detecting Andreev molecules, as E_T may be comparable to Δ/h (90 GHz for aluminum), well within the spectrometer bandwidth. Conventional microwave spectroscopy using a resonator coupled to the Andreev molecule is convenient for small hybridization gaps less than 18 GHz, for example when transmissions are low or the separation is large. Further theoretical work is necessary to determine the selection rules for the transitions. By design, as only the first junction is inside the spectrometer high-frequency loop, emitted photons cannot directly excite the second junction. This implies that only vertical transitions in Fig. 1.6 are possible. However as the symmetry of the BdG Hamiltonian is different for dEC and dCAR, there is no evidence that the selection rules are similar. Since the conventional ABS Hamiltonian has the same symmetry as the dEC Hamiltonian, at least the transitions at $\delta_2 = -\delta_1$ should be optically active.

3 Experimental techniques

This chapter focuses primarily on the most time-consuming part of the thesis: fabrication of devices. It includes the design of devices and their fabrication, explaining the choices that were made based on physical constraints and the problems that were faced. We also outline potential improvements to the whole process. Second we describe the setup used for DC measurements and detail the circuit from the sample holder to oscilloscope. We also explain our results on the use of HEMTs as DC cryogenic amplifiers and how they isolate samples from noise. These HEMTs are a promising tool to perform low noise DC measurements in dry cryostats where low-frequency noise due to vibrations is ubiquitous.

3.1 Sample design and fabrication process

In this section, we are going to present the extended fabrication process of device AM14, from motivation and design to detailed fabrication steps. The design attempts to satisfy the constraints dictated by theory and inevitably includes compromises.

3.1.1 Sample design and fabrication strategy

The objective is to obtain a device which hosts an Andreev molecule and which can be measured with DC electronic transport techniques. The two Josephson junctions in the molecule must be closely spaced and contain a few conduction channels of high transmission. The distance separating the junctions must be on the order of the coherence length of the superconductor used. For the conduction channels of the weak links, the goal is to have approximately ten well-transmitted channels.

With these constraints, the most promising technological platform is InAs-Al nanowires. These nanowires are recent technology coming from an impressive work of Peter Krogstrup's group [25]; they are made of a semiconducting core of InAs covered by an epitaxial superconducting Al shell, as shown in Fig. 3.1(a). Thanks to the epitaxial growth process the nanowires have a good interface between the core and shell, as shown in Fig. 3.1(b). The end result is that Josephson junction fabricated from these nanowires have a well-defined superconducting gap. Furthermore with aluminum as the superconducting shell, the nanowires are amenable to conventional superconducting circuit fabrication techniques. The aluminum has a dirty superconducting coherence length of about 150 nm, which makes fabrication of junctions with smaller spacing technically feasible. Furthermore, this platform allows tuning the number of channels and their transparency with side gates.

We were able to access to this technological platform thanks to a close collaboration with Groupe Quantronique (or "the Quantronics group") which was willing to share their knowledge with us. The Quantum Flux Lab and Groupe Quantronique were already working together on other research projects.

I would like to deeply thank Groupe Quantronique without which the fabrication of this sample would have taken much longer.

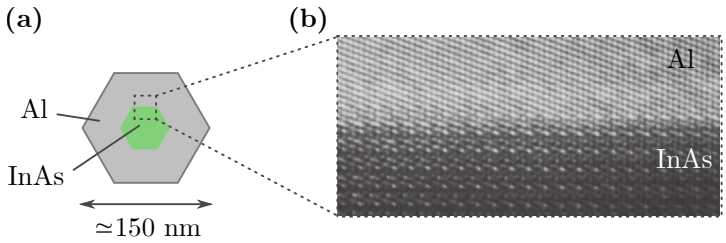

Figure 3.1: Figures modified from [25]. (a) Schematic of the cross-section of epitaxial full-shell nanowire with InAs core (green) and Al shell (gray). (b) Transmission electron micrograph of epitaxial N/S interface along the cut in (a)

To make Josephson junctions with InAs-Al nanowires, one needs to etch the Al shell around the core to create a weak link. After this step one connects electrodes to the junctions and deposits side gates.. The final device should look like the schematic in Fig. 3.2. It consists of two Josephson junctions separated by a distance $l \approx \xi_0$ and with side gates addressing each junction.

To obtain this device from raw nanowires it is necessary to perform multiple optical and electronic lithography steps, many thin film depositions and one wet etch. Among these steps, the two most difficult ones are the wet etch to define the two weak links and forming the contact to the nanowires. The short duration of the wet etch makes the weak link length susceptible to variations. Contacting the nanowire is delicate due to the precision required to align to the middle island ($l \approx 150\,\mathrm{nm}$) of the freshly etched nanowire.

With these challenges in mind, we increase the chances to obtain a working sample by fabricating multiple samples in parallel. Multiple nanowires are deposited on each chip, and multiple Andreew molecules are fabricated on each nanowire.

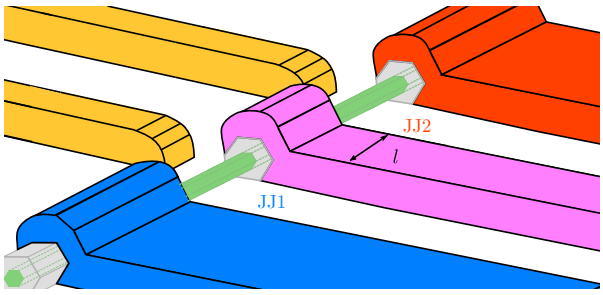

Figure 3.2: Schematic of Andreev molecule device. The sample is made of two junctions JJ1 and JJ2. JJ1, located between the blue and pink terminals, is in contact with the Al shell (gray) of the InAs-Al nanowire and has a side gate (yellow) to tune the carrier density of the exposed InAs core of the nanowire (green). JJ2 is located between the pink and red terminals. The separation between junctions is l, corresponding to the width of the middle terminal (pink).

3.1.2 Preparation of the wafer

In this section, we describe how we prepared a bare wafer to use it as a support for the future circuit. The wafer used is intrinsic floating-zone silicon (100) with a 150 nm capping layer of silica (SiO_2) and is diced into $1\,cm^2 \times 1\,cm^2$ chips. Multiple nanowires are deposited onto a prefabricated $90\,\mu m^2 \times 90\,\mu m^2$ drop zone on each chip. The drop zone is surrounded by leads which will serve to make electrical contact to the nanowires and which have bonding pads at the far end.

The lithography and thin-film metal deposition techniques used in the following steps are described in detail in Fig. 3.5-3.8. To fabricate the leads we employ a photoresist stencil mask consisting of a bilayer of S1813/LOR5B and pattern the design using optical lithography at a dose of approximately $200\,mJ/cm^2$. After development, we deposit a 3 nm thin film of titanium and 50 nm of gold. The resulting pattern, after lift-off, is shown in Fig. 3.3.

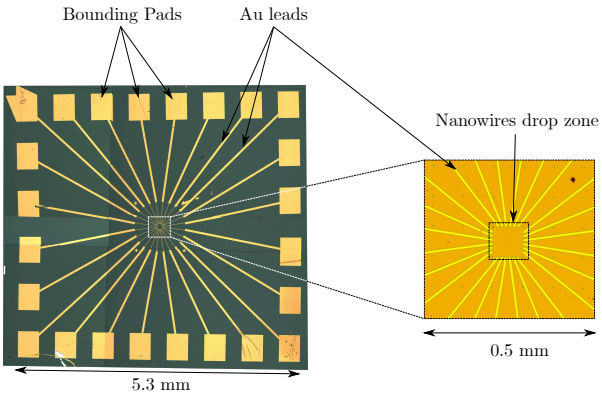

Figure 3.3: Two micrographs show the bond pads, the leads and the nanowire drop zone. The Au(50 nm)/ Ti(3 nm) metallization is patterned with optical lithography.

After this step, we add alignment markers, in the form of evenly spaced crosses, to the drop zone. These marks allow aligning the electrodes with the nanowires. Patterning the sub-micron crosses requires the use of electronic lithography. The chip is first cleaned in an asher using an oxygen plasma. The cleaning parameters are 38 cc/min flow of oxygen at a pressure of 0.2 mbar and an RF power of 50 W for a duration of 2 min. After cleaning the chip was coated with a bilayer of PMMA/MAA as described in Sec. 3.1.2.1. The design, shown in Fig. 3.4(a), was patterned with a 30 kV scanning electron microscope at a dose of $420\,\mu C/cm^2$. After development, we obtain the stencil shown in Fig. 3.4(b). We then perform the same Au/Ti metal deposition as before. The resulting pattern, after lift-off, is shown in Fig. 3.4(c).

3.1.2.1 Lithography techniques

Optical lithography was performed with a Microtech Laserwriter LW405B capable of 1 µm resolution. Electronic lithography was performed at an accelerating voltage of 30 kV in a Philips XL30 scanning electron microscope (SEM) equipped with Raith Elphy Quantum lithography software.

Prior to exposure, the chip is coated with the proper resist. For optical lithography, we used a bilayer of S1813/LOR5B. The top layer, S1813, is a positive photo resist from Shipley. The

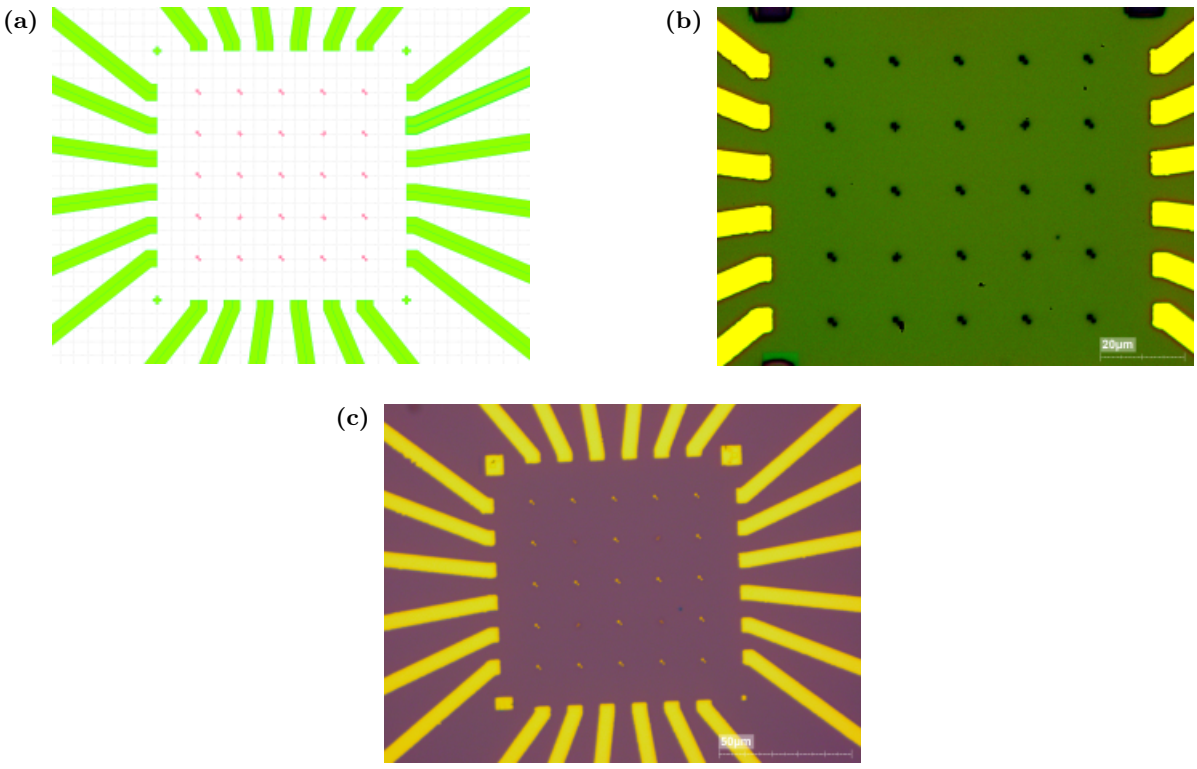

Figure 3.4: Representation of the alignement crosses necessary for further steps. (a) Alignement crosses in the gds viewer. (b) Micrograph (500x) of the stencil of alignement crosses. (c) Micrograph (200x) of the metal deposition of alignement crosses.

bottom layer, LOR5B, is a resist based on polydimethylglutarimide from Microchem which is removed chemically by the developer solution. For electronic lithography, we use either a single resist layer of polymethyl-methacrylate (PMMA) or a bilayer stack of PMMA/MMA (methyl-methacrylate). The chips are spin-coated with the following recipes.

Bilayer for optical lithography Pour LOR5B on chip and spin at 1000 rpm for 60 s to obtain 850 nm thin film. Bake on hotplate at 200 °C for 5 min and spray cool by flowing nitrogen gas on backside of chip. Pour S1813 and spin at 3000 rpm for 45 s. Bake at 115 °C for 1 min. The resulting bilayer is 1.5 µm thick.

Monolayer for electronic lithography Prebake the chip at 175 °C for 5 min. Pour PMMA on chip and spin at 6000 rpm for 60 s to obtain 290 nm thin film. Baked on hotplate at 180 °C for 90 s.

Bilayer for electronic lithography Prebake the chip at 175 °C for 5 min. Pour MMA on chip and spin at 6000 rpm for 60 s for a 390 nm thin film. Bake chip on hotplate at 180 °C for 90 s After cooling with nitrogen flow, pour PMMA, spin at 6000 rpm for 60 s and bake at 180 °C for 90 s. The resulting bilayer is 680 µm thick.

The chip is then loaded in the lithography system and the designed pattern exposed point-by-point. Parameters such as step size, dose, and beam intensity are optimized for each lithography. In electronic lithography, the undercut layer is electro-active and is exposed with a lower dose than the main design, as shown in Fig. 3.6. In optical lithography, the chemically active undercut layer is not affected by photo exposition.

After exposition, the resist is developed. For optical lithography, the chip is dipped in a MF319 solution (Dow) for 30 s, rinsed with water to stop development, and dried under nitrogen flow. For electronic lithography, we develop the resist in methyl-isobutyl ketone (MIBK) diluted 1:3 by volume in isopropanol (IPA) for 45 s. We then transfer the chip to a beaker full of IPA, rinse it for 15 s to stop development, and dry with nitrogen. We finally obtain the desired pattern as shown in Fig. 3.7.

3.1.2.2 Metal deposition

All the metal deposition steps were performed with two similar electron beam evaporators from Plassys (MEB 550S). The evaporator has two vacuum chambers: the main chamber, at 10^{-8} mbar, containing the electron gun and crucibles; and the load lock chamber, pumped to 10^{-7} mbar, containing the sample chip and process accessories including an ion-mill etcher and a liquid nitrogen cooling system for the sample holder.

All evaporation recipes start with ion etching. This dry physical etch is used to either clean the sample surface or to remove oxides. Metal can then be deposited on the exposed regions.

Metal is sublimated from the crucibles as a result of heating by electron bombardment from the electron gun. In this recipe, we only use titanium, gold and aluminum, which are typically evaporated at a rate between 0.5 nm/s and 1 nm/s.

After metal deposition, the load lock chamber is vented and the chip is removed. The resist stencil is removed in a lift-off process where the the chip is placed in a bath of heated acetone at 65 °C for 30 min. Fig. 3.8 summarizes the process.

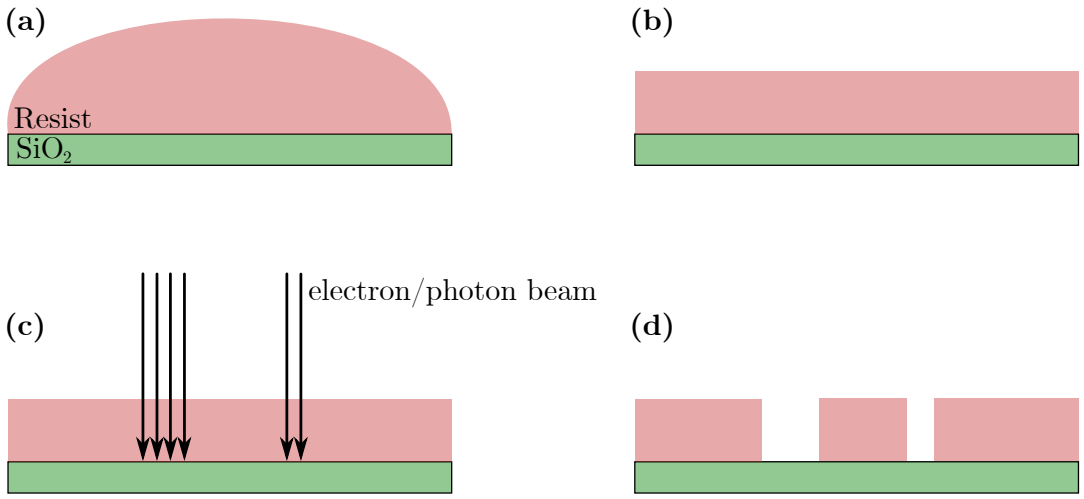

Figure 3.5: All the stages of lithography with a single layer. (a) Chip after resist deposition. (b) Chip after spinning and baking. (c) Exposure of the chip. (d) Chip after development. The exposed resist has been dissolved.

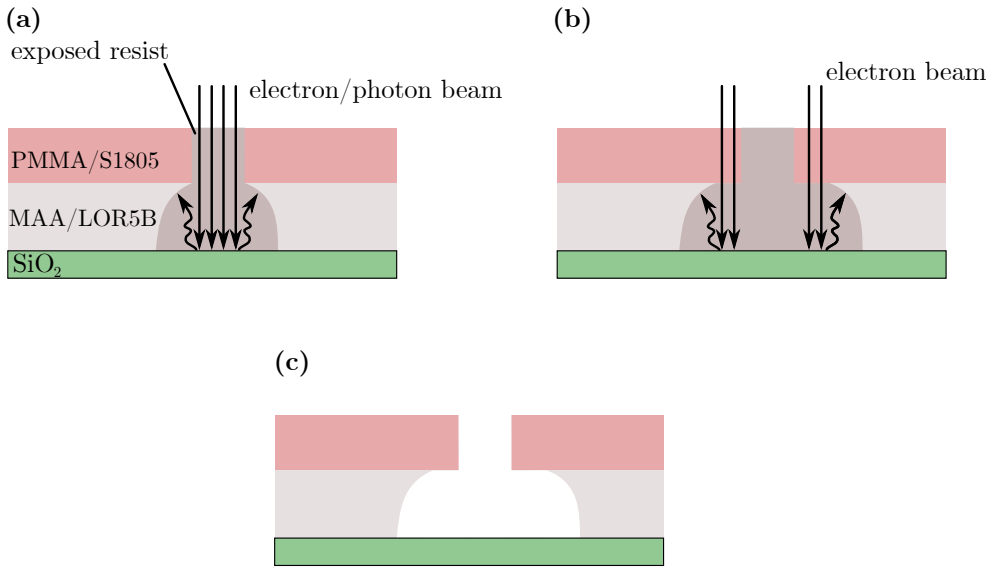

Figure 3.6: Lithography of a bilayer stack. (a) Chip exposition. (b) Exposition of the undercut at a lower dose than (a) only necessary for the PMMA/MAA stack. (c) Chip after development. For the photosensitive resist the undercut is due to inherent chemical sensitivity to the developer. For the electro-sensitive resist the undercut is due to exposure in (b).

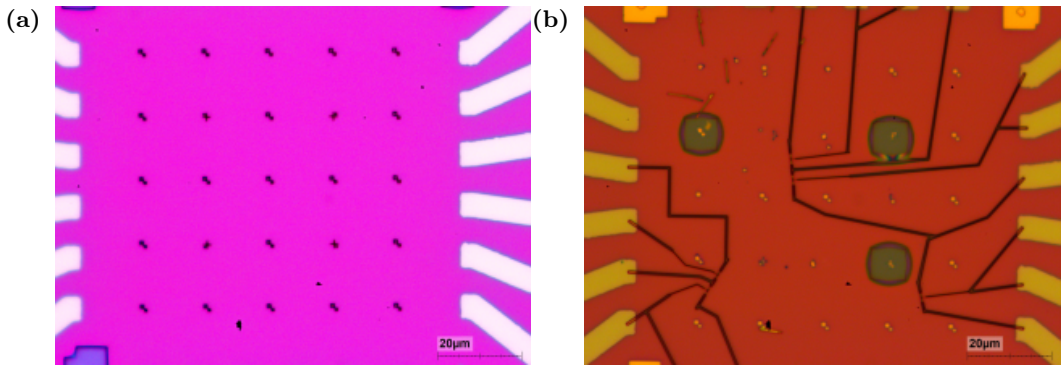

Figure 3.7: Examples of lithography steps. (a) Lithography steps of the alignment marks. (b) Lithography steps of contact leads.

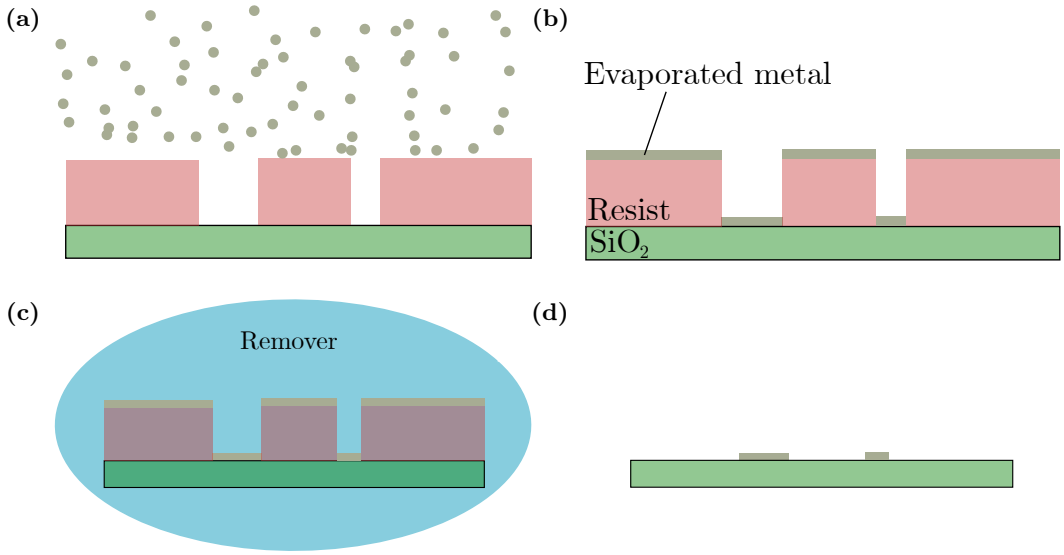

Figure 3.8: Metal deposition process. (a) Evaporation of metal. (b) Metal deposited on chip covering resist and patterned trenches. (c) Chip immersed in remover. (d) Chip after lift-off with desired metallization pattern.

3.1.3 Nanowire deposition

Once the chip is prepared with the intermediate lines and the alignement crosses, we clean the chip in the asher with the same parameters as before. After cleaning the chip is baked at 140 °C for 5 min to remove water. Then we coat the chip with AL1805 which corresponds to S1805 resist from Shipley diluted in volume concentration 1:33 with propylene glycol monomethyl ether acetatat from Dow and filtered through 0.2 µm filter paper. This coating is an adhesion layer to avoid the peeling of the PMMA resist during a future etching step due bad adhesion between PMMA and silica. The resist is then spun at 6000 rpm for 45 s and baked at 110 °C for 3 min. The resulting 4 nm underlayer avoids having the nanowire in direct contact with the chip and helps in etching its aluminum shell. To spread the nanowires we use a micromanipulation station home assembled. This station is composed of a digital microscope VHX950F from Keyence and a micromanipulator TransferMan4R from Eppendorf. The tips used to manipulate the nanowires are made in titanium from American Probe & Technologies, Inc, with a radius of curvature of 100 nm (model : #72X-G2/01). They are placed in a tip holder design and made in house which allows, contrary to commercial options, a rotation along the tip axis. This feature is of great importance to manipulate and place the nanowires on the chip. From a forest of nanowires, shown in Fig. 3.9(a), one nanowire is collected onto the tip of the micromanipulator, as shown in Fig. 3.9(b), and is transferred to the drop zone on the chip 3.9(c). Once the nanowire is deposited, it can be delicately pushed around and positioned with the micromanipulator tip. This operation is repeated for each nanowire. Fig. 3.9(c) shows the sample AM14 with ten nanowires placed inside the drop zone.

3.1.4 Nanowire etching

In this step we etch parts of the aluminum shell of a nanowire. The exposed regions of the nanowire will be the weak links of the Josephson junctions. The distance between the two regions is the junction separation and needs to be short to obtain an Andreev molecule. On the other hand if this aluminum island is too short it will be difficult to make electrical contact with the central lead.

To remove the Al shell, we first coat the nanowires on the chip with a single layer of PMMA as described in 3.1.2.1. Optical micrographs of the as-deposited nanowires serve as a reference to align the lithography pattern, show in Fig. 3.10(a), consisting of narrow perpendicular cuts across the nanowires which define the junctions. After alignment, the design is exposed with electron beam lithography and developed with the aligement crosses pattern recipe (3.1.2). Fig. 3.10(b) shows the chips after exposure and development. Before the chemical etch, the surface of the exposed aluminum shell is cleaned by ashing with the above-mentioned parameters.

The layer of AL1805 is dissolved during development, creating a 4 nm gap between the nanowire and the wafer. Exposed regions of nanowire are therefore suspended above the wafer. This gap helps to evenly etch the aluminum shell, as the etchant may otherwise fail to pass under the nanowire.

A beaker of aluminum etchant, Transine type-d, and a beaker of DI are placed in a mary bath of water at 50 °C. We plunge the chip first in the Al etchant for 12 s, then hot DI water for 15 s, and finally in room-temperature DI water. The chip is then plunged in a beaker of

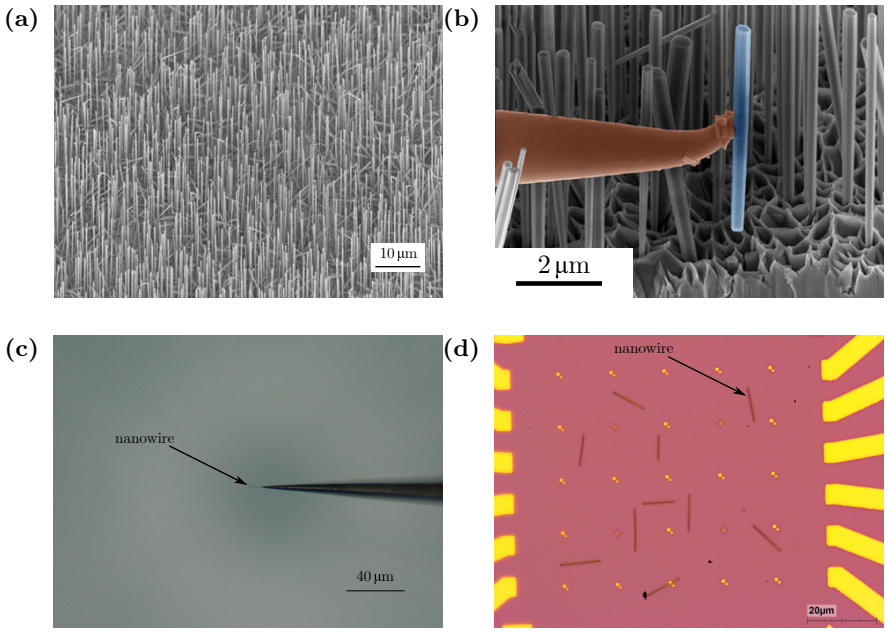

Figure 3.9: (a) SEM image of a forest of III-V semiconductor nanowires standing, as grown, on a silicon substrate from the Technische Universitaet Muenchen [70]. The nanowires we used are different but also grew in forest like the one on the image. (b) SEM image from [71] with false colored single nanowire (blue) being removed with a micromanipualtor from a forest of GaN nanowires. The nanowires we used are different but the extraction technique is similar. (c) Micrograph (1000x) of InAs-Al at the end of a micromanipulator. (d) Micrograph (500x) of InAs-Al deposited on AM14 chip.

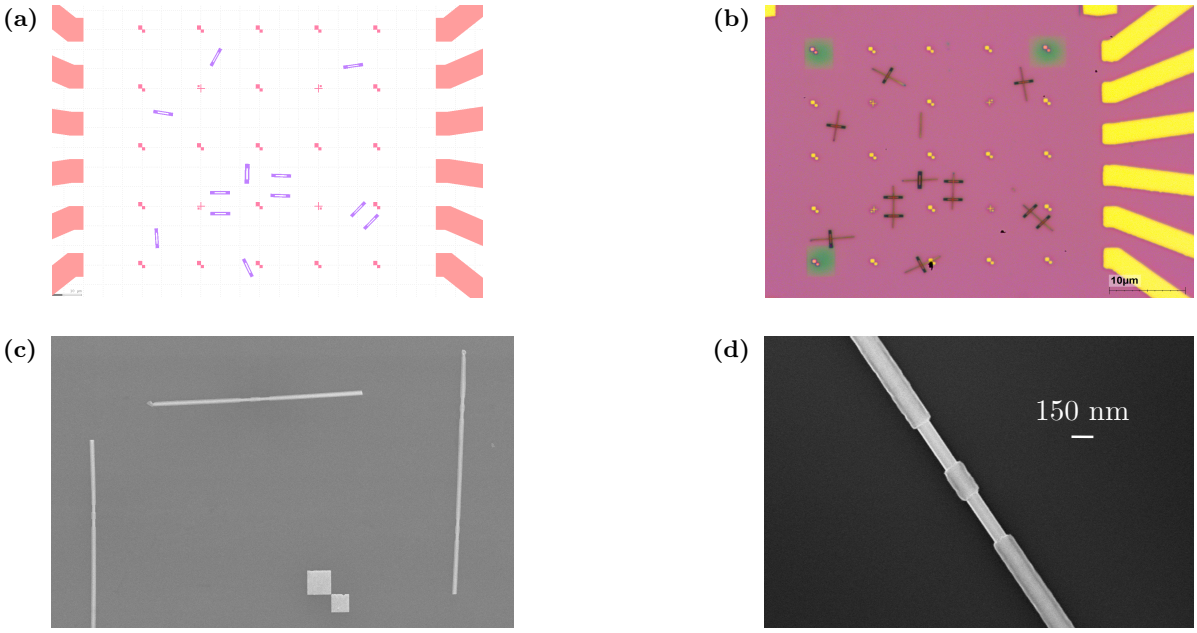

Figure 3.10: Etching of the nanowires (a) Lithography pattern of the trenches crossing the nanowires. (b) Microscope image zoom x500 of AM14 chip after development, the black lines crossing the nanowires are the trenches. (c) SEM image of three nanowires after etching. We can see the variations on the etching process on a same chip. (d) SEM image of succeeded etch. The two exposed parts and the middle island have clear edges.

acetone at 60 °C to dissolve the PMMA mask. Fig. 3.10(c)-(d) shows an SEM image of the nanowire after the etching, where we can see the InAs nanowire core in two places for each sample.

This step produces unreliable results since the etching process is extremely sensitive to temperature and time. Furthermore, wetting of the Al etchant inside the resist trenches is not always reproducible. As we can see in the SEM image not all nanowires are etched equally. By etching multiple junctions on multiple nanowires, we can select the best ones for an Andreev molecule.

3.1.5 Contacting nanowires with metallic leads

Using SEM images taken after the etch step, it is possible to align the pattern with the electrical connections to the nanowires. The design of AM14 in Fig. 3.11(a) shows contacts to six potential Andreev molecules on four different nanowires.

Before electron-beam lithography, the chip is cleaned with the asher and coated with a bilayer of PMMA/MAA. Fig. 3.11(b) shows microscope images of the sample AM14 after these steps.

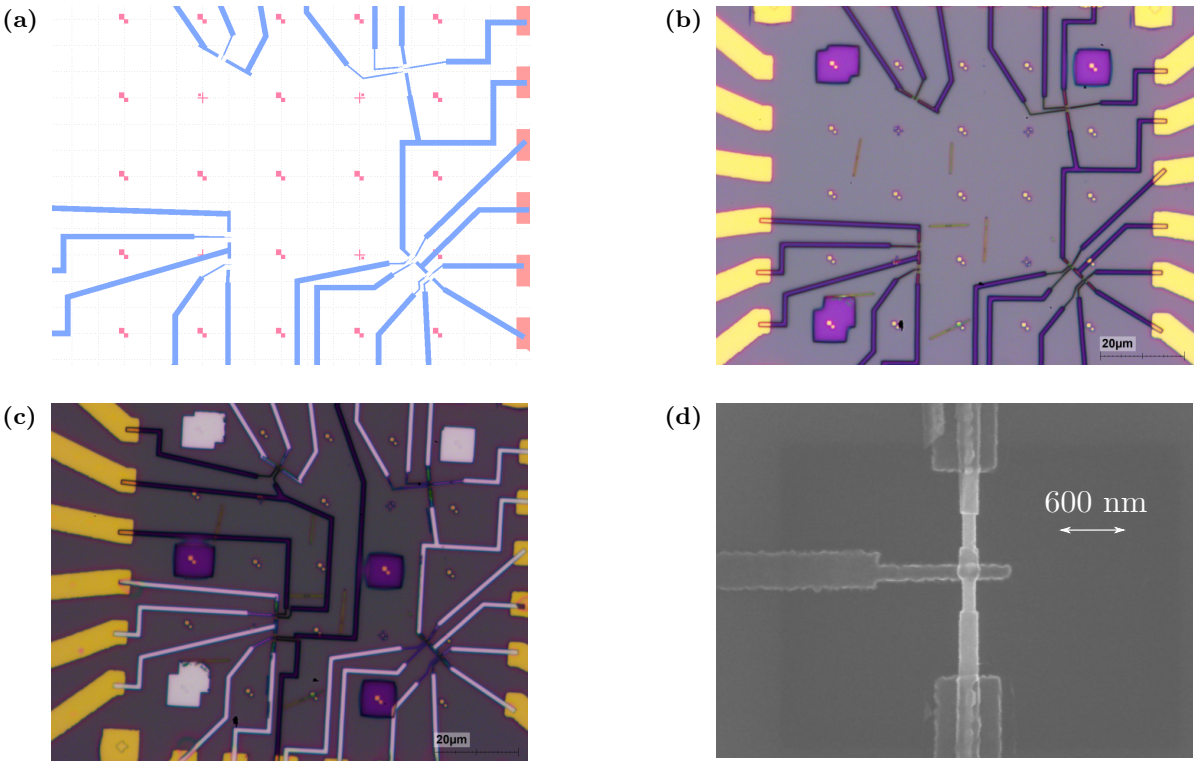

Figure 3.11: Metal deposition of contact leads (a) Patterns of the contact leads defined in Elphy Quantum. (b) Optical micrograph (500x) of AM14 chip after development. The stencil represents contacting leads to six Andreev molecules. Some molecules also have gate leads. (c) Optical micrograph (500x) of AM14 chip after metal deposition and development of gates, showing aluminum contact leads. (d) SEM image of AM14 before gate deposition.

To electrically contact the nanowires, it is necessary to first etch the thin aluminum oxide layer on the aluminum shell before evaporating aluminum. The Al shell oxidizes in air and would result in a large series resistance if not removed. A dry argon ion etch performed in the electron-beam evaporator physically removes this oxide layer. This step is performed before depositing the aluminum leads and without breaking vacuum, avoiding additional oxidation. The etch consists of height 5 s cycles of ion irradiation, with 40 s pauses in between at 500 eV and 130 mA. The pauses are necessary to avoid excessive heating which would damage the resist and distort the lithography pattern. We discuss solutions to improve reliability of this step using different techniques in Sec. 3.1.7. After ion milling, we evaporate 120 nm of Al and then proceed to lift-off. Fig. 3.11(c) shows a microscope image of the sample. Even if the overall result is satisfying, we can see in Fig. 3.11 that there is a shift of approximately 100 nm between the pattern and the actual circuit, as shown in Fig. 3.12. This shift is due to the precision limit of the lithograph. Some strategies to reduce the offset are presented in Sec.3.1.7.

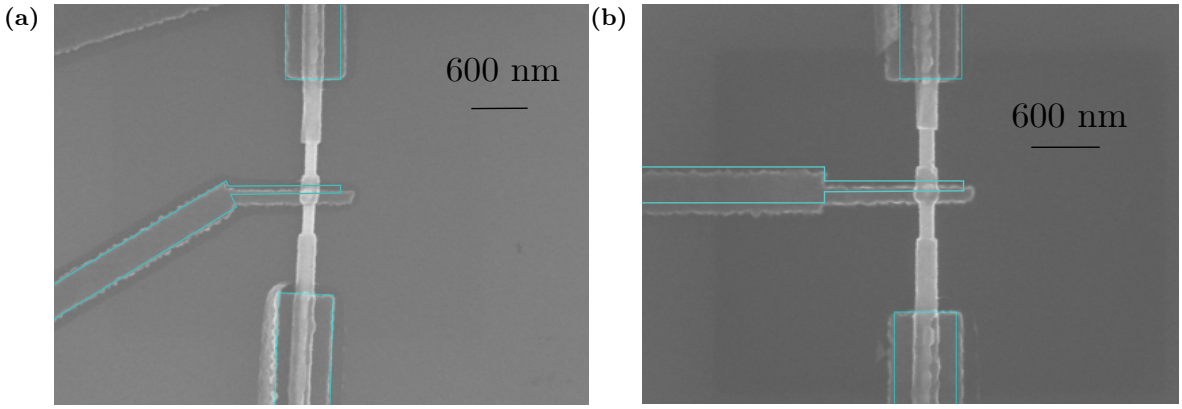

Figure 3.12: SEM images of devices showing the shift between the desired pattern and the metal deposition. (a) AM14 device before gate deposition. (b) AM15 device before gate deposition.

One can remark that some potential molecules have their gate electrodes patterned at this stage. This was an attempt to reduce the number of fabrication steps, but the patterns are distorted by ion milling and short the junctions, as shown in Fig. 3.13.

3.1.6 Gating and shunting nanowires

The last step is adding side gates and protective shorts between intermediate leads. The gates tune the conduction channels of the weak links and the shorts mitigate the risk of electrostatic discharge which could damage the junctions. The chip is cleaned, spin-coated, and then loaded for electron-beam lithography as above. The small gate electrodes are patterned with a dose of 390 µC/cm^2 and small spot size (1) whereas the larger shorts are patterned at 700 µC/cm^2 and spot size 5.

After development, the resulting stencil for the gates is shown in Fig.3.11(c). There are six gates for three potential Andreev molecules. A bilayer of Au(150 nm) /Ti(3 nm) is then deposited in the electron-beam evaporator. Fig. 3.14 is an electron micrograph of the chip, showing device AM14 whose measurement is presented in Chap. 2.

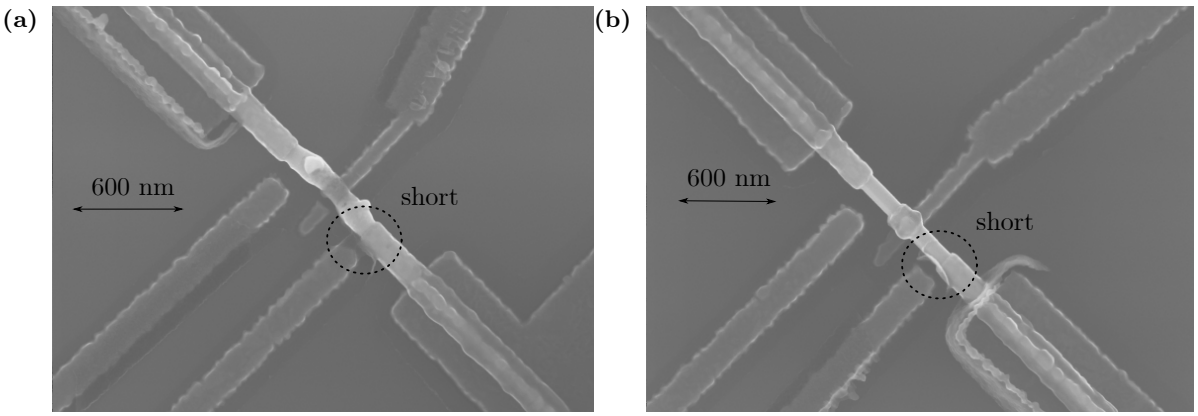

Figure 3.13: SEM images of samples with aluminum gates shorting the junctions. (a) Sample with a short and a middle island damaged during ion milling. (b) Sample with shorts.

3.1.7 Potential improvements

The recipe presented is long and difficult. There are six lithography steps, one wet etch and one dry etch. We managed to produce a working device, AM14, with junction length and separation of 330 nm. Although these dimensions are promising, the experiments showed that even smaller lengths are needed, particularly for the middle island. Since the device broke in the fridge, we started developing a new recipe to reach smaller dimensions. The potential advantages of this recipe are presented in this section.

The goal was to reduce the size of the weak links and their separation as well as to improve reproducibility. To reduce these dimensions we improved the patterning of trenches in the Elphy Quantum electron-beam lithography software. In the previous recipe these trenches were patterned as a rectangular grid of exposure points with a specified width and length. Depending on the orientation of the trenches and other factors, the software calculates how to pattern the exposure. In order to eliminate ambiguities in this calculation, we changed the pattern from rectangles to single path lines, with a linear dose of 1300 pC/cm. Only one parameter, the dose, defines the width of the trench, making it easier to control and improving reproducibility.

The second goal was to improve the wet etching technique. The purpose was to find a recipe which would take more time to decrease the relative variability between each wet etch. When the whole etch process is done by hand and takes only 12 s, the relative timing error may be large. To extend the duration of this process we changed the chemical etchant to MF319 from The Dow Chemical Company. The chip is dipped in MF319 at 20° for 55 s and then in DI water at 20°.

Using these two techniques, we were able to etch weak links of less than 150 nm width and separation, as shown in Fig. 3.15(a)

However it turned out that this combination of techniques does not result in a uniform etch. Further investigation is needed to understand why some nanowires are incompletely etched and others perfectly etched, despite being on the same chip, as shown in Fig. 3.15(b). This lack

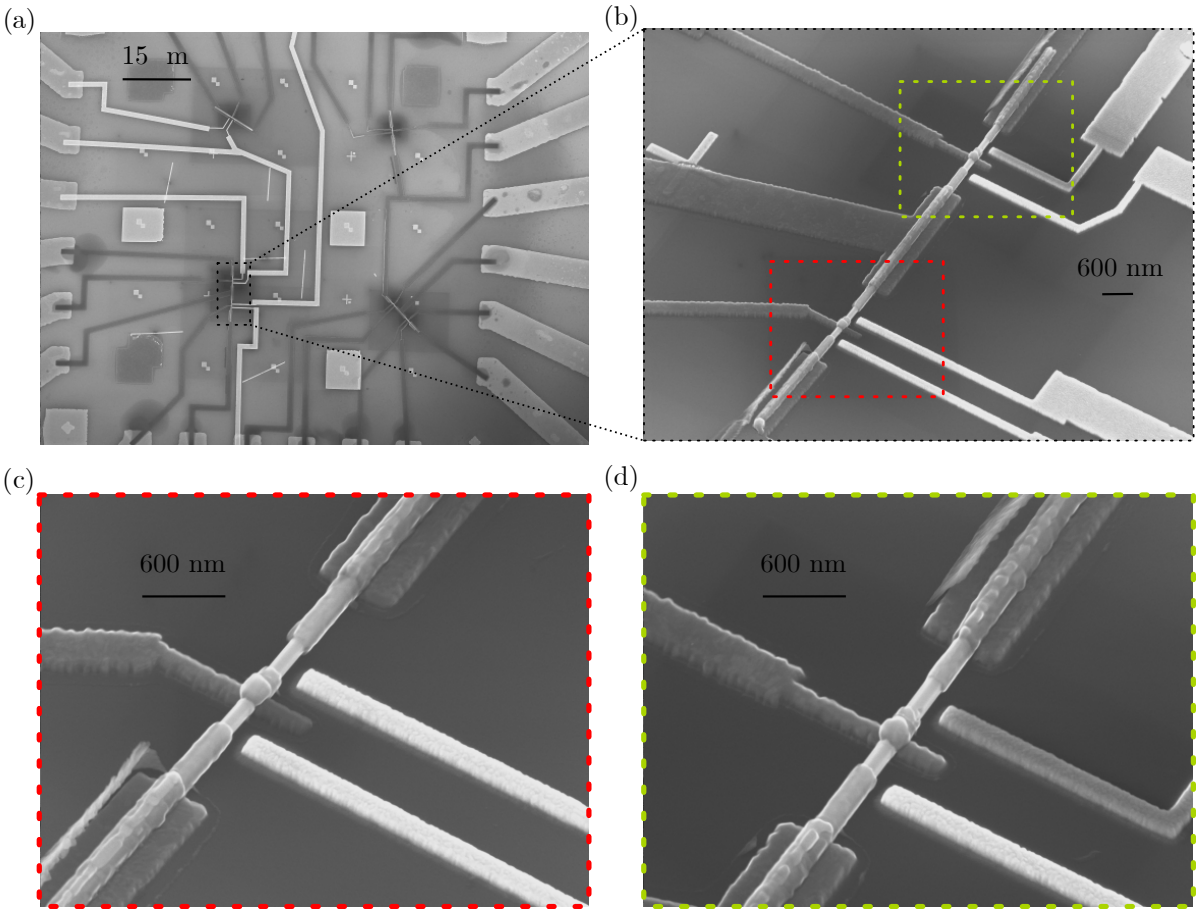

Figure 3.14: Electron micrographs of the chip containing device AM14. (a) Image of the nanowire drop zone. The gray lines are in aluminum and the white lines are in gold. The nanowire inside the black dotted rectangle contains AM14. (b) Image of a nanowire with two potential Andreev molecules: (c) AM14 (red dashed rectangle), for which data is presented in Chap. 2. (d) AM15 (green dashed rectangle) which did not work.

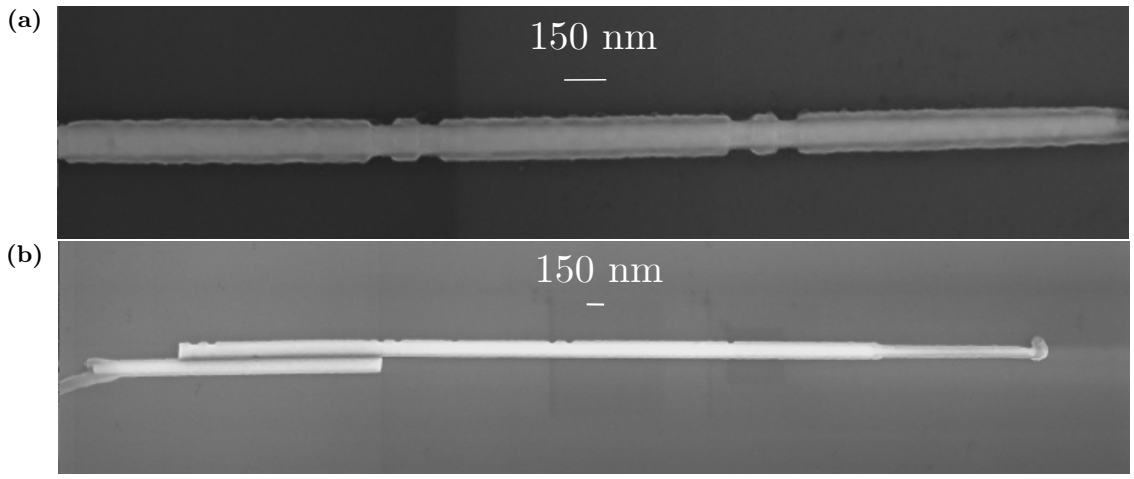

Figure 3.15: Electron micrographs of nanowires on the same chip showing successful etch (a) and failed etch (b). Etch process is MF319 solution at 20° for 55 s.

of uniformity may not be a problem as long as some of the nanowires in the drop zone are properly etched. However if one preselected nanowire needs etching, this recipe is not suitable without further development.

The second challenge is making electrical contact to the small island separating the two weak links, as described in Sec 3.1.5. The small size of the island makes ion milling more delicate, with deformations of the resist due to heating becoming more detrimental. Heat induced changes to the resist layers damages the undercut, resulting in walls after metal deposition as shown in Fig. 3.16(a). During lift-off, these metallic walls are redeposited on the chip and may short the Josephson junctions, as shown in Fig. 3.16(b).

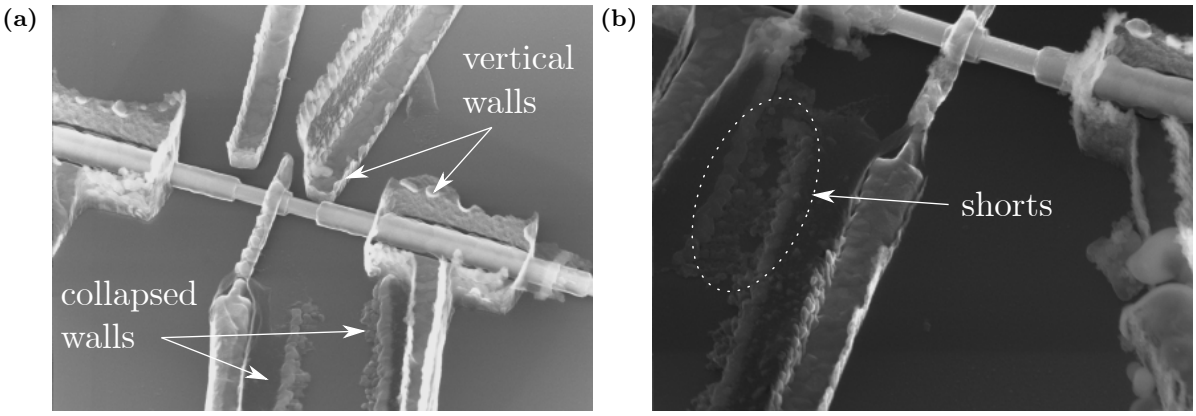

Figure 3.16: Electron micrographs of failed devices with unwanted aluminum walls resulting from ion milling induced resist damage. (a) Device with both vertical and collapsed walls which do not short the circuit. (b) Device with shorts due to collapsed walls.

To overcome re-deposition of sidewalls we tried cooling the chip during ion milling and

by sonicating the sample during lift-off. Since the deformation of the resist is due sample heating, we used the liquid nitrogen cooling system in the electron-beam evaporator to maintain the sample holder at $-70\,°C$ during the entire ion milling and metal deposition process. To terminate lift-off, instead of manual agitation we sonicate the sample for 10 s at low power in order to break the remaining walls. The combination of these two techniques give good results as shown in Fig. 3.17(a).

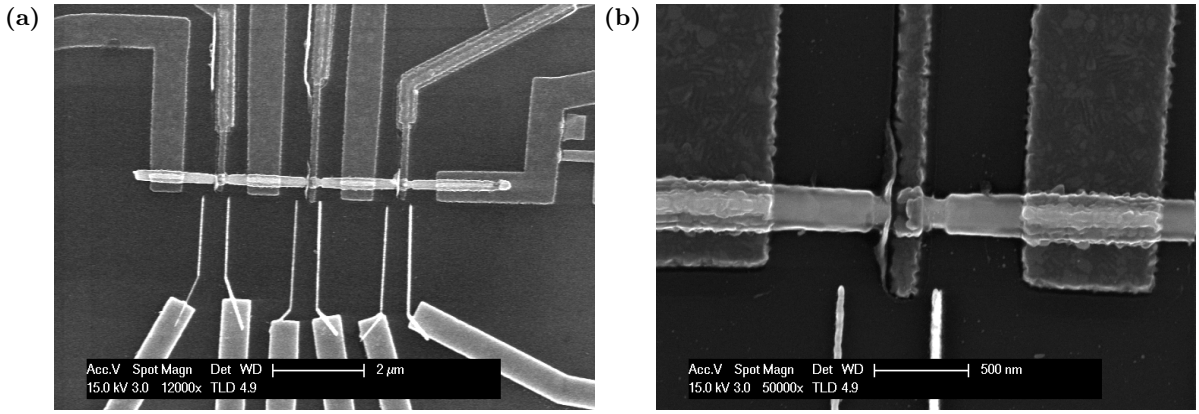

Figure 3.17: Electron micrographs of the last device, with approximately half the junction length and separation as compared to AM14. (a) Image of a nanowire with three potential molecules. (b) Image of one failed device due to shorts. This last device is promising for future realizations of an Andreev molecule.

The last challenge is improving the alignment of patterns to nanowires in electron-beam lithography, essential in contacting the small island separating the junctions of an Andreev molecule. With a double layer of PMMA/MAA, the alignment precision is around 100 nm. To increase precision it would be to necessary to use a smaller working area and a better reference image. These possibilities have only been partially explored.

To conclude, as seen in Fig. 3.17(b), we produced samples with characteristic size divided by two compared to device AM14.

3.2 Cryogenic D.C. measurements

To perform cryogenic D.C. measurement, it is important to take care of noise filtering at each stage of the setup from the sample holder to the electronic equipment needed for data acquisition. In this section, we present the complete measurement and bias circuit and the strategies implemented to minimize noise when measuring the current-voltage characteristics of Andreev molecules.

3.2.1 Chip and sample box

Starting from the chip, on the sample itself two characteristics can be designed to reduce noise. First the use of superconductors all the way to the nanowire to avoid any heat dissipation close to the Josephson junction and thereby thermal noise. This point was overlooked for device AM14 and there are three parasitic resistances, as shown in Fig. 2.4. Fortunately the resistances were small enough so that heating was not an issue for small critical current Andreev molecules. The second strategy, to eliminate common mode noise, is to use a balanced measurement circuit. A completely balanced circuit is not possible for a three-terminal device in which one terminal, the middle superconductor, needs to be connected to ground.

To reduce electromagnetic noise incident on the sample, it is necessary to filter it along the cables coming from the biasing and measurement equipment. Among the different filtering stages, the last stage closest to the sample is made of discrete RC filters. With the necessity to use discrete components close to the chip, a custom sample box was designed to be able to carry a double-sided printed circuit board (PCB). The double-sided multi-layer PCB allows placing all the filtering on one side and connecting to the sample located on the other side of the PCB, as shown in Fig. 3.18(b). The PCB is screwed into a copper sample box which is anchored to the mixing chamber plate. The inward face of the PCB is the filtering circuit. The outward face of the PCB is aligned with a hole in the sample box which is the zone where the chip can be attached and then wire bonded, as shown in Fig. 3.18(a,c). Once the chip is in place, a lid is screwed in the sample holder and place on top of the chip, as shown in Fig. 3.18(d). The inward face of the lid is covered with a layer of magnetically loaded material (Ecosorb MFS series) which has high permeability and magnetic losses. This helps to reduce high-frequency electromagnetic noise and dampens resonant modes of the sample box cavity.

Fig. 3.19 is a simplified schematic of the bias circuit of the PCB and the sample which does not show filtering components. The bias lines $B_{1/2}$ are attenuated by a divisor made of $R_{B1/2}$ and $r_{s1/2}$. There are three measurement lines by junction: $I^{-}_{1/2}$, $I^{+}_{1/2}$ and $V_{JJ1/2}$. Junction voltages are measured at $V_{JJ1/2}$ and from a differential measurement of $I^{\pm}_{1/2}$ and the value of $R_{B1/2}$ one can obtain the junction currents. Lastly, there is one gate bias line per junction, $V_{G1/2}$.

3.2.2 Cryostat wiring and room temperature setup

All the lines of the sample box previously mentioned are filtered along their path to the exterior of the cryostat. Outside the sample box, these lines are twisted pairs, thermally connected to each stage of the cryostat.

All the measurements presented in this thesis were performed in a Bluefors LD dry cryostat reaching a base temperature of 7 mK. It encloses a mu-metal shield preventing the external magnetic field from entering the cryostat.

At the exterior of the cryostat, each pair of measurement lines $I^{-}_{1/2}$ and $I^{+}_{1/2}$ is connected to a DC-coupled, differential voltage preamplifier (LI-75A, NF Corporation). Similarly, each line $V_{JJ1/2}$ is connected to a similar preamplifier in differential mode but with the minus input connected to cold ground. The gate bias lines $V_{G1/2}$ are each connected to a low-noise DC voltage supply (Yokogawa 7651). The bias lines $B_{1/2}$ are connected to a two-channel arbitrary waveform generator (Rigol DG1032).

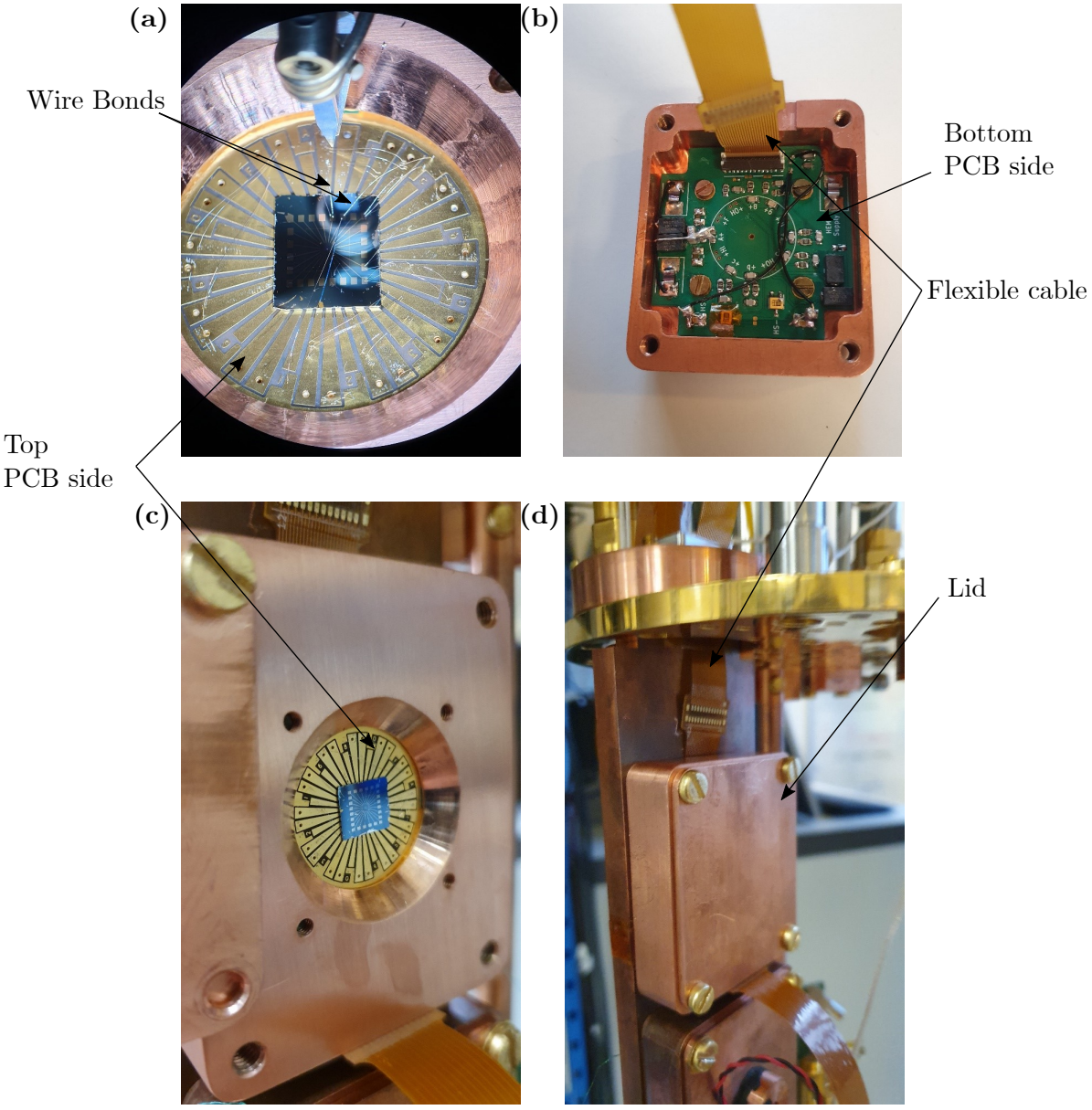

Figure 3.18: Photos of the sample holder, the printed circuit board (PCB) and the sample (a) attached to one side of the PCB and connected with wire bonds. (b) Bottom side of the PCB, with discrete resistances and capacitors. The whole PCB is connected to the exterior via the flexible printed circuit (FPC) cable. (c) Sample holder with a sample inside attached to the cryostat. (d) Sample holder closed and attached to the cryostat.

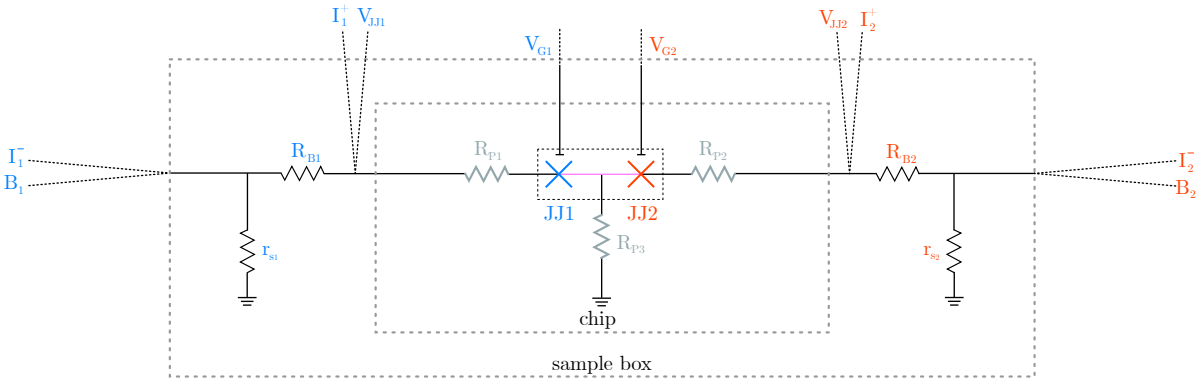

Figure 3.19: Sketch of the biasing circuit inside the sample holder.

To avoid ground loops, the four preamplifiers are powered by batteries. Furthermore, the two gate supplies and the waveform generator are decoupled from building ground with an isolation transformer.

3.3 Cryogenic amplifier and sample isolator: HEMT

Low noise DC measurements at millikelvin temperatures are challenging, especially in a closed-cycle cryostat. In general at low frequencies the noise spectral density is high and few components, such as amplifiers or circulators, exist or work at cryogenic temperatures and can help alleviate this noise. The difficulty in isolating a sample from noise near zero frequency and amplifying the signal is a great hindrance to DC measurements.

For example, to maximize and measure the switching current of a junction it is important to reduce the noise coming to the junction and to have enough bandwidth to do perform statistics. In the setup shown in Fig. 3.19, the noise coming from the bias line is attenuated down to DC, however, the noise coming from the unattenuated measurement lines ($V_{JJ1/2}, I_{1/2}^{+/-}$) directly affects the sample. There are many sources of noise which can propagate through these cables, including magnetic pickup in cable loops, thermal noise, and triboelectric noise. High frequency noise can be filtered through a mix of discrete and distributed filters, such as Eccosorb, copper powder filters, thermocoax, and microwave capacitors. When filtering for DC measurements, a balance must be struck between noise and bandwidth. Furthermore, in a closed cycle cryostat such as the Bluefors SD/LD used for this thesis, one of the main sources of low frequency noise is the triboelectric noise coming from the vibration of the cables connecting the samples. Since cables vibrate over their whole length, the corresponding noise source is also distributed.

In this kind of setup a solution to reduce noise impinging on the sample is to place an amplifier with a low output impedance, in a buffer or isolator configuration, as close to the sample as possible. Thereby, noise coming from the measurement lines will be shorted to ground without passing through the sample. Unfortunately, there is no commercial DC low-noise amplifier which can work at millikelvin temperatures.

Fortunately, there exist high-electron mobility transistors (HEMTs), made by Dr. Yong Jin, a principal investigator of the NanoFET group at C2N, which have low noise at low frequencies, which work at 4 K, and are immune to freeze-out effects which would make them fail at lower

temperatures [66, 72]. This motivated us to use these HEMTs as millikelvin DC amplifiers and isolators. HEMTs are field-effect transistors made of different layers of semiconducting material (GaAs) which allow tuning with a gate the carrier density of a two-dimensional electron gas (2DEG) connecting the source and drain terminals. HEMTs were discovered by Takashi Mimura in 1980 [73] and integrated in circuits the following year [74]. Nowadays, such HEMTs are frequently incorporated into sensitive microwave amplifiers, including for cosmology [75, 76, 77, 78]. Although these HEMTs should work at millikelvin temperature, there are additional challenges regarding dissipation or heating which must be addressed.

In this section we present a protocol to use HEMTs as DC amplifier at millikelvin temperatures. The amplifier is DC-coupled, has a gain of approximately 7, and sub-nV/$\sqrt{\text{Hz}}$ voltage noise at 100 Hz. The first part will introduce the operational principal of a HEMT. The second part is a description of the bias cooling process necessary to make the HEMT work at mK temperature. The last part is the presentation of the acquisition of a current-voltage characteristic of a Josephson junction forming part of an Andreev molecule measured with a HEMT.

3.3.1 Operational principle

A HEMT is a three-terminal device with a source, a drain and a gate, as shown in Fig. 3.20(a,c). The drain and the source are connected through a 2DEG whose carrier density can be tuned by the capacitively coupled gate. Applying a voltage at the gate tunes the source-drain conductance and affects the current passing between drain and source. When linearized about the operating point, this relationship can be expressed as

$$\delta I_{DS} = g_m \delta V_{GS}, \tag{3.1}$$

with g_m the transconductance of the HEMT, I_{DS} the current between drain and source and V_{GS} the voltage between gate and source.

To measure a Josephson junction using a HEMT as an amplifier we follow a common source circuit topology as shown in Fig. 3.20(c). The source degeneration, or the presence of the resistance R_S, allows bias cooling the HEMT. The junction is connected to the gate terminal at one end and to ground at the other end. Not shown is the junction biasing circuit which would also be connected to the gate. The signal to amplify is the voltage at the junction V_G and the amplified output voltage is V_D. Most importantly, the noise coming from the biasing lines V_{BC1}, V_{b1} and the measurement line V_{b1} are only capacitively coupled to the Josephson junction and is therefore blocked at low frequencies. The relevant gate-source and gate-drain capacitances (C_{gs} and C_{gd}) are small, on the order of 1 pF to 300 pF, and are not shown in Fig. 3.20(c). In this configuration, the voltage source V_{b1} supplies power to the HEMT. The HEMT drain-source voltage is

$$V_{DS} = V_{b1} - I_{DS}\left(R_D + R_S\right), \tag{3.2}$$

with $V_{DS} = V_D - V_S$, R_D the drain resistance and R_S the source resistance. If the voltage at the junction changes, for example when switching, as a result of Eq. 3.1 the current passing between drain and source will also change. This variation in current will lead to a change in the voltage V_D and result in voltage gain,

$$\frac{\delta V_{out}}{\delta V_{in}} = \frac{\delta\left(V_S + V_{DS}\right)}{\delta V_G} = \alpha, \tag{3.3}$$

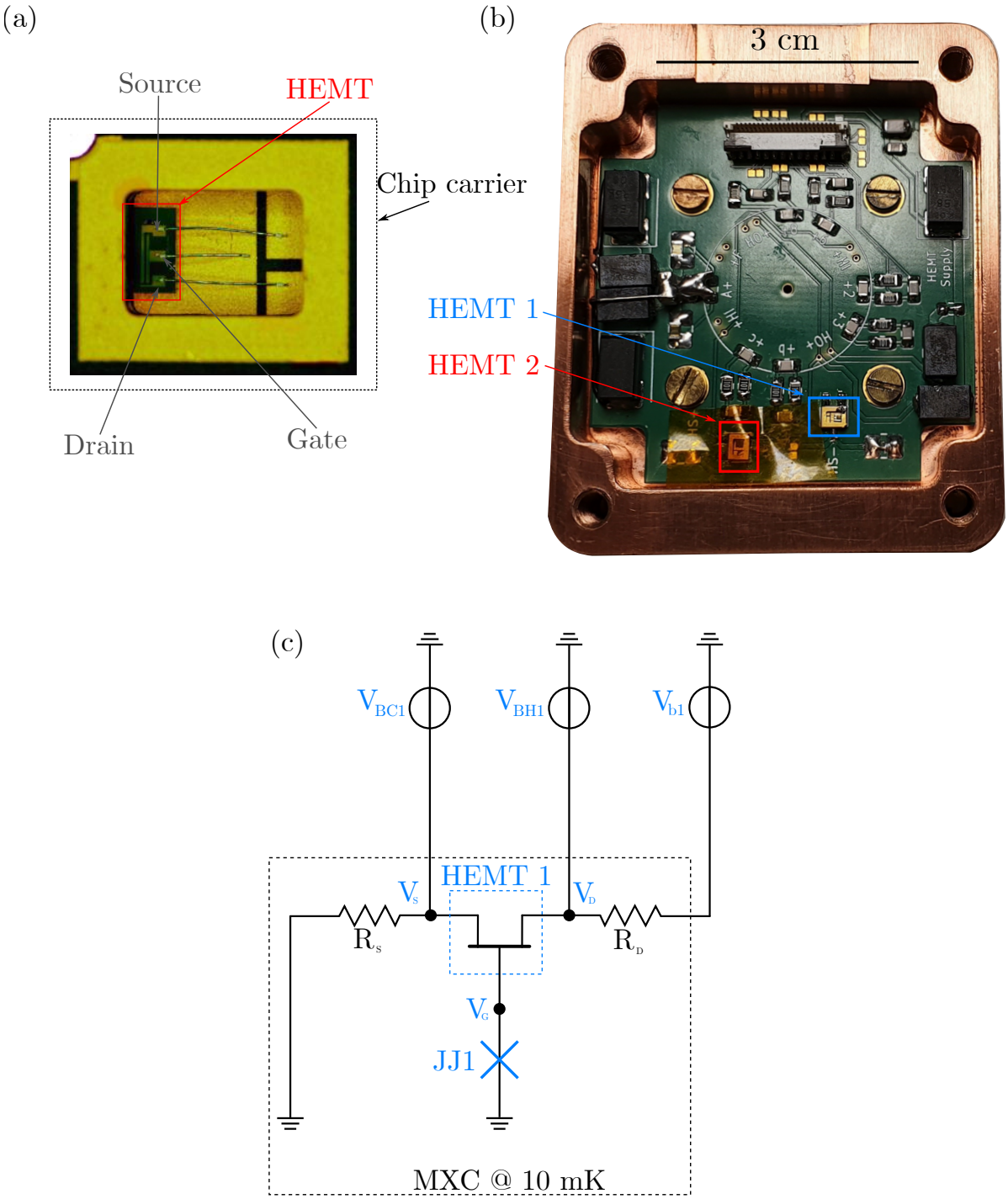

Figure 3.20: (a) HEMT wire-bonded inside of chip carrier. Image courtesy Yong Jin and Quan Dong. (b) Sample holder showing printed circuit board containing HEMTs and biasing circuits. The sample is in close proximity on the back side of the PCB in the central circular region as shown in Fig. 3.18(c). (c) Schematic of an electrical circuit used to bias cool and measure a HEMT amplifier connected to a Josephson junction.

with a gain α given by,

$$\alpha = \frac{-g_m R_D}{1 + g_m R_S}. \tag{3.4}$$

To maximize the gain α one would reduce R_S and increase R_D, however one must also take into account dissipation which could heat the mixing chamber stage of the fridge.

An important characteristic of HEMTs is the pinch-off voltage, the gate-source voltage difference at which the transconductance g_m is non-zero. Below the pinch-off voltage the HEMT cannot be used to amplify. A typical gate-source voltage $V_{GS} = V_G - V_S$ to operate these cryogenic HEMTs is $-150\,\mathrm{mV}$, and will change slightly for each batch of HEMTs. Since the Josephson junction is connected to ground and will only be biased in a range of $4\Delta \approx 1\,\mathrm{mV}$ with $\Delta = 180\,\mu\mathrm{V}$ for aluminum, $V_G \approx 0$. Therefore one would have to apply a large positive voltage $V_{RS} \approx 150\,\mathrm{mV}$ on R_S such that $V_{GS} = -150\,\mathrm{mV}$. The power dissipated by R_S is $P_{RS} = V_{RS}^2/R_S$ and should not exceed the cooling power of the cryostat near base temperatures, $20\,\mu\mathrm{W}$. Therefore the value of R_S cannot be too small. At the same time, to keep the gain high, we would like to increase R_D but this will also result in dissipation, $P_{RD} = I_{DS}^2 R_D$. Finally, gain can be improved by increasing the value of g_m, but this is only possible by increasing the drain-source current and therefore the dissipation in the HEMT itself, $P_H = I_{DS} V_{DS}$.

An equilibrium needs to be found between amplification and dissipation. Our closed-cycle cryostat has a cooling power of approximately $20\,\mu\mathrm{W}$ at $10\,\mathrm{mK}$. We primarily want to use a HEMT as an isolator and if there is any remaining cooling power we can optimize the circuit for amplification. One solution to avoid the problems of heating is to place the HEMT and the resistances R_S, R_D at the $1\,\mathrm{K}$ or $4\,\mathrm{K}$ stage of the cryostat where there is ample cooling power. However the drawback of this solution is that the junction could pick up noise from the intermediate cabling. Although this strategy improves upon simple room temperature signal amplification, it is not the best we can do in terms of isolating the junction.

A better solution exists which is to change the operating point of the HEMT. By using a method called bias cooling [66, 72], one can shift the pinch-off voltage closer to zero. By doing so the operating point can be set to a value of $V_{GS} = 0\,\mathrm{mV}$, eliminating the heat dissipated in R_S, increasing the gain, and allowing the use of the HEMT in a common source topology at mK temperature. Using this method, the HEMT can be placed on the same printed circuit board as the sample as shown in Fig. 3.20.

3.3.2 Bias cooling

When a HEMT is cooled down, usually the gate and source terminals are grounded. Bias cooling corresponds to applying a non-zero gate-source voltage, $V_{GS} = V_{GC}$, during cooldown. This potential difference may "freeze-in" charges at low temperature and can thereby shift the pinch-off voltage [66]. Applying positive V_{GC} will shift the $I_{DS} - V_{GS}$ towards the right, as shown in Fig. 3.21(a) and oppositely a negative value will push the operating point towards the left [66, 72].

Fig. 3.21(a) represents the $I_{DS} - V_{GS}$ characteristic of one HEMT for different bias cooling voltages V_{GC}. With the HEMT above $200\,\mathrm{K}$, this gate offset is applied by biasing the source with the supply voltage V_{BC1}, always keeping the gate terminal grounded such that $V_{GC} = -V_S$. The exact value of V_{GC} can be measured at V_{BH1} 3.20(c) and the drain supply V_{b1} is left floating. When the source bias is zero such that $V_{GC} = 0\,\mathrm{V}$) during cooldown the base temperature

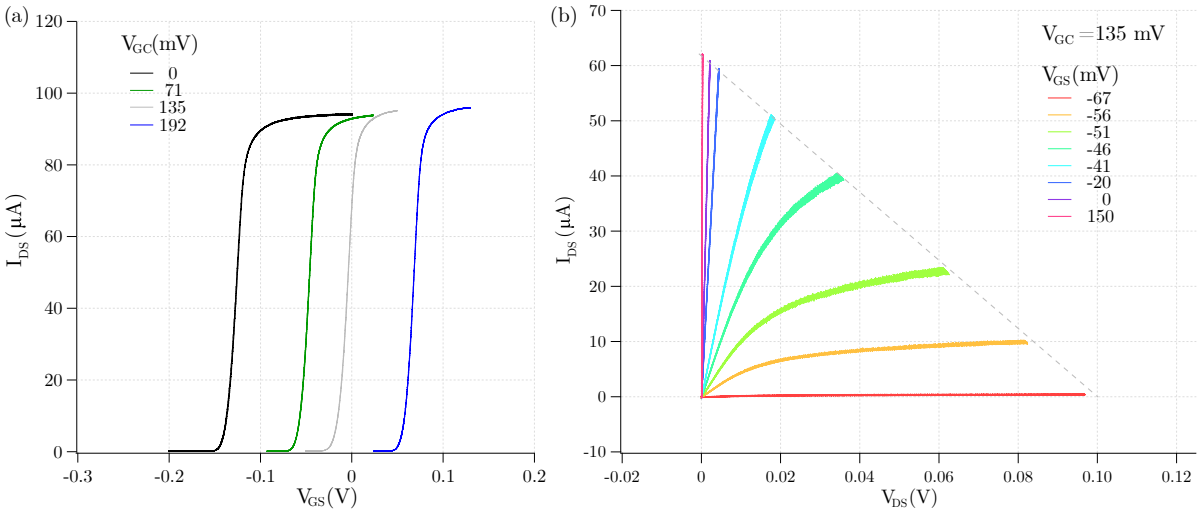

Figure 3.21: (a) $I_{DS} - V_{GS}$ characteristics of cryogenic HEMT at different bias cooling voltages V_{GC}. (b) $I_{DS} - V_{DS}$ characteristic of HEMT bias-cooled with $V_{GC} = 135\,\mathrm{mV}$ for different values of gate voltage V_{GS}.

pinch-off point of the HEMT is around $V_{GS} = -150\,\mathrm{mV}$. Even if this value is different for each HEMT, for one HEMT the same cool down protocol will give the same operating point. With this reproducibility, it is possible to tune the bias cooling voltage to place the operating point of a HEMT where it is beneficial for the measurement.

To measure a Josephson junction's switching current, the main points to optimize are the gain and the power dissipation. To minimize the dissipation in R_S, the HEMT needs to have its operating point at $V_{GS} = 0\,\mathrm{V}$. The total power dissipated in the HEMT and the biasing circuit is

$$P_{tot} = I_{DS}^2(R_S + R_D) + I_{DS}V_{DS}. \tag{3.5}$$

From this equation and regarding the gain we want to achieve, we distribute the power dissipation evenly between the resistances and the HEMT.

For a given bias cooling voltage and value of resistances (R_S, R_D), the current and voltage states accessible by a HEMT are shown in Fig. 3.21. The $I_{DS} - V_{DS}$ characteristic for different values of gate voltage shows the possible current-voltage configuration for the HEMT. Starting from one current-voltage state, a HEMT has to follow the load line (dashed gray lines) with a slope of $1/(R_D + R_S)$ to move to a new state. In optimizing HEMT operation, higher gain is generally associated with higher power but also more dissipation.

With all these constraints, choosing the values of resistances, bias cooling voltage and operating current-voltage is a complex optimization where different solutions are possible. The main factors to determine these values will be the type of measurement to perform and the cooling power available.

3.3.3 Data acquisition with a bias cooled HEMT

This section presents the acquisition protocol and switching current data of one Josephson junction. The measured junction is part of device AM20 (Fig. 3.17(b)), a failed Andreev

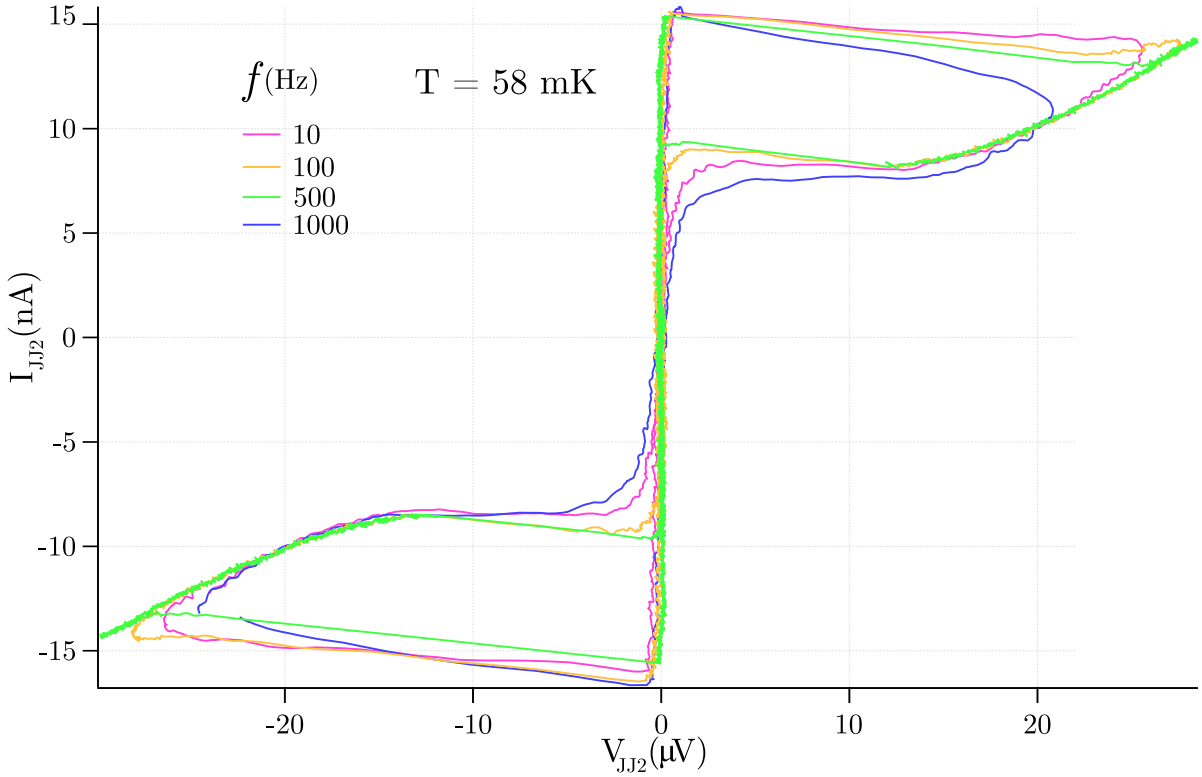

Figure 3.22: Current-voltage characteristics of one Josephson junction in device AM20 (Fig. 3.17(b)) measured at different frequencies f with a cryogenic, bias-cooled HEMT.

molecule in which one of the junctions is shorted. The remaining junction is studied in this section.

With the available cooling power of 20 µW at 20 mK and with the objective of measuring two Josephson junctions with independent HEMTs simultaneously, the power dissipated for each amplifier must be less than 10 µW. If we allocate the power evenly between the resistances R_S, R_D and the HEMT, each component must dissipate less than approximately 3 µW. Balancing between power dissipation and gain, (Eq. 3.4), the chosen resistances are $R_D = 1\,\mathrm{k}\Omega$ and $R_S = 10\,\Omega$ and an operating point for the HEMT of $I_{DS} \approx 50\,\mu\mathrm{A}, V_{DS} \approx 50\,\mu\mathrm{V}$.

The HEMT used in this section has been calibrated such that the bias cooling voltage necessary to place its operating point at zero V_{GS} is already known and corresponds to $V_{GC} = 128.55\,\mathrm{mV}$. Similarly, the gain has been calibrated to $\alpha = 8.6$. This value is in accordance with Eq. 3.4, it corresponds to $g_m \approx 9.4$.

The data acquisition is in two steps: the bias cooling and the measurement. To bias cool the circuit, the previously determined bias cooling voltage needs to be applied across the gate and source terminals of the HEMT. Referring to Fig. 3.20(a), we apply the negative of the bias cooling value to the source via V_{BC1}, such that $V_{GS} = -V_S = 128.55\,\mathrm{mV}$ is at the correct positive value. Since this preparation is done at room temperature where the pinch-off voltage is approximately $-150\,\mathrm{mV}$, the HEMT is on. The drain terminal is shorted outside the fridge via the supply V_{b1} which is set to zero. To check the value of V_S applied by V_{BC1}, a voltmeter is connected to V_{BH1}. Since the HEMT is on and g_m is large, the voltage drop V_{DS} is small compared to $I_{DS}R_D$ and therefore $V_{GS} = -V_S \approx -V_D$ (3.21(b)).

The power dissipated in R_S during bias cooling is $V_{GC}^2/10 \approx 1.65\,\mathrm{mW}$ which is much too high to maintain at base temperature. Before condensing the dilution unit, when the mixing chamber is approximately at 7 K, bias cooling is turned off. At this temperature, electrons in the HEMT are already frozen in. Once the fridge has reached base temperature, the HEMT is turned on by biasing V_{b1} such that $V_{DS} = 50\,\mathrm{mV}$. We also verify that $I_{DS} \approx 50\,\mu\mathrm{A}$. The measurements are performed in a Bluefors SD which has a cooling power of 20 µW at 20 mK. The operating temperature is at 58 mK which is higher than expected.

To measure the switching current, we bias the junction with a circuit similar to the one in the experiment presented in Fig.3.19. The measurement lines are different in this circuit, with only line I_1^+ remaining in Fig.3.19. There are no more unattenuated direct measurement lines connected to the junctions. The amplified junction voltage is measured at V_D and from the difference with I_1^+ one can calculate the junction current.

Fig.3.22 shows the current-voltage characteristic of the junction measured with the HEMT at different sweep frequencies. The switching current of the junction is approximately 15 nA with a junction's gate voltage $V_{JG} = 0\,\mathrm{V}$. This value is comparable to the junctions measured in Chap. 2 (device AM14). The fact that the mean switching current varies little with sweep frequency between 10 Hz to 1000 Hz is promising in terms of the low-frequency noise isolation provided by the HEMT. Measurements of the switching probability and extraction of the effective temperature, as well as control measurements, would be necessary to fully quantify the role of the HEMT in reducing noise. However, this junction is much more isolated than the previous ones, so a higher current could have been expected. This could be explained by the fact that this junction was not made using the same fabrication recipe and do not present the same physical characteristics. However, even if these first considerations let us think that these measurements could be noisier, the stability of the switching current value for different

frequencies shows how isolate is the junction. These last measurements show how effective are the isolation and the amplification of a HEMT. Using bias cooling techniques, we were able to measure the switching current of a Josephson junction up to 1 kHz without diminishing its value.

Conclusion

This thesis was motivated by work on multi-terminal Josephson junction circuits [38, 21], specifically Cooper pairs quartets [22]. Experimental work on the hybridization of Andreev bound states at non-zero voltage [23, 24] revealed intriguing physics and raised several questions. This thesis focused on studying the hybridization of Andreev bound states at zero voltage both with a different theoretical formalism and a different type of experiment.

Theoretically, we calculated properties of the Andreev molecule, two closely Josephson junctions, within the Bogoliubov-de Gennes formalism. Using three different techniques we explored different aspects of the Andreev molecule. Our simplest model consisted of two one-dimensional single-channel junctions separated by a superconducting segment. We calculated the energy spectra and current-phase relation of such a system for varying junction separation, channel transmissions, and phase configurations. These studies allowed describing the spatial dependence of hybridization in an Andreev molecule, showing exactly how various phenomena such as the energy gap varied with the length of the superconducting segment separating the two junctions. We developed the link between these phenomena and the two microscopic mechanisms at the core of the hybridization, double elastic cotunneling and double-crossed Andreev reflection. Most importantly, Andreev state hybridization changes the current-phase relation of the junctions. The theory predicts non-local Josephson effects where the phase of one junction can influence the current-phase relation of the other junction. One striking effect is the possibility of a φ_0-junction where a junction may have a non-zero supercurrent with zero-phase difference. A second step was to describe one-dimensional, multi-channel Andreev molecules. Numerical simulations of such Andreev molecules with random scattering matrices showed more complex structure but with experimentally identifiable signatures such as energy gaps and modifications to the current-phase relation. The last step was to use a tight-bonding model which allowed representing two-dimensional systems with disorder. This last representation, the closest to a real system, showed the robustness of hybridization to disorder.

Experimentally, a two-junction system was fabricated based on InAs-Al nano-wire from Peter Krogstrup's group from the University of Copenhagen [25] and thanks to the sharing of knowlodge and facility of the Quantronique group. The junctions made of aluminum were separated by 330 nm. The objective was to measure the influence of one junction on the supercurrent of the other one. A map delimiting the zero voltage region as a function of both junctions' bias currents was acquired. Unfortunately the measurement had too much noise to be conclusive. However some features of the map indicate agreement with theory and are encouraging for the design of future experiments. Lastly, in subsequent measurements a protocol was developed to use a cryogenic HEMT to isolate the junctions from noise and to amplify their voltage signal.

To conclude, this thesis gives a better understanding of the hybridization of Andreev bound states at zero voltage and presents experiments paving the way for the detection of an Andreev molecule.

There are several perspectives to improve on this work. In the short term, producing new samples with a smaller junction separation is the main objective. A new fabrication recipe was developed to overcome the problems encountered in making the first batch of samples. We hope to perform pulsed switching measurements with the next batch of samples using the cryogenic HEMTs.

Eventually, it will be necessary to explore the phase space of an Andreev molecule with a phase-biased switching current measurement. Measuring the spectrum of an Andreev molecule using the Josephson spectrometer developed by the group [79] or with conventional microwave spectroscopy could establish the existence of hybridization-induced gaps.

In the much longer term, the Andreev molecules have prospects for both quantum information and quantum simulation. Regarding quantum information, an Andreev molecule can be considered a tunable four-state qubit and could be useful in implementing gates in an Andreev bound state based quantum computer. Finally, one could extend Andreev molecules to more than two Josephson junctions, realizing Andreev "polymers" or more complex structures with multiple closely spaced weak links. Such Andreev systems may allow simulating the chemistry of real molecules, or help in implementing exotic Hamiltonians, such as the SSH model or the Kitaev chain.

Bibliography

[1] B.D. Josephson. "Possible new effects in superconductive tunnelling". In: *Physics Letters* 1.7 (July 1962), pp. 251–253. DOI: 10.1016/0031-9163(62)91369-0

Cited pages VII, 1

[2] P. W. Anderson and J. M. Rowell. "Probable Observation of the Josephson Superconducting Tunneling Effect". In: *Physical Review Letters* 10.6 (Mar. 1963), pp. 230–232. DOI: 10.1103/physrevlett.10.230

Cited pages VII, 1

[3] Alex I. Braginski John Clarke. *The SQUID Handbook*. Wiley-VCH, Mar. 2006. 395 pp. ISBN: 9783527604586. URL: https://www.ebook.de/de/product/21192549/john_clarke_alex_i_braginski_the_squid_handbook.html

Cited pages VII, 1

[4] S.P. Benz and C.A. Hamilton. "Application of the Josephson effect to voltage metrology". In: *Proceedings of the IEEE* 92.10 (Oct. 2004), pp. 1617–1629. DOI: 10.1109/jproc.2004.833671

Cited pages VII, 1

[5] Lucas Lamata et al. "Digital-analog quantum simulations with superconducting circuits". In: *Advances in Physics: X* 3.1 (Jan. 2018), p. 1457981. DOI: 10.1080/23746149.2018.1457981

Cited pages VII, 1

[6] M. H. Devoret and R. J. Schoelkopf. "Superconducting Circuits for Quantum Information: An Outlook". In: *Science* 339.6124 (Mar. 2013), pp. 1169–1174. DOI: 10.1126/science.1231930

Cited pages VII, 1

[7] J. H. Plantenberg et al. "Demonstration of controlled-NOT quantum gates on a pair of superconducting quantum bits". In: *Nature* 447.7146 (June 2007), pp. 836–839. DOI: 10.1038/nature05896

Cited pages VII, 1

[8] John M. Martinis, Michel H. Devoret, and John Clarke. "Energy-Level Quantization in the Zero-Voltage State of a Current-Biased Josephson Junction". In: *Physical Review Letters* 55.15 (Oct. 1985), pp. 1543–1546. DOI: 10.1103/physrevlett.55.1543

Cited pages VII, 1

[9] Y. Nakamura, Yu. A. Pashkin, and J. S. Tsai. "Coherent control of macroscopic quantum states in a single-Cooper-pair box". In: *Nature* 398.6730 (Apr. 1999), pp. 786–788. DOI: 10.1038/19718

Cited pages VII, 1

[10] D. Vion. "Manipulating the Quantum State of an Electrical Circuit". In: *Science* 296.5569 (May 2002), pp. 886–889. DOI: 10.1126/science.1069372

Cited pages VII, 1

[11] I. Chiorescu. "Coherent Quantum Dynamics of a Superconducting Flux Qubit". In: *Science* 299.5614 (Feb. 2003), pp. 1869–1871. DOI: 10.1126/science.1081045

Cited pages VII, 1

[12] Jens Koch et al. "Charge-insensitive qubit design derived from the Cooper pair box". In: *Physical Review A* 76.4 (Oct. 2007), p. 042319. DOI: 10.1103/physreva.76.042319

Cited pages VII, 1

[13] V. E. Manucharyan et al. "Fluxonium: Single Cooper-Pair Circuit Free of Charge Offsets". In: *Science* 326.5949 (Oct. 2009), pp. 113–116. DOI: 10.1126/science.1175552

Cited pages VII, 1

[14] K. K. Likharev. *Dynamics of Josephson junctions and circuits*. New York: Gordon and Breach Science Publishers, 1986. ISBN: 2881240429

Cited pages VII, 1

[15] J. Bindslev Hansen and P. E. Lindelof. "Static and dynamic interactions between Josephson junctions". In: *Reviews of Modern Physics* 56.3 (July 1984), pp. 431–459. DOI: 10.1103/revmodphys.56.431

Cited pages IX, 1, 3

[16] G. Deminova and A. Kovalenko. "A calculation of interaction between two Josephson junctions". In: *IEEE Transactions on Magnetics* 15.1 (Jan. 1979), pp. 291–294. DOI: 10.1109/tmag.1979.1060183

Cited pages IX, 3

[17] Axel Freyn et al. "Production of Nonlocal Quartets and Phase-Sensitive Entanglement in a Superconducting Beam Splitter". In: *Physical Review Letters* 106.25 (June 2011). DOI: 10.1103/physrevlett.106.257005

Cited pages IX, 3, 55

[18] T. Jonckheere et al. "Multipair dc Josephson resonances in a biased all-superconducting bijunction". In: *Physical Review B* 87.21 (June 2013), p. 214501. DOI: 10.1103/physrevb.87.214501

Cited pages IX, 3

[19] R. Mélin et al. "D.C. Josephson transport by quartets and other Andreev resonances in superconducting bijunctions". In: *J. Phys.: Conf. Ser.* 568 (2014)

Cited pages IX, 3

[20] Denis Feinberg et al. "Quartets and the current-phase structure of a double quantum dot superconducting bijunction at equilibrium". In: *The European Physical Journal B* 88.4 (Apr. 2015). DOI: 10.1140/epjb/e2015-50849-3

Cited pages IX, 3

[21] Régis Mélin et al. "Gate-tunable zero-frequency current cross correlations of the quartet state in a voltage-biased three-terminal Josephson junction". In: *Physical Review B* 93.11 (Mar. 2016), p. 115436. DOI: 10.1103/physrevb.93.115436

Cited pages IX, 3, 103

[22] Régis Mélin et al. "Simple Floquet-Wannier-Stark-Andreev viewpoint and emergence of low-energy scales in a voltage-biased three-terminal Josephson junction". In: *Physical Review B* 95.8 (Feb. 2017), p. 085415. DOI: 10.1103/physrevb.95.085415

Cited pages IX, 3, 103

[23] A. H. Pfeffer et al. "Subgap structure in the conductance of a three-terminal Josephson junction". In: *Physical Review B* 90.7 (Aug. 2014). DOI: 10.1103/physrevb.90.075401

Cited pages IX, 3, 55, 103

[24] Yonatan Cohen et al. "Nonlocal supercurrent of quartets in a three-terminal Josephson junction". In: *Proceedings of the National Academy of Sciences* 115.27 (June 2018), pp. 6991–6994. DOI: 10.1073/pnas.1800044115

Cited pages IX, 3, 55, 103

[25] P. Krogstrup et al. "Epitaxy of semiconductor–superconductor nanowires". In: *Nature Materials* 14.4 (Jan. 2015), pp. 400–406. DOI: 10.1038/nmat4176

Cited pages IX, 3, 15, 55, 77, 78, 103

[26] J.-D. Pillet et al. "Nonlocal Josephson Effect in Andreev Molecules". In: *Nano Letters* 19.10 (Aug. 2019), pp. 7138–7143. DOI: 10.1021/acs.nanolett.9b02686

Cited pages 5, 31, 34, 38, 39, 42

[27] Jean-Damien Pillet et al. "Scattering description of Andreev molecules". In: *SciPost Physics Core* 2.2 (June 2020). DOI: 10.21468/scipostphyscore.2.2.009

Cited page 5

[28] L. Bretheau et al. "Exciting Andreev pairs in a superconducting atomic contact". In: *Nature* 499.7458 (July 2013), pp. 312–315. DOI: 10.1038/nature12315. arXiv: 1305.4091 [cond-mat.mes-hall]. URL: https://ui.adsabs.harvard.edu/abs/2013Natur.499..312B

Cited pages 5, 76

[29] M. L. Della Rocca et al. "Measurement of the Current-Phase Relation of Superconducting Atomic Contacts". In: *Physical Review Letters* 99.12 (Sept. 2007). DOI: 10.1103/physrevlett.99.127005

Cited page 5

[30] S. M. Albrecht et al. "Exponential protection of zero modes in Majorana islands". In: *Nature* 531.7593 (Mar. 2016), pp. 206–209. DOI: 10.1038/nature17162

Cited page 6

[31] M. T. Deng et al. "Majorana bound state in a coupled quantum-dot hybrid-nanowire system". In: *Science* 354.6319 (Dec. 2016), pp. 1557–1562. DOI: 10.1126/science.aaf3961

Cited page 6

[32] M F Goffman et al. "Conduction channels of an InAs-Al nanowire Josephson weak link". In: *New Journal of Physics* 19.9 (Sept. 2017), p. 092002. DOI: 10.1088/1367-2630/aa7641

Cited pages 6, 63

[33] G. E. Blonder, M. Tinkham, and T. M. Klapwijk. "Transition from metallic to tunneling regimes in superconducting microconstrictions: Excess current, charge imbalance, and supercurrent conversion". In: *Physical Review B* 25.7 (Apr. 1982), pp. 4515–4532. DOI: 10.1103/physrevb.25.4515

Cited page 13

[34] John Bardeen et al. "Structure of Vortex Lines in Pure Superconductors". In: *Physical Review* 187.2 (Nov. 1969), pp. 556–569. DOI: 10.1103/physrev.187.556

Cited page 14

[35] C. W. J. Beenakker and H. van Houten. "Josephson current through a superconducting quantum point contact shorter than the coherence length". In: *Physical Review Letters* 66.23 (June 1991), pp. 3056–3059. DOI: 10.1103/physrevlett.66.3056

Cited pages 14, 22

[36] Philip F. Bagwell. "Suppression of the Josephson current through a narrow, mesoscopic, semiconductor channel by a single impurity". In: *Physical Review B* 46.19 (Nov. 1992), pp. 12573–12586. DOI: 10.1103/physrevb.46.12573

Cited page 18

[37] Magnus Hurd and Göran Wendin. "Superconducting current in a ballistic double superconducting – normal-metal – superconducting structure". In: *Physical Review B* 51.6 (Feb. 1995), pp. 3754–3759. DOI: 10.1103/physrevb.51.3754

Cited page 18

[38] P. Samuelsson et al. "Nonequilibrium Josephson effect in mesoscopic ballistic multiterminal SNS junctions". In: *Physical Review B* 62.2 (July 2000), pp. 1319–1337. DOI: 10.1103/physrevb.62.1319

Cited pages 18, 103

[39] D. G. Olivares et al. "Dynamics of quasiparticle trapping in Andreev levels". In: *Physical Review B* 89.10 (Mar. 2014). DOI: 10.1103/physrevb.89.104504

Cited page 18

[40] A. Y. Kasumov et al. "Supercurrents through single-walled carbon nanotubes". In: *Science* 284.5419 (1999), pp. 1508–1511

Cited page 20

[41] Pablo Jarillo-Herrero, Jorden A. van Dam, and Leo P. Kouwenhoven. "Quantum supercurrent transistors in carbon nanotubes". In: *Nature* 439.7079 (Feb. 2006), pp. 953–956. DOI: 10.1038/nature04550

Cited page 20

[42] J-D. Pillet et al. "Andreev bound states in supercurrent-carrying carbon nanotubes revealed". In: *Nature Physics* 6.12 (Nov. 2010), pp. 965–969. DOI: 10.1038/nphys1811

Cited page 20

[43] J.-D. Pillet et al. "Tunneling spectroscopy of a single quantum dot coupled to a superconductor: From Kondo ridge to Andreev bound states". In: *Physical Review B* 88.4 (July 2013). DOI: 10.1103/physrevb.88.045101

Cited page 20

[44] A. A. Golubov, M. Yu. Kupriyanov, and E. Il'ichev. "The current-phase relation in Josephson junctions". In: *Reviews of Modern Physics* 76.2 (Apr. 2004), pp. 411–469. DOI: 10.1103/revmodphys.76.411

Cited page 20

[45] S. Datta, P.F. Bagwell, and M.P. Anantram. *Scattering Theory of Transport for Mesoscopic Superconductors*. Technical report (Purdue University. School of Electrical and Computer Engineering). Purdue University, School of Electrical and Computer Engineering, 1996. URL: https://books.google.fr/books?id=ud16GwAACAAJ

Cited page 30

[46] C. W. J. Beenakker. "Random-matrix theory of quantum transport". In: *Reviews of Modern Physics* 69.3 (July 1997), pp. 731–808. DOI: 10.1103/revmodphys.69.731

Cited pages 31, 34

[47] Francesco Mezzadri. "How to generate random matrices from the classical compact groups". In: *NOTICES of the AMS, Vol. 54 (2007), 592-604* (Sept. 18, 2006). arXiv: math-ph/0609050v2 [math-ph]

Cited pages 31, 34

[48] Yaroslav M. Blanter Yuli V. Nazarov. *Quantum Transport*. Cambridge University Pr., May 1, 2009. ISBN: 0521832462. URL: https://www.ebook.de/de/product/8217177/yuli_v_nazarov_yaroslav_m_blanter_quantum_transport.html

Cited pages 31, 34, 38

[49] I. O. Kulik. "Macroscopic Quantization and the Proximity Effect in S-N-S Junctions". In: *Soviet Journal of Experimental and Theoretical Physics* 30 (Jan. 1969), p. 944. URL: https://ui.adsabs.harvard.edu/abs/1969JETP...30..944K

Cited pages 31, 34

[50] C. W. J. Beenakker. "Why Does a Metal—Superconductor Junction Have a Resistance?" In: *Quantum Mesoscopic Phenomena and Mesoscopic Devices in Microelectronics*. Springer Netherlands, 2000, pp. 51–60. DOI: 10.1007/978-94-011-4327-1_4

Cited pages 31, 34

[51] Guy Deutschern. "Crossed Andreev Reflections". In: *Journal of Superconductivity: Incorporating Novel Magnetism* 15.1 (2002), pp. 43–47. DOI: 10.1023/a:1014075110249

Cited page 34

[52] Patrik Recher, Eugene V. Sukhorukov, and Daniel Loss. "Andreev tunneling, Coulomb blockade, and resonant transport of nonlocal spin-entangled electrons". In: *Physical Review B* 63.16 (Apr. 2001). DOI: 10.1103/physrevb.63.165314

Cited page 34

[53] G.B. Lesovik, T. Martin, and G. Blatter. "Electronic entanglement in the vicinity of a superconductor". In: *The European Physical Journal B* 24.3 (Dec. 2001), pp. 287–290. DOI: 10.1007/s10051-001-8675-4

Cited page 34

[54] L. Hofstetter et al. "Cooper pair splitter realized in a two-quantum-dot Y-junction". In: *Nature* 461.7266 (Oct. 2009), pp. 960–963. DOI: 10.1038/nature08432

Cited page 34

[55] D. Feinberg. "Andreev scattering and cotunneling between two superconductor-normal metal interfaces: the dirty limit". In: *The European Physical Journal B - Condensed Matter* 36.3 (Dec. 2003), pp. 419–422. DOI: 10.1140/epjb/e2003-00361-6

Cited page 37

[56] I A Sadovskyy, G B Lesovik, and V M Vinokur. "Unitary limit in crossed Andreev transport". In: *New Journal of Physics* 17.10 (Oct. 2015), p. 103016. DOI: 10.1088/1367-2630/17/10/103016

Cited page 37

[57] Viktoriia Kornich, Hristo S. Barakov, and Yuli V. Nazarov. "Fine energy splitting of overlapping Andreev bound states in multiterminal superconducting nanostructures". In: *Physical Review Research* 1.3 (Oct. 2019). DOI: 10.1103/physrevresearch.1.033004

Cited pages 37, 50, 51, 71

[58] X. Li et al. "Chemically Derived, Ultrasmooth Graphene Nanoribbon Semiconductors". In: *Science* 319.5867 (Feb. 2008), pp. 1229–1232. DOI: 10.1126/science.1150878

Cited page 39

[59] Minsoo Kim et al. "Valley-symmetry-preserved transport in ballistic graphene with gate-defined carrier guiding". In: *Nature Physics* 12.11 (June 2016), pp. 1022–1026. DOI: 10.1038/nphys3804

Cited page 39

[60] A. Anthore, H. Pothier, and D. Esteve. "Density of States in a Superconductor Carrying a Supercurrent". In: *Physical Review Letters* 90.12 (Mar. 2003). DOI: 10.1103/physrevlett.90.127001

Cited page 47

[61] Viktoriia Kornich, Hristo S. Barakov, and Yuli V. Nazarov. "Overlapping Andreev states in semiconducting nanowires: Competition of one-dimensional and three-dimensional propagation". In: *Physical Review B* 101.19 (May 2020). DOI: 10.1103/physrevb.101.195430

Cited pages 50, 71

[62] Sergey K. Tolpygo and Denis Amparo. "Electrical stress effect on Josephson tunneling through ultrathin AlOx barrier in Nb/Al/AlOx/Nb junctions". In: *Journal of Applied Physics* 104.6 (Sept. 2008), p. 063904. DOI: 10.1063/1.2977725

Cited page 52

[63] A.K. Jain et al. "Mutual phase-locking in Josephson junction arrays". In: *Physics Reports* 109.6 (July 1984), pp. 309–426. DOI: 10.1016/0370-1573(84)90002-4

Cited page 55

[64] J. J Riquelme et al. "Distribution of conduction channels in nanoscale contacts: Evolution towards the diffusive limit". In: *Europhysics Letters (EPL)* 70.5 (June 2005), pp. 663–669. DOI: 10.1209/epl/i2005-10028-0

Cited page 63

[65] M. Zgirski et al. "Evidence for Long-Lived Quasiparticles Trapped in Superconducting Point Contacts". In: *Physical Review Letters* 106.25 (June 2011), p. 257003. DOI: 10.1103/physrevlett.106.257003

Cited page 71

[66] Y. X. Liang et al. "Insight into low frequency noise induced by gate leakage current in AlGaAs/GaAs high electron mobility transistors at 4.2 K". In: *Applied Physics Letters* 99.11 (Sept. 2011), p. 113505. DOI: 10.1063/1.3637054

Cited pages 72, 96, 98

[67] M. F. Goffman et al. "Supercurrent in Atomic Point Contacts and Andreev States". In: *Physical Review Letters* 85.1 (July 2000), pp. 170–173. DOI: 10.1103/physrevlett.85.170

Cited page 75

[68] C. D. English et al. "Observation of nonsinusoidal current-phase relation in graphene Josephson junctions". In: *Physical Review B* 94.11 (Sept. 2016). DOI: 10.1103/physrevb.94.115435

Cited page 75

[69] R. Delagrange et al. "0-π quantum transition in a carbon nanotube Josephson junction: Universal phase dependence and orbital degeneracy". In: *Physical Review B* 93.10520069 (May 2016). DOI: 10.1103/physrevb.93.195437

Cited page 75

[70] Benedikt Mayer et al. "Lasing from individual GaAs-AlGaAs core-shell nanowires up to room temperature". In: *Nature Communications* 4.1 (Dec. 2013). DOI: 10.1038/ncomms3931

Cited page 85

[71] J. C. Weber et al. "Gallium nitride nanowire probe for near-field scanning microwave microscopy". In: *Applied Physics Letters* 104.2 (Jan. 2014), p. 023113. DOI: 10.1063/1.4861862

Cited page 85

[72] Y. Jin et al. "Ultra-low noise CryoHEMTs for cryogenic high-impedance readout electronics: Results and applications". In: *2016 13th IEEE International Conference on Solid-State and Integrated Circuit Technology (ICSICT)*. IEEE, Oct. 2016. DOI: 10.1109/icsict.2016.7998915

Cited pages 96, 98

[73] Takashi Mimura et al. "A New Field-Effect Transistor with Selectively Doped GaAs/n-AlxGa1-xAs Heterojunctions". In: *Japanese Journal of Applied Physics* 19.5 (May 1980), pp. L225–L227. DOI: 10.1143/jjap.19.l225. URL: https://doi.org/10.1143/jjap.19.l225

Cited page 96

[74] T. Mimura et al. "An enhancement-mode high electron mobility transistor for VLSI". In: *Jpn. J. Appl. Phys., vol. suppl. 20-1, pp. 364* (1981)

Cited page 96

[75] A. Juillard et al. "Low-noise HEMTs for coherent elastic neutrino scattering and low-mass dark matter cryogenic semiconductor detectors". In: *Journal of Low Temperature Physics* 199.3-4 (Nov. 2019), pp. 798–806. DOI: 10.1007/s10909-019-02269-5

Cited page 96

[76] J. L. Sauvageot et al. "Toward large μ-calorimeters x-ray matrices based on metal-insulator sensors and HEMTs/SiGe cryo-electronics". In: *Space Telescopes and Instrumentation 2016: Ultraviolet to Gamma Ray*. Ed. by Jan-Willem A. den Herder, Tadayuki Takahashi, and Marshall Bautz. SPIE, July 2016. DOI: 10.1117/12.2232397

Cited page 96

[77] A. Phipps et al. "An HEMT-Based Cryogenic Charge Amplifier for Sub-kelvin Semiconductor Radiation Detectors". In: *Journal of Low Temperature Physics* 184.1-2 (Jan. 2016), pp. 505–511. DOI: 10.1007/s10909-016-1475-2

Cited page 96

[78] A. Phipps et al. "A HEMT-based cryogenic charge amplifier with sub-100 eVee ionization resolution for massive semiconductor dark matter detectors". In: *Nuclear Instruments and Methods in Physics Research Section A: Accelerators, Spectrometers, Detectors and Associated Equipment* 940 (Oct. 2019), pp. 181–184. DOI: 10.1016/j.nima.2019.06.022

Cited page 96

[79] Joël Griesmar. "Un spectromètre mésoscopique reposant sur l'effet Josephson". PhD thesis. Collège de France, 2018

Cited page 104

RÉSUMÉ

Cette thèse traite de l'hybridation des états liés d'Andreev dans un système formé de deux jonctions Josephson contiguës, une "molécule d'Andreev". Il est prédit que les dispositifs incorporant des molécules d'Andreev ont un spectre d'énergie avec des anti-croisements et une relation courant-phase non conventionnelle.
La première partie est une analyse théorique de la molécule d'Andreev. Les deux mécanismes microscopiques à l'origine de l'hybridation des états liés d'Andreev y sont décrits. De plus, les caractéristiques électriques d'une molécule dans des configurations de circuits multiples y sont calculées à l'aide de différents cadres théoriques.
Dans la deuxième partie sont présentées des mesures d'un circuit constitué de deux jonctions Josephson très proches l'une de l'autre. Bien que des signes possibles d'hybridation soient détectés, en raison de la présence de bruit et d'une séparation des jonctions trop faible, les résultats ne sont pas concluants.
Dans la troisième partie sont décrits les détails techniques de la fabrication de l'appareil et du dispositif de mesure, y compris l'utilisation à des millikelvins d'un amplificateur DC cryogénique.

MOTS CLÉS

Physique mésoscopique, états liés d'Andreev, jonction Josephson, molécule d'Andreev, hybridation

ABSTRACT

This thesis discusses the hybridization of Andreev bound states in a system of two closely spaced Josephson junctions, an "Andreev molecule". Devices incorporating Andreev molecules are predicted to have an energy spectrum with avoided crossings and a non-conventional current-phase relation.
The first part is a theoretical analysis of Andreev Molecule. Two microscopic mechanisms at the origin of the hybridization of Andreev bound states are explained. Furthermore, electrical characteristics of a molecule in multiple circuit configurations are calculated using different theoretical frameworks.
In the second part measurements of a circuit made up of two Josephson junctions in close proximity to each other are presented. Although possible signs of hybridization are detected, due to the presence of noise and insufficiently small junction separation, the results are inconclusive.
In the third part technical details of device fabrication and the measurement setup, including a millikelvin DC cryogenic amplifier, are described.

KEYWORDS

Mesoscopic physics, Andreev bound states, Josephson junction, Andreev molecule, hybridization